NATURE AND EVOLUTION OF CONDUIT FAULTS IN THE 2004-2008 MOUNT ST. HELENS LAVA DOME ERUPTION

by

ELIZABETH ANNE FRIEDLANDER

B.Sc. Honours, Colorado College, 2007

A THESIS SUBMITTED IN PARTIAL FULFILMENT OF
THE REQUIREMENTS FOR THE DEGREE OF

MASTER OF SCIENCE

in

The Faculty of Graduate Studies

(Geological Sciences)

THE UNIVERSITY OF BRITISH COLUMBIA
(Vancouver)

January 2012

Abstract

Mount St. Helens reawakened 24 years after erupting in the 1980's. This effusive eruption produced 95 million cubic meters of dacite in the form of 7 discrete, competent spines or domes of lava between September 2004- June 2008. The spines comprise low-porosity dacite that is inferred to have crystallized at a depth of about 1 km and are enveloped by a 1-3 meter carapace of fault gouge. The rate of linear extrusion of the spines peaked at 11 m/day in November 2004 and subsequently slowed to < 0.5 m/day. Dome growth was accompanied by a "drumbeat" seismicity that was sourced from 1-0.5 km below the vent.

Here, field, petrographic, and microstructural observations on the nature of deformation attending the extrusion of Spines 4, 5 and 7 at Mount St. Helens (2004-2006) are presented. The enveloping fault zones provide a static view of the cumulative strain produced by shear along the conduit wall. The conduit faults narrow from Spine 4 to Spine 7 and exhibit fewer macroscopic brittle features. Strain accommodation is achieved through a scale-dependent ductility.

The subsurface ascent velocities for each packet of magma are reconstructed using surface observed extrusion rates. Computed shear strain rates for the margins of the conduit range from $1x10^{-4}$ to $7.9x10^{-5}$ s^{-1}. As ascent rate decreases, fault zone width also decreases maintaining an average shear strain rate of $4.3x10^{-5}$ s^{-1}. Intense strain localization within each fault zone is expressed by 0.001 m thick slickensides implying very high (co-seismic) transient shear-strain rates of $1x10^{-1}s^{-1}$ (Spines 4-5) to $2.2x10^{-2}s^{-1}$ (Spine 7).

I conclude with a time and space model for the evolution of the fault zone as magma ascends the conduit, and how the fault zones evolve through time. The factors that

contribute to the differences in conduit fault zone width and nature throughout the eruption are: 1) differences in ascent rates at the onset and origin of brittle failure, 2) variations in shear strain rates, 3) and the increasing residence time throughout the eruption that the damaged fault rocks experienced at high temperatures within the conduit.

Preface

This thesis is written as a manuscript written for publication in a peer reviewed journal. I am senior author and my co-authors are L.A. Kennedy and J.K.Russell. The project was equally supervised by L.A. Kennedy and J.K. Russell with critical initial guidance in the field from John Pallister from the USGS at the Cascade Volcano Observatory. I was responsible for executing the entire field campaign into the crater of Mount St. Helens in the summer of 2010 that involved other research groups from University College London and Ludwig-Maximillians-Universitat Munchen but did not collaborate with them on this research.

I carried out the initial fieldwork, hand sample and microstructural observations with direct guidance from L.A. Kennedy and J.K. Russell. I developed the reconstruction of the spines in time and space model with critical guidance from J.K. Russell. Additionally, the structural reconstruction and fault mechanics was developed with L.A. Kennedy and J.K. Russell.

Table of Contents

List of Tables

List of Figures

Chapter 1: Introduction

Chapter 2: Nature of Conduit Faults

List of Symbols and Abbreviations

MSH		Mount St. Helens
x/z		Kinematic plane
x/y		Fault plane
M_d		Magnitude
Az		Azimuth
Δt_s	days	Duration of for each spine surface eruption
Q_{min} /Q_{max}	m^3/s	Surface growth rate for each spine (min/max)
U_{min}/U_{max}	m/day	Surface extrusion rate (min/max)
T_{fz}	m	Thickness of conduit fault (fault core &damage zone)
T_{core}	m	Thickness of fault core
T_{min}	m	Minimum thickness of slickenside
V_{total}	m^3	Total volume of the 2004-08 dome (USGS, 2009)
V_{min} /V_{max}	m^3	Volume produced during each spine (min/ max/avg)
H_{min} /H_{max} /H_{av}	m	Height of each spine (min/ max/average)
D_{min} /D_{max} /D_{av}	m	Cylindrical model diameter or dacite spine
H_{min} /H_{max} /H_{av}	m	Min/ max/average height of total column of dacite
t_s / t_{500} / t_{1000}	day	Day in the eruption when the top of each spine's position is at surface, 500 and 1000 meters below vent
v_{500}	m/s	Velocity of spine from 500 meters depth to the surface
v_{1000}	m/s	Velocity of ascent rate from 1000-500 meters depth
$\gamma'fz$	/s	Shear strain rate accommodated fault core and damage zone from
$\gamma'h$	/s	Shear strain rate accommodated across a the diameter of the spine from
$\gamma'ss$	/s	Shear strain rate accommodated across a single slickenside surface

Acknowledgments

They say it takes a village to raise a child. I'd extend the expression further to say it takes a community to write a thesis. Although I was the final pipe the contents of this thesis poured through, there is number of people that contributed that I am ever so grateful for. Finical support for this M.Sc. thesis was provided by an NSERC Discovery Grant held by Professor Kelly Russell and Professor Lori Kennedy.

First I'd like to thank my supervisors, Kelly Russell and Lori Kennedy. Without both of you, I would not have started or finished - thank you for pushing me to overcome the coefficient of static friction and continue to 'steady-state' movement. Kelly, thank you for your enthusiasm, curiosity, conversations and commitment to honest, noble science. I cannot thank you enough for your guidance, advising and necessary help with writing up. Lori, thank you for encouragement, curiosity, insight and on fault rocks and life outside of grad school. Your enthusiasm and knowledge is extensive and always enlightening! You two have built a lab that I am proud and thankful to be a part of.

To the VPL/CESL lab, what would I do without my comrades? Lucy, thank you for your constant and steady friendship, the pep-talks, the ridicule (yes, the humorous ridicule), the adventures, and abundant support. Jenny, thank you for your continued friendship and encouragement (8 years!). Shelly, thank you for keeping me in check, Chanone, for support and encouragement. Dan, from CC to here, I am thankful for you and your constant cadence in life. Alex, thank you for 'having my back', and for your never ceasing enthusiasm. Michelle, thanks for your kind, genuine, honest soul . Stephan, thank you for showing all of us what life can be like when lived with great expression and without regrets. Luke, the new guy, you're a great one too. Other UBC folks I'd like to thank for being in my life and talking geology: Kirsten, Leanne, Moira, Jack, Will, Dave, Leif, JF.

To my found family in Vancouver – Christy, Sam, Trudy, Charlotte, I am grateful that I can call you family. Thank you for keeping me grounded. BT and Nancy, you too. To my scattered family across the world, thank you for love from afar (e.g. March, Erica, Kerry, Kelly, Becca).

I am also grateful to John Pallister, David Sherrod, Cynthia Gardner, Roger Denlinger and the Cascade Volcano Observatory, USGS for scientific discussion and

support with logistical planning for the field campaign. I also thank Peter Frenzen who is in charge of permitting within the Gifford Pinchot National Forest for guidance in access to the crater of Mount St. Helens. Jeff Linscott and J.L Aviation, thank you for superb helicopter support in and around the crater. Alex Kushnir and Stephan Kolzenberg for support in our crazy journey into the crater. I also will thank the long-established monitoring systems operated by the U.S. Geological Survey, USGS and their David A. Johnston Cascades Volcano Observatory (CVO) and the Pacific Northwest Seismic Network (PNSN) at the University of Washington. Chelsea Raley & James Welles, thank you for your hard work with sample preparation and general contagious enthusiasm for geology.

Other people I'd like to thank: Jim Mortensen, Ken Hickey, Mati Raudsepp, Jenny Lai and the rest of the XRD/SEM Facility Staff, Arne Toma, Teresa Woodley, Cary Thompson and Michael Hermawan other grad students and professors who have kept me engaged in other aspects of geology not directly related to this research.

And, of course, I thank my family, Mom, Papa, Tommy Tom, Andy, Kelli & Little Friedlander to be, I am grateful beyond words for your love, support and presence in my life… at the end of the day, you all remind me of what love is and why living in community and with family really means.

1. Introduction

The 2004 to 2008 eruption of Mount St. Helens extruded 95 million m^3 of low-porosity, crystalline dacite in the form of seven discrete spines (Fig. 1.1, Fig.1.2) (Sherrod et al., 2008). Rates of linear extrusion for the lava domes varied from a peak of 11 m/day in November 2004 to < 0.5 m/day in February 2006 (Moran et al., 2008a; Vallence et al., 2008) and the lava dome growth was accompanied by a consistent "drum beat" seismicity (Iverson et al., 2006). The 2004-2008 Mt. St. Helens lava spines are distinctive in that each features an exterior carapace of variably consolidated fault gouge and striations (Cashman et al., 2008). The gouge is comprised of brecciated to finely comminuted dacite lava that formed along fault zones localized at the interface between the lava and the conduit wall rocks (Cashman et al., 2008). Previous work has described this fault zone gouge and there are several models proposed for its origin (Cashman et al., 2008; Kennedy and Russell, 2011; Pallister et al., 2008a; Smith et al., 2011).

Here, I build on this earlier work by providing field-based descriptions of the strain distribution within the Mount St. Helens dacite lava spines extruded from 2004 to 2008. The objectives of this project are: **(1)** to describe the architecture of, and variations in, the conduit faults in the Mount St. Helens 2004-2008 lava dome, **(2)** to identify the mechanisms of deformation/mode of failure within the fault zones, **(3)** to explain the evolution of the enveloping fault zones as magma ascends the conduit, and **(4)** to create a time and space model for the initial formation of the conduit faults at depth and their evolution throughout the eruption.

My research is based on metre-scale structural mapping of spines 4, 5, and 7. These maps document the transition in structural state from dacite to localized fault zones composed

of cataclasite and finely comminuted gouge. The laboratory component of my study involves petrographic and microstructural observations on oriented samples collected across these conduit fault zones. These observations document the textural changes within the ascending dacite caused by shear between the conduit wall rocks and the viscous to solid dacite. Surface extrusion rates for each spine (Moran et al., 2008a; Scott et al., 2008; Sherrod et al., 2008; Vallence et al., 2008) were used to reconstruct the ascent velocity of the subsurface magma. These reconstructed velocities allow me to calculate the shear strain rates associated with strain localization along the conduit walls. These results, coupled with the field and microstructural constraints, are used to build a space and time model for deformation of the dacite magma during ascent from 1 km depth to the surface. The model couples volcanological (effusion rates), petrological (rock types/physical properties), structural (maps and textures), and geophysical (seismicity) observations to explain the nature, origin and evolution of the strain localization during the 2004-08 Mount St. Helens lava dome eruption.

1.1 Dome Growth and Conduit Shear Zones

Degassed, high viscosity magmas commonly erupt from volcanic vents to produce mounds, domes and spines of partly to fully crystallized lava (Fink and Anderson, 2000; Fink and Griffiths, 1998; Sparks et al., 1998; Watts et al., 2002). Although the majority of the 2004-2008 activity at Mount St. Helens was effusive (e.g., producing 'whale back' lava domes) (Sherrod et al., 2008; Watts et al., 2002), these systems have the capacity to rapidly switch to explosive behavior. Four months after the onset of dome growth at Mt. St. Helens, two major explosions (January 16 and March 8, 2005) punctuated the emplacement and disintegration of the seven successive spines (Rowe et al., 2008). Other spine forming volcanoes (e.g. Soufriere Hills, Montserrat, Unzen, Japan, Merapi, Philippines, Montagne

Pelée, Martinque and Santa Maria, Santiaguito) have demonstrated the capacity to oscillate between effusive lava dome growth and the sudden collapse of these unstable landforms triggering pyroclastic eruptions (Carn et al., 2004; Kaneko et al., 2002; Sparks et al., 2000a; Tanguy, 2004; Watts et al., 2002).

Volatile content, ascent rate and permeability of domes are the main parameters controlling dome geometry and extrusion mechanisms (Sparks et al., 1998; Watts et al., 2002). There are three main types of lava domes categorized by styles of growth: 1) plug domes and spines erupt as a solid mass of rock, 2) endogenous domes grow by expansion driven by addition of new material within the dome, and 3) exogenous domes grow in size via effusion of new lava through the exterior surface of the dome (Watts et al., 2002; Williams, 1932). Styles of dome growth are strongly tied to extrusion rate. In describing the 2000 lava dome eruption of Soufriere Hills Volcano, Montserrat, Watts et al (2002) linked volumetric growth rates of 7 m^3/s to the production of pancake-shaped exogenous dome growth, while lower rates of 1-3 m^3/s to the growth of plug domes and spines. Slower rates of ascent allow magma to degas and therefore solidify and extrude as a solid monolith-like spine (Sparks et al., 2000b). The lava spines commonly exhibit smooth, continuous, striated exterior surfaces that preserve slickensides and gouge (Jaggar, 1904; Lacroix, 1904; Williams, 1932). Mimatsu (1995) describes an erupted solid spine on the mountain of Usu, Japan as 'having a shape like the bottom of a boat with a coating of pulverized rock or dirt with grooves or scratches parallel to the extrusion direction'.

Descriptions of these 'whaleback' and 'boat-like' landforms with smooth and striated surfaces are commonly described spine-forming lava domes throughout history (Jaggar, 1904; Lacroix, 1904; Sparks et al., 2000a; Tanguy, 2004; Watts et al., 2002; Williams, 1932).

However, there has been little detailed characterization of these bounding-fault surfaces due to the lack of intact exposures and dangerous locations. Mount St. Helens serves as an ideal field location to map the transition from protolith dacite to deformed dacite in fault zones, where volcanic activity is closely monitored and exposures of these conduit faults are intact (Fig.1.2).

Previous work on the MSH fault gouge were carried out by Cashman et al. (2008) and was conducted on dredged samples collected from the crater by helicopter during the eruption. Cashman et al. (2008) concluded the fault zone formed as a brittle response from friction along the conduit wall because the dacite was degassed, dry and solid at 1 km depth. Sparks et al. (2000) describes similar striated shear zones at Soufriere Hills, Montserrat that were detached form the spin and "left behind" on the conduit wall. At Mount St. Helens, the shear zones are not fully detached from the extruded spines, but rather encase the solid dacite spines in smooth slickensides (Fig. 1.2). These volcanic conduit faults originate in the subsurface near the margins of the dacite where it is contact with the conduit wall (Fig. 1.3B, c, d & e). Also, these conduit faults are strikingly similar to the general internal structure of tectonic fault zones, in that, they feature three main architectural elements: undeformed protolith, damage zone and fault core that accommodates the majority of the strain (Fig. 1.3A) (Chester et al., 1993; Faulkner et al., 2010; Pallister et al., 2008a).

The cessation of dome growth has provided a crater with fresh, accessible, and moderately intact outcrop of exposed asymmetric fault zones, which we mapped in 2010 (Fig. 1.3 f). The sequence of extrusion of these spines is well constrained, therefore the 2004-2008 deposit is ideal to study.

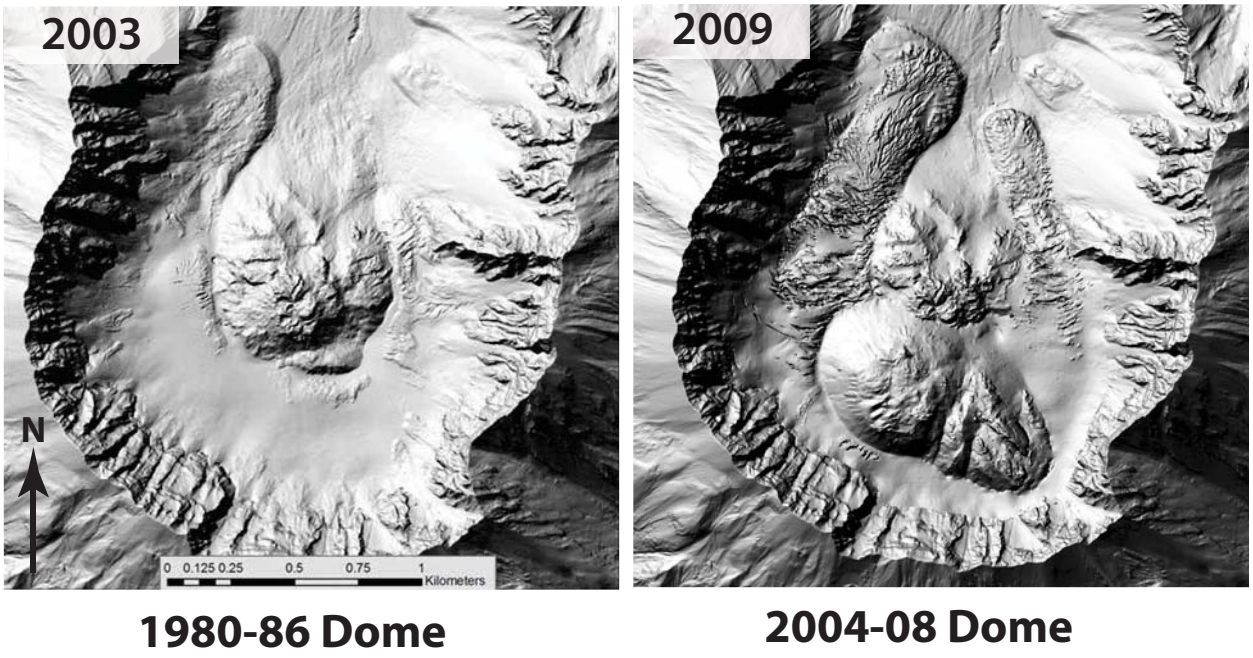

Figure 1.1. Mount St. Helens Crater: View of Before and After the 2004-2008 Eruption. The crater of Mount St. Helens, Washington before (2004) and after (2009) the dome-forming eruption in 2004-2008. Both images are digital elevation maps (DEM) that are hill shaded. The crater of Mount St. Helens in 2003 consists of the 1980-86 dome deposit that is surrounded by a crater glacier. The 2009 DEM shows the new dome that erupted to the south of the 1980 dome, puncturing through and displacing the crater glacier.

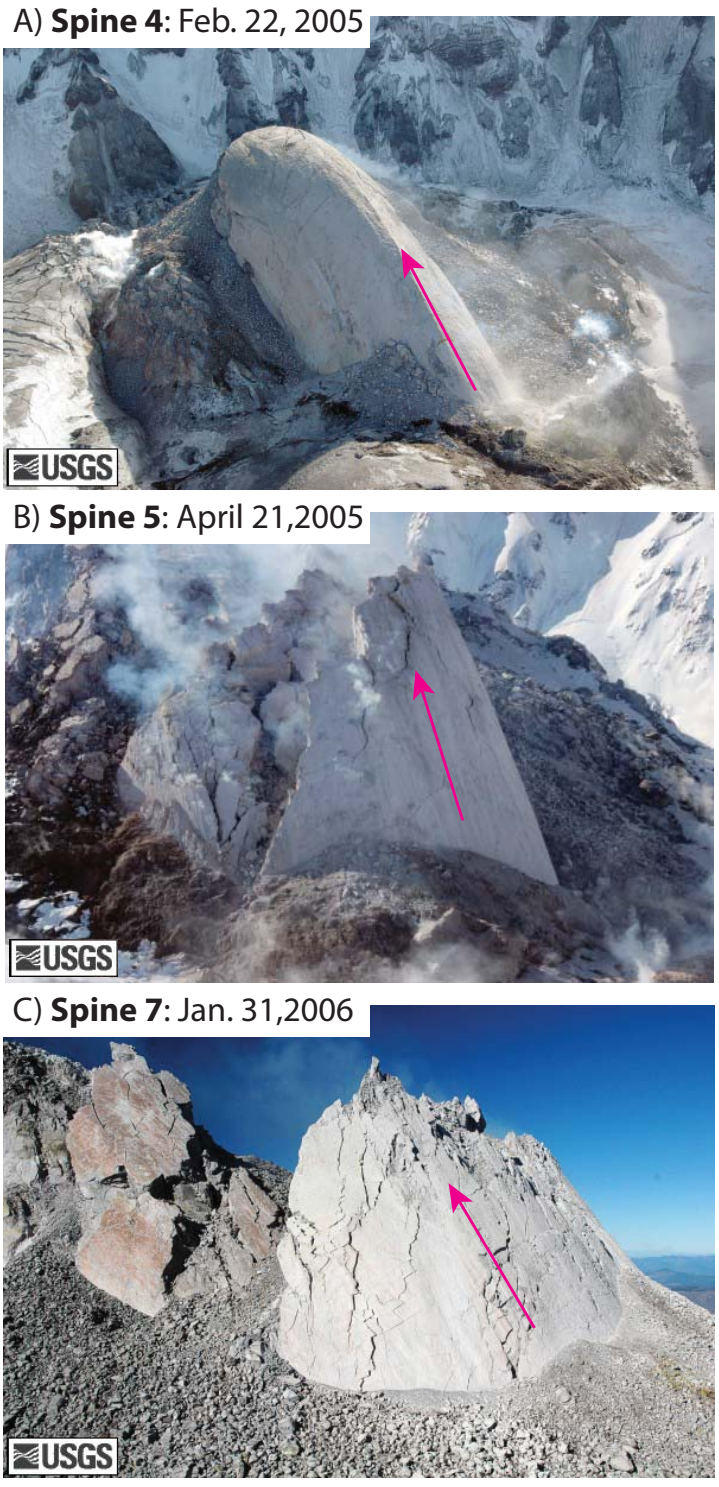

Figure 1.2. Spine 4,5 and 7 During the Eruption. (A) USGS photo from February 22, 2004 of the spine 4 whale back with long axis plunging to the northwest, extrusion is to the southeast (arrow). (B) USGS photo from April 21,2005 of spine 5 extruding to the south (arrow). (C) USGS photo from January 31, 2006 while spine 7 was extruding at the surface towards the southwest (arrow).

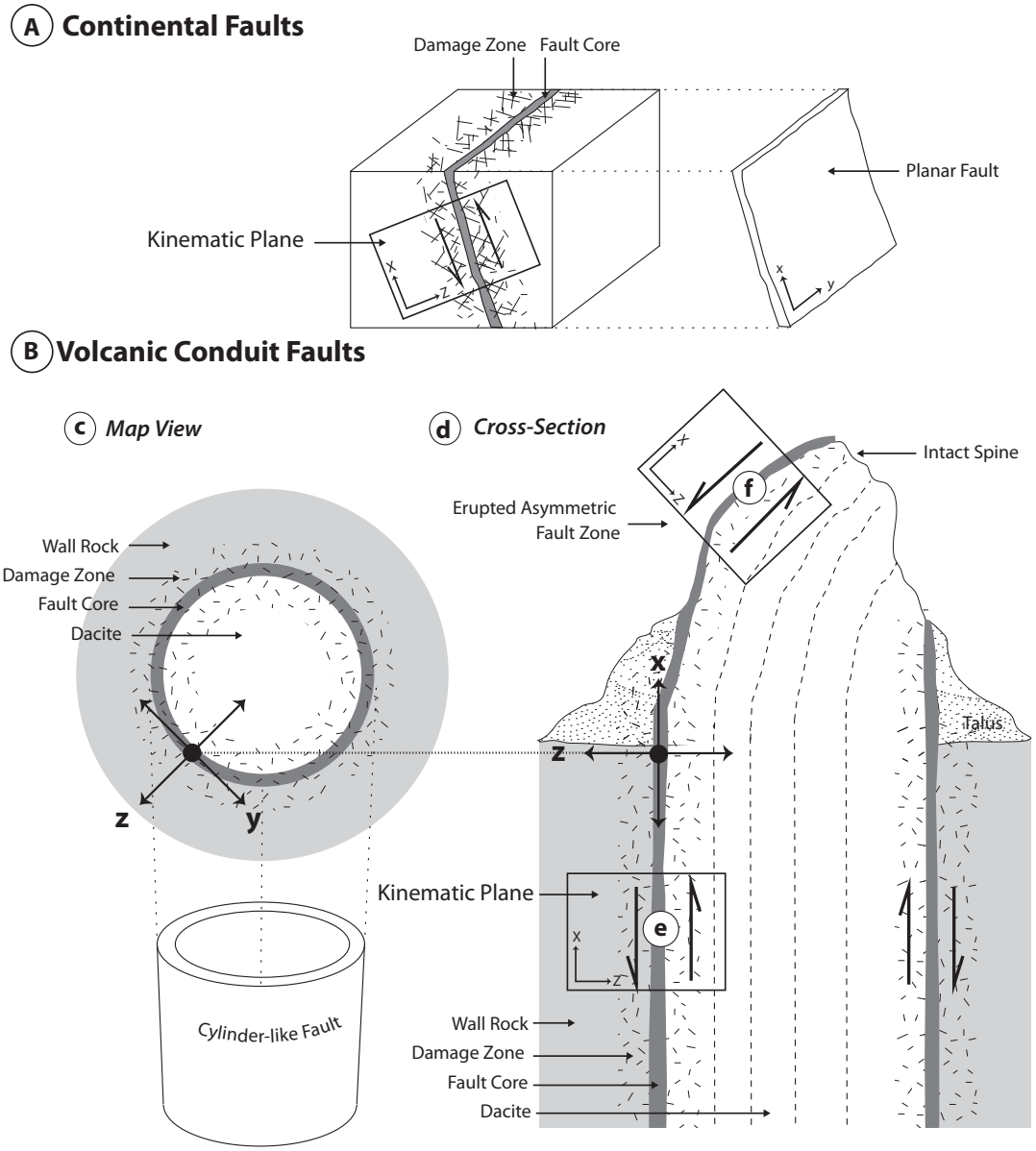

Figure 1.3. Continental Faults vs. Volcanic Vent Faults. (A) Schematic of a simplified continental fault zone structure showing a fault surface (x/y) represented by a single, high-strain fault core surrounded on both sides by a fractured damage zone (after Chester and Logan, 1986). The kinematic plane (x/z) is perpendicular to the fault plane and shows the relative movement within the fault zone along the x-axis (greatest lengthening) and z-axis (greatest shortening). (B) Conduit fault zones within volcanic conduits. (c) Schematic map view of a cylindrical fault zone formed at margin of volcanic conduits. These have similar features to continental fault zones: a high-strain fault core surrounded on both sides by a fractured damage zone in the dacite lava dome and surrounding conduit wall rock. This map view is in z/y plane where the y-axis is the asymptote to the cylindrical fault zone and the z-axis therefore also changes orientation. (d) Schematic cross section of solid dacite spine that is showing fault zone development at the conduit margin where (e) the kinematic plane in the x/z plane during ascent. As the solid spine reaches the surface it erupts as a whaleback or near vertical spine revealing one side of the fault zone that formed at depth. (f) At surface, we see the exposed asymmetric fault zone on the exterior of the spine; the attitude of the kinematic plane is rotated from its original orientation in the subsurface.

2. Conduit Faults in Mount St. Helens 2004-2008 Lava Dome

2.1 Introduction

The conduit faults located at the margin of the spines in the Mount St. Helens 2004-2008 eruption vary texturally throughout the eruption. In this chapter, the architecture of the fault zones is described using conventional continental fault zone terminology. The distribution of strain is described through macroscopic, petrographic and microstructural observations that highlight the transition from the protolith dacite to the fractured dacite in the damage zone to the finely comminuted gouge in the fault core.

2.2 Methodology

A series of detailed cross sections of the conduit faults were completed for spines 4, 5 and 7. Faults rarely comprise a single discrete failure surface but, rather, define a zone of variable deformed rock featuring a complex internal structure (Wibbereley et al., 2008). To avoid visual and sampling bias, the structural geometry of the fault zones was mapped using a 2mx2m dimensional grid partitioned into 20 cm squares. Grid map locations (Fig. 2.1) were chosen based on the quality of the fault zone exposure and safe access to the outcrop. We chose outcrops that exposed the kinematic (x/z) plane of the fault zone at each spine margin (Fig. 1.3f). The kinematic plane (x/z) is perpendicular to the local fault surface (x/y) and contains kinematic indicators that deduce transport direction (Van der Pluijm and Marshak, 2004) (Fig. 2.2, Table 2.1). The term, 'local kinematic plane' is used to emphasize two structural conventions unique to conduit faults: (1) each cross section mapped is only a section of the cylindrical fault and therefore, the orientations of the local kinematic plane varies around the circumference of the spine and (2) the field-mapped fault surface and kinematic plane has been rotated since formation of the fault zone within the conduit.

The geological structures and fault rocks document the evolution of the fault zone as the magma ascended through the conduit. Riedel shear zone terminology is used to define fault related fractures (Fig.2.3) (Logan et al., 1992; Rutter, 1986; Skempton, 1966). Hand sample descriptions follow the fault rock convention modified by Snoke et al (1998) where gouge and breccia refer to incohesive fault material and cataclasite refers to cohesive fault-derived material. Due to the nature of the Mount St. Helens conduit fault zone, we distinguish fault gouge and breccia as unconsolidated material, indurated fault gouge as cohesive but easily fractured with a hammer, and cataclasite as cohesive rock that does not disintegrate when struck with a hammer.

Structurally oriented samples were collected at recorded locations across each spine fault zone (Appendix A, B, C). The extremely broken and friable samples were stabilized by epoxy resin impregnation in the lab. Samples were saw cut into serial sections parallel to the local kinematic plane (Fig. 2.2, Table 1), in order to provide information on microstructures, kinematics of movement and variability along strike. A selection of samples was also cut in the x/y plane (parallel to the fault plane) and the z/y plane to assess structural features in 3D.

Thin section and Scanning Electron Microscope (SEM) analysis were performed on oriented, polished thin sections, cut parallel to the local kinematic plan, to catalogue the textural changes and microstructures. From these observations, the active deformation mechanisms across each fault zone can be assessed. Mineralogy and glass content were estimated by petrographic examination and X-ray diffraction analysis (Appendix D). Geochemical analysis of major and minor elemental abundances was performed on specific samples from Spine 4 and 7 using X-ray fluorescence (Appendix D).

2.3 Structure of the Mount St. Helens 2004-08 Lava Dome

The 1980-86 and the 2004-08 domes are surrounded by a glacier that is covered lightly by debris from the rock avalanches from the crater walls. As of August 2010, the majority of the current 2004-08 composite dome deposit comprises angular talus overlying unstable but intact outcrops of dacite. Fumaroles are common. The dome is divided into three main talus mounds consisting of Spines 3 and 4 to the east, Spine 5 in the middle and the largest, Spines 6 and 7 to the west. There are accessible outcrops of Spines 3, 4, 5 and 7. Exposures of the margins of the erupted spines range in thickness from 1-10 meters. Our mapping focused on the intact outcrops of Spines 4, 5, and 7. Many exposures were not accessible due to unstable overhangs, or extremely steep, insecure slopes. Mapping was therefore focused on Spines 4, 5 and 7. The accessible outcrops display structures and zones of fault rocks that yielded reliable kinematic information that is consistent with the observed extrusion and transport of material from the vent into the crater.

2.3.1 Spine 4

2.3.1.1 Spine 4 Macroscopic Field Observations

Spine 4 lies in the southeast part of the crater and consists of large, angular, dacite talus distributed amongst 3 ridges striking NW/SE of intact outcrop (Fig. 2.1). These exposures are the remnant carapace of the whaleback surface that had initial total dimensions of 100 x 200m. Remnant masses of coherent dome lava still feature smooth surfaces having prominent striations. These striations on Spine 4 exposures range in orientation: trending from NNW/SSE to E/W and plunge from 20 to 38° towards E/NE/N (Fig. 2.2A). Many outcrops expose 1-3 meters of fault gouge and cataclasite that contain layers of slickensides, oriented parallel to the fault surface above variably fractured dacite (Fig. 2.4A,B). These slickenside

lineations cluster with an average orientation of 30°→345 and range from 35°→335 to 9°→002 based on the location around the perimeter of Spine 4. Listric normal faults, on a scale from a few centimeters to meters, crosscut the fault zone. These faults strike perpendicular to the long axis of the spine and dip to the north. Multiple joints, oriented perpendicular to the striated surfaces, extend from the margin into the spine exposing vertical sections 2 to 30 meters in depth (Fig. 2.4C,D) that reveal a fracture network that extends two meters into the interior of the spine. Some intact outcrops are large enough to exhibit the smooth, curviplanar exterior geometry of whaleback spine (Fig. 2.4D) that was observed during the eruption (Sherrod et al., 2008).

Table 2.1. Structural Data. Select structural data including fault plane, grid map and corresponding motion plane. See Fig. 2.1.

Spine	Label	Fault Plane	Grid Map Plane	Kinematic Plane
4	D4G1	312/28 NE	172/78 W	171/62 W
4	D4G2	325/23 NE	169/85W	180/66 W
4	D4G3	325/23 NE	169/85 W	180/66 W
4	D4L4	331/28 NE	-	132/50 SW
4	D4G5	290/30 N	150/89 SW	168/74 W
4	D4G6	285/24 N	010/88 E	168/72 W
4	D4L7	254/35 NW	-	157/84 W
5	D5L1	009/61 E	-	246/41 NW
5	D5L2	000/65 E	-	244/46 NW
7	D7G1	009/60 E	235/82 NW	240/65 NW
7	D7L2	002/46 E	-	250/70 NW

2.3.1.2 Spine 4 Cross-Section Maps and Log

Five detailed 2x2 m grid maps were produced. Each location was chosen to map the local kinematic plane of the conduit fault. Figure 2.5 is a representative example of one of the Spine 4 grid maps and shows the transition from flow-banded dacite, to cataclasite to fine-grained slickensides and unconsolidated gouge. The cross sectional grid maps are mapped in their field orientation, post extrusion and settling (Fig. 1.3f). The fault rocks and fracture geometry observed are strikingly similar to textures observed in continental faults. The kinematics inferred from the fracture pattern with prominent Riedel, (R1) Y and P orientations are consistent with the extrusion direction of spine 4 (Fig. 2.3). Textural and structural elements from these 4 cross section grid maps have been compiled into a single composite log (Fig 11A, Appendix B). The compilation cross-section is rotated to vertical fault zones to emulate the orientation of the kinematic plane during shearing along the conduit wall (Fig. 1.3e).

Loose, powdery fault gouge is present at the upper surface of most outcrops (Fig. 2.4A). The gouge is unconsolidated, matrix supported and poorly sorted. The clasts within the gouge include: variably fractured angular to sub-rounded clasts of dacite, 'snowballs' of indurated finer grained gouge and sub-angular conduit wall rock. Fine-grained slickenside layers are within the gouge, parallel to the fault surface and spaced 1 mm to 10 cm apart (Fig. 2.4A-B, 2.5, 2.6A). These surfaces are typically indurated, forming a hard and resistant shell that aids in the preservation of the loose fault gouge. In cross section the slickensided surfaces exhibit an asymmetrical grain-size reduction, with the smallest grains towards the top indurated surface. These surfaces are parallel to sub-parallel to the local fault plane, are sub-

planar to weakly undulating and can extend for meters. The slickenside lineations on these planes are consistently parallel to the extrusion direction of the spine.

The variably indurated gouge transitions into cohesive cataclasite towards the interior of the spine. The cataclasite is matrix supported with mm-10 cm fragments of dacite wall rock clasts that are angular to sub-rounded (Fig. 2.6B). Some dacite clasts are competent while others are fractured. The matrix comprises < 2 mm clasts of dacite and conduit wall rocks. While some cataclasite layers are void of fractures, others have small networks of low-angle normal Riedel (R_1, R_2,) and Y fractures (Fig. 2.6B-C).

The boundary between the cataclasite (i.e. the fault core) and the variably fractured dacite (i.e. the damage zone) towards the interior of the spine is distinct, sharp and texturally variable (Fig 2.5, 2.6A,C). The boundary can be 1) planar, 2) cuspate or 3) is angular with a 'saw-tooth' patter. The contact varies along strike (e.g. Figure 2.5). The planar boundary surfaces are scoured and are oriented parallel to the local fault plane (e.g. north end of cross section Fig. 2.5, Fig. 2.4B). The saw-tooth boundary is created by low-angle normal faults (R_1) and higher angle reverse faults (R_2), that offset the cataclasite (e.g. south end of Fig. 2.5). The cuspate boundary lies between the planar and saw-tooth end members and here, low-angle Riedel faults are truncated at the cataclasite/dacite boundary (e.g. middle Fig. 2.5, 2.6C).

The damage zone comprises variably fractured dacite. There is a consistent fracture geometry that exists at all scales within the damage zone (Fig. 2.3, 2.5B). Riedel shear fractures link toY-shears that are parallel to the local fault place. P and X shear fractures are less common. The dacite directly at the damage zone/fault core boundary is cut by closely spaced prominent decimeter to meter-length fractures, most abundantly, R_1. Many Riedel

fractures are weakly folded. Fracture density decreases toward the interior of the spine with the exception of concentrated zones of local high strain accommodation that are oriented sub parallel to the main fault surface and range in thickness from 2-10 cm. These higher strain zones have a well-developed R and Y shear fabric that typically progresses along strike into angular, unconsolidated, flakey breccia (Fig. 2.6D). Although the rough fracture surfaces within the damage zone do not contain fine-grained slickensides, they do contain a thin dusting of fine-grained powder.

A weak foliation defined by planes of micro-fractures, spaced mm apart, is present throughout the competent dacite in the R_1 and Y orientation within 1-2 meters of the fault core (Fig. 2.6F). This foliation and the pervasive fractures decrease in density away from the fault core. The least deformed material is massive, moderately flow-banded dacite defined by alignment of euhedral phenocrysts (hornblende, hypersthene, plagioclase) within a microcrystalline groundmass.

2.3.2 Spine 5

2.3.2.1 Spine 5 Macroscopic Field Observations

Spine 5 forms a ridge composed of sharp, angular talus located to the west of Spine 4 that strikes north-northeast and south-southwest (D5L1 & D5L2 in Fig. 2.1). At the crest of this ridge is an excellent exposure of the fault surface that strikes almost north/south and dips 60° east exposing the eastern shell of the extruded spine (Fig. 2.7A). The slickenside lineations have an orientation that averages 30°→025 and ranges in orientation from 30°→019 to 34°→030 (Fig. 3B). The west slope below the fault plane exposes dacite that is highly brecciated and is located above angular cataclasite (Fig. 2.7B). Spine 5 has no complete outcrops of the local kinematic plane, however, the deterioration aids in exposing

the outcrop along strike. A summary stratigraphic log was constructed including textures and fractures observed through the accessible parts of the entire outcrop (Fig. 2.11B). The rocks and textures in Spine 5 are highly altered by very active sulfurous fumaroles depositing sulfur and red iron oxides within cracks. Many of the textures and fractures observed in Spine 4 were also abundant in Spine 5. However, Spine 5 offers some new textures not observed in Spine 4.

2.3.2.2 Spine 5 Log

Spine 5 conduit fault zone contains two separate high strain zones with observed displacement. Strain, is therefore distributed not only at the contact with the conduit wall, but is also partitioned to a coarser cataclasite/breccia zone that does not contain fine-grain slickensides. The outer fault core is the primary fault core, most similar to the fault core observed in Spine 4 and the inner cataclasite zone being the secondary with brecciated dacite in between (Fig. 2.11B).

The primary fault core is capped with unconsolidated, poorly sorted gouge of variably rounded clasts of dacite from >1 mm-8 cm. Along the Spine 5 ridge, the gouge ranges in thickness from 1 to 10 cm, however it can be absent thereby exposing indurated slickensided surfaces that cap indurated gouge. This gouge to cataclasite layer is 40-60 cm thick and is similar in grain size and shape variability that was observed in Spine 4. The gouge and cataclasite layers are matrix supported with sub-angular to sub-rounded clasts of dacite from 1 mm to 10 cm (Fig. 2.6B). Unique to Spine 5 is the yellow and red mineral precipitates as a result of active sulfurous fumaroles (Fig. 2.6B,E). Interlayered within the gouge are indurated, fine-grained surfaces. These slickensided layers are sub parallel to the fault plane and are spaced 1 mm to 5 cm apart within the cataclasite (Fig. 2.6A). A 40-30 cm zone of variable grain sizes of cataclasite and does not contain slickensides sits at the bottom of the first fault

core. Serial saw cuts parallel to the kinematic plane reveal mm to cm size low-angle Riedel fractures within the cataclasite (Fig. 2.6B).

Damage zone 1, below the primary fault core, consists of 50-70 centimeters of angular brecciated dacite (Fig. 2.7B). The lower contact with the secondary fault core is sharp and wavy and appears that the cataclasite (below) is injected into the breccia (above) (Fig. 2.7B). The breccia is composed of fractured angular fragments (1- 10 cm) of dacite and yellow/orange/red sulfurous alteration precipitate (Fig. 2.6E). Between the fragments of dacite are spaces that can be void of finer grains of dacite. Within this brecciated zone are small, 2 cm wide shear zones in the Y and R_1 orientation that consist of mm to cm angular clasts of dacite. The general lack of rounding of large fragments, as well as minimal displacements indicate that offset along the fractures was minimal, but some displacement was accommodated along the shear zones within the breccia.

Below this breccia zone, is the secondary fault core that consists of a 60-80 cm thick variable-grain sized cataclasite. Shear planes link Y and R_1 orientations comprised of finer-grained cataclasites (>1-3 mm) within a larger grained cataclasite (1mm to 1 cm of clasts). Each layer of the finer grained cataclasite ranges in thickness from 3 to 10 centimeters. This cataclasite zone does not contain slickensided surfaces. Below this zone is another 20-30 cm layer of breccia identical to the damage zone 1 as described above. Further below this is talus of massive to flow-banded dacite blocks. The Spine 5 fault zone did contain, meter scale fracture pattern similar to Spine 4, however, due to the lack of large exposures, these fractures were not mapped.

2.3.3 Spine 7

2.3.3.1 Spine 7 Macroscopic Field Observations

The exterior of spine 7 exposes a very narrow shear zone that is more ductile in appearance and absent of large-scale brittle fractures and zones of breccia characteristic of Spines 4 and 5 (Fig. 2.8). The intact fault surface that accommodated the extrusion of Spine 7 outcrops west of Spine 5 exposes a 15 x 30 meter fault surface that strikes north/south and dips about 80° to the east (Fig. 2.8A). The fault surface is undulating, smooth and covered with well-indurated planes with slickenside lineations with average orientations of 46°→038 and ranges from 37°→033 to 60°→040 (Fig. 2.2C). Most notably, the Spine 7 shear zone is comprised of layers of ultra-fine grained dark grey to black cataclasite with an aphanitic matrix (Fig. 2.8B). The details of these textures are discussed below. The interior of the spine has a random array of large-scale fractures from cooling and post extrusion settling. On the upper north side of the fault surface at location 'C' in Figure 2.8A, fracture-free dacite outcrops just below cataclasite, where the black layer is absent. This dacite exhibits a foliation defined by the alignment of phenocrysts within a microcrystalline groundmass. This foliation is oblique (P) to the shear plane and is consistent to the known extrusion direction (→ X, Fig. 2.8B-C).

2.3.3.2 Spine 7 Fault Cross Section and Log

One detailed 2x1.5 m grid map on an exposed crack of the kinematic plane of Spine 7 was produced (Fig. 2.9) and included along strike field observations that are complied to complete a summary log (Fig. 2.11C). The narrow shear zone of Spine 7 is comprised of four different types of shear zone (fault) rocks: 1) indurated gouge, 2) grey, foliated cataclasite,

3)ultra-fine grained, aphanitic, black, foliated cataclasite and 4) foliated dacite. Although there is variation in thickness, occurrence and contacts between these facies, the Spine 7 shear zone comprises a foliated cataclasite. Foliation is parallel to the fault plane and is defined by variation in the color and grainsize of the indurated gouge, grey to black fine-grained cataclasite and flow banded dacite. We describe the variation of contacts between these fault facies and then describe each unit in detail.

The contact between the indurated gouge and the ultra-fine grained black cataclasite varies in geometry along strike. It can be quite sharp (Fig. 2.10C) and faulted by low-angle R1 shears, resulting in a saw tooth pattern (Fig. 2.9). It also can be undulating whereby the boundaries looks like a semi-turbulent wave interaction/mixing (Fig. 2.10B). Rip-up angular clasts of the underlying black layer is abundant within the overlying cataclasite and gouge, highlighting the developed fault fabric as exhibited by the P and S fabric geometry (Fig. 2.10A). The contact between the black foliated cataclasite and the underlying dacite varies along strike from distinctly sharp (Fig. 2.10C) to more gradual whereby the gradation is defined by varying layers of black and grey foliated cataclasites. Ultimately, there is a defined boundary between the grey dacite, and foliated cataclasites (Fig. 2.10D).

At the exterior of the spine, the gouge has similar components to Spine 4 and 5 with the addition of sub-angular to rounded clasts of black-cataclasite. The thickness of the gouge varies from 0 to 20 cm and contains fewer slickenside layers within the gouge than observed in Spines 4 and 5. Where present, the slickenside layers are 1-3 mm thick. The gouge transitions down into a cohesive light grey to pink cataclasite with a foliation defined by the alignment of clasts and the development of a fault fabric with a defined shape fabric (Fig. 2.10A,C). The cataclasite has the same componentry of the gouge, also including variably

angular 5-10 mm fragments of darker grey and black cataclasite. The cataclasite ranges in thickness from 2-6cm and contains shear fractures in R_1, R_2 and Y orientation (Fig. 2.10A).

Along strike, the thicknesses of the foliated grey to black cataclasite vary from 1-30 cm (Fig. 2.10 B-E). The grey and black cataclasite layers are distinguished from one another based on field observation color, and noticeable grain-size variation whereby the black unit has an aphanitic matrix and (~5%) sub-rounded phenocrysts. There are stretched white lineations that are parallel to the Y-shear plane. These white bands are also consistently parallel to the slickenside lineations on the surface of the fault and therefore are also parallel to the extrusion direction of Spine 7. The dark black cataclasite layers ranges in thickness from 1-30 cm. The white lineations range in thickens from <1-3 mm and are 3-50 mm in length (Fig. 2.10D). Some lineations are folded where the axial plane is parallel to the P shape fabric and provide consistent kinematic indication of shear (Fig. 2.10E). While there are no large scale fractures observed, there are small < 1mm in thickness Y-shear fractures within the ultra-fine grained black layers that have a rough surface and propagate from stretched white plagioclase lineations. These fracture surfaces extend along strike from a few mm to a few centimeters. There are also en echelon S-shaped tension gashes that occur in groups and are spaced 2 mm apart that dip toward the extrusion direction.

Near the bottom of the foliated, black to grey cataclasite zone, foliation is also defined by color banding of light grey to dark grey. These grey bands have fewer stretched lineations of plagioclase and have more competent subhedreal phenocrysts. The boundary between the black and grey zones is defined by a semi-gradual or sharp transition that then grades into dacite with a P-shape fabric that is defined by the alignment of euhedral phenocrysts of plagioclase, orthopyroxene, amphibole (Fig. 2.10C-D). This zone of foliated grey to black

cataclasite grades into lighter grey, dacite (Fig. 2.10D). The grey dacite just below the foliated cataclasite zone (black to grey cataclasite) exhibits a foliation defined by alignment of phenocrysts that are oriented obliquely to the shear zone foliation. The talus of the Spine 7 consists of large blocks of massive to flow-banded dacite.

2.3.4 Comparison of Spines 4, 5, & 7

Figure 11 is a summary comparison of the macroscopic structures, textures and fault rocks observed in Spine 4, 5 and 7. Thicknesses and textures of the fault core and damage zone vary not only from spine to spine but also along strike of the fault plane (Table 2.2). Spine 4 exhibits one main fault core that ranges in thickness from 0.21 – 1.6 meters of grain size-reduced fault gouge and cataclasite that is interbedded with ultra fine-grained slickensides. Spine 4 has a large damage zone comprised of variably fractured dacite that is 0.4-1.7 meters thick. The total conduit fault thickness varies 0.6-3.3 meters. The Spine 5 conduit fault zone consists of one primary fault core 1.01-1.5 meters and a secondary fault core 0.6-0.8 meters that separate two damage zones of 0.5-0.7 meters and 0.2-0.3 meters. Similar to Spine 4, the conduit fault zone is primarily all brittle structures. The Spine 5 total conduit fault thickness is therefore 1.71-2.5 meters. In contrast to the variety of brittle features observed in Spine 4 and 5, the Spine 7 shear zone exhibits no large-scale damage zone, and is comprised of a foliated cataclasite. Therefore, the Spine 7 shear zone ranges from 0.03-0.6 meters in thickness with no appreciable damage zone. All fault gouges in all spines contain thin ultra-fine-grained indurated surfaces of slickensides.

Table 2.2. Field Summary of Fault Thicknesses. Field observations of minimum and maximum thickness of fault rocks, interpreted fault core and damage zone.

	SPINE 4 T_{fz} (m)		SPINE 5 T_{fz} (m)		SPINE 7 T_{fz} (m)	
Fault Rock	min	max	min	max	min	max
Fault Gouge	0.01	2.00	0.01	0.10	0.00	0.20
Ultracataclasite Slickensides	0.001	0.01	0.001	0.01	0.001	0.003
Cataclasite	0.20	0.60	0.40	0.60	0.02	0.20
Mylonite-like	x	x	x	x	0.01	0.20
Breccia	x	x	0.50	0.70	x	x
Cataclasite 2[a]	x	x	0.60	0.80	x	x
Densely fractured dacite	0.20	0.50	0.20	0.30	x	x
Incipiently fractured dacite	0.20	1.20	x	x	x	x
Total Fault Core	0.21	2.60	1.01	1.50	0.02	0.40
Total damage zone	0.40	1.70	0.70	1.00	x	x
Zone	0.61	3.0	1.71	2.50	0.03	0.60

[X] not present or exposed in field

[a] secondary fault core in Spine 5

[b] only cataclasite and fault gouge

[c] fault core and mylonite-like zone

2.4 Microstructural Observations

In this section begins by describing the most-undeformed dacite of the 2004-2008 dome eruption and document the microscopic progression of strain through the damage zone and into the fault core of Spine 4 and Spine 7. The micro-textures document a progression in intensity and timing of deformation, which evolved from the interior of the spine (undeformed) through the damage zone and to the exterior of the spine (the fault core).

2.4.1 Undeformed Dacite

The dacite that erupted from the 2004-2008 eruption is chemically homogeneous with a uniform bulk composition around 65 wt% SiO_2, (Table D.1) (Thornber et al., 2008a). It is almost holocrystalline containing 41-45 % euhedral phenocrysts and of plagioclase, orthopyroxene (hyperthene) and amphibole (hornblend) set in a microcrystalline matrix (Fig. 2.12) (Pallister et al., 2008b; Thornber et al., 2008b). Groundmass microlites (<30 μm) include laths of orthopyroxene hypersthene and plagioclase, Fe and Ti-oxides, tridymite and cristobalite (Fig. 2.12 B&C). The amount of glass (quenched melt) decreased throughout the eruption decreased from 22% in Spine 1 to 13% in Spine 4 and to trace amounts in Spine 5, 6 and 7 (Pallister et al., 2008b). Porosity is distributed within the groundmass as irregular pockets and passageways 100-500 μm in length (Fig. 2.12A) or as small, 1μm spherical vesicles (Fig. 2.12C). Total sample porosity decreased throughout the eruption from 10-15% in Spine 3 and 4 to <6% in Spine 7 (Pallister et al., 2008b).

2.4.2 Spine 4 Microstructures

2.4.2.1 Spine 4 Damage Zone Microstructures

Although the undeformed dacite within 2 meters of the fault core in the field looks undeformed, microscopic observations show that microcracks are pervasive and effectively disrupt the dacite creating significant crack induced dilation (Fig. 2.13). Further from the fault

core/damage zone boundary, the inter-granular cracks utilize flow banding and form along phenocrysts/groundmass boundaries and within the groundmass propagating from porosity pockets (Fig. 2.13C). Closer to the fault core, inter-granular fractures are present in R, X and Y orientations that propagate from centimeters to <100 μm in length (Fig. 2.13A). Consistent within the damage zone, whole phenocrysts of plagioclase, amphibole and pyroxene are densely fractured (Fig. 2.13 B). These intra-granular fractures are present in some phenocrysts and completely absent in others. Many micro-fractures are trans-granular and crosscut phenocryst/groundmass boundaries (Fig. 2.13D). With the exception of micro-cracks, the groundmass texture is igneous and identical to the undeformed dacite (Fig. 2.12C). Overall, porosity increases towards the damage zone/fault core boundary as a result of inter-granular, trans-granular and intra-phenocryst fractures that result in dilation.

2.4.2.2 Spine 4 Fault Core Microstructures

The fault core (i.e. the cataclasite and gouge) is comprised of granular material of broken dacite with a wide range in clast size distribution. Regardless of scale, clasts are sub-rounded to angular fractured and broken phenocrysts and the microcrystalline groundmass is also fractured (Fig. 2.14 A,B,C). In addition to single phenocrysts, whole sub-angular to sub-rounded clasts are present and are comprised of a phenocryst surrounded by smaller matrix materials. Some are fragments of dacite that has not been fully broken apart and have euhedral phenocrysts within variably fractured microcrystalline groundmass.

Other clasts consist of subhedral phenocrysts that are coated with fragmented clasts orders of magnitude smaller. While componentry and variety is identical to the larger clasts described above, the matrix consists of clasts that are orders of magnitude smaller of <50 μm (Fig. 2.14C-F). Grains are fractured, rounded and comminuted at all scales within the gouge. Impingement micro-cracks within grains form at contact points between grains (Fig. 2.14C).

Reduction of grain size and rounding within the matrix-supported gouge and cataclasite is the result of grain-on-grain microcracks and frictional sliding. Fine-grained matrix flows into the microcracks. Trans-granular fractures are present in the R1 orientation. These R1 fractures are manifested as brittle intra-granular microcracks within plagioclase grains and link across the matrix though ductile deformation (Fig. 2.14A). In this case the matrix reveals no brittle texture response showing a difference in mechanical behavior between the finer-grained matrix and the larger, intact phenocrysts. (Fig. 2.14 C).

Strain localization within the indurated gouge is indicated by extreme grain-size reduction that is concentrated in Y-oriented planes that are 1-4 mm thick: these are the cross sectional view of the slickensided surfaces. Foliation within the gouge is defined multiple layers of slickensides, which are composed of much smaller grains (<50 μm) than the surrounding cataclasite and gouge components (Fig. 2.14 D,E,F). Within these grain-size-reduced slickenside layers, further strain localization is concentrated into ultrafine-grained layers are that are <1 μm in width. These planes have an asymmetric grain size distribution with the smallest, sub-micron sized particles at the top of each surface that forms a sharp, straight or slightly undulating boundary with coarser grains above the slickensided surface (Fig. 2.14 E&F). The smallest grain-sizes cannot be determined at the SEM scale, but have a small amount of non-crystalline material (Appendix D, Table D.2). Between the slickenside surfaces are sub layers that are comprised of poorly sorted, sub-rounded <1-50 μm in size.

2.4.3 Spine 7 Microstructures

The exterior of Spine 7 is composed of a narrow shear zone without macroscopic fractures that ranges in thickness along strike. Most notably, black, grain-size reduced layers of cataclasite zones have accommodated extreme strain localization resulting in both brittle

and scale-dependent ductile mechanisms. We describe the three main units that comprise the shear zone: 1) grey dacite with shape fabric foliation (Fig. 2.15C), 2) the ultrafine-grained black to dark grey cataclasite (Fig. 2.15B), and 3) the indurated fault gouge and slickensides (Fig. 2.15A). The protolith dacite is identical in composition and texture as the protolith dacite for spine 4 (Fig. 2.12, Table D-2).

2.4.3.1 Spine 7 Grey Dacite Microstructures

Although in the field grey dacite within 2-30 cm of the black cataclasite possessed few macroscopic fractures and looks igneous in texture with a flow fabric, microscopic observations show that trans-grain cracks are abundant across phenocryst/groundmass boundaries and intra-grain cracks are pervasive in plagioclase feldspars (Fig 2.15C & 2.16B). The flow/shape fabric is defined by the alignment of euhedral phenocrysts, phenocryst trails and lineations of crushed, brittle elongated plagioclase (Fig 2.16A).

The matrix appears, at low magnifications, to be igneous in texture and is composed of euhedral micro-cysts of plagioclase, clinopyroxene and Fe-Ti oxides (Fig. 2.16A). At higher magnification, plagioclase and quartz polymorphs (probably cristobalite) are anhedral (Fig. 2.16C). A bi-modal size distribution of porosity exists within the groundmass as 20-50 μm (Fig 2.16B) pockets or as microporostiy 1-5 μm in diameter within the anhedral groundmass (Fig 2.16C).

2.4.3.2 Black to Dark Grey Cataclasite Microstructures

Spine 7 is unique in that it features an ultra-high, black strain zone (Fig 2.15B). Plagioclase, amphibole, clinopyroxene and quartz phenocrysts are sub-rounded (anhedral) to sub-angular (subhedral) (Fig 2.17A&B). The groundmass of the ultrafine-grained black layers consists of anhedral plagioclase within a quartz-rich amorphous matrix (Fig 2.17D). The darkest black zones contain the least amount of rounded phenocrysts (10-15%) and have

highest amount aphanitic ground mass (85-90%). The dark grey zones possess a higher percentage of subhedral phenocrysts (35-40%) with a microcrystalline to aphanitic groundmass. The lighter grey zones consist of 45-50% euhedral fractured phenocrysts noticeably larger than phenocrysts within the dark grey to black zones (Fig. 2.17).

The macroscopic foliation within the dark grey to black cataclasite zones is defined by stretched and crushed plagioclase in the Y-orientation (Fig 2.17A&B). The plagioclase lineations consist of ~30% porosity and ~70% comminuted, sub-angular to sub rounded fragments of plagioclase and clasts of black cataclasite that range in size from 5-50 μm (Fig 2.17C). Foliation is also defined by alignment of Ti-Fe oxides in the Y-orientation. Kinematic sense of shear is indicated by undulating lineations of crushed feldspars and offset fractured subhedral phenocrysts (Fig 2.17A). Micro-porosity is more abundant in dark grey cataclasite than in the black cataclasite. Fractures exist within the dark black material both cutting across matrix and phenocrysts. These larger fractures aid in the brittle transition into indurated fault gouge.

2.4.3.3 Fault Core: Gouge, Cataclasite and Slickensides

Although the Spine 7 shear zone is drastically different form the Spine 4 fault zone, both spines have layers of indurated fault gouge and ultrafine-grained slickensides within the gouge (Fig. 2.18A). The Spine 7 gouge includes of broken and rounded dacite and black cataclasite clasts. At the lower boundary of the fault gouge, the underlying black cataclasite has thoroughgoing inter-granular fractures that are pervasive and effectively disrupt the dark grey/black cataclasite. Dilation increases between clasts creating the fault gouge, increasing porosity by grains rotating and fracturing (Fig. 2.18B).

The fault gouge of Spine 7 is heterogeneous with sub-rounded to angular clasts of black cataclasite, phenocrysts and aggregates of coated sub-rounded phenocrysts (Fig. 2.18A).

These clastic aggregates are identical to Spine 4 where large phenocrysts that are fractured or rounded coated by clasts orders of magnitude smaller to form rounded clasts of aggregate. The fault gouge phenocrysts can be larger than the black to grey cataclasite below. Impingement micro-cracks within grains form at contact points while finer grains, magnitudes smaller infill the cracks .

The indurated fault gouge also has Y-oriented layers of strain-localized slickensides that are 1-4 mm thick (Fig. 2.18A). Within the slickenside planes, are layers of variably sorted, rounded to sub-rounded grains where the highest strain is elucidated by 20-30 μm layers of ultrafine-grained material (Fig. 2.18C). There is a sharp boundary between the top of the slickensides and the larger-grained layers resulting in an asymmetric grain size distribution where the smallest grains (<1 μm) are at the sharp boundary that gradually grade to the larger grains (up to 100 μm) that exist within a fine-grained matrix (Fig 2.18C). The finest grain size of the slickensides, at the top of each slickenside is sub-micron where grain boundaries cannot be distinguished (Fig. 2.18E). Many of the finest-grained slickensides are crosscut by Riedel shear fractures (Fig. 2.18D). The finest grain size of the slickensides, at the top of each slickenside is sub-micron and no grain boundaries can be distinguished (Fig. 2.18E).

2.5 Summary of Conduit Fault Features

2.5.1 Mode of Failure / Deformation Mechanisms

In all spines, deformation within shear zones is micromechanically brittle, which is a confining pressure-dependent processes. Brittle faulting, extensional fracturing and cataclastic flow of material, including localized, rapid slip to create layers of ultrafine-grained slickensided surfaces are the primary mechanisms that accommodated displacement. This is

despite the fact that the surface temperature of the gouge was measured at 730 °C (Cashman et al. 2008). Typically, in silicates, moderately high confining pressure of > 200 MPa are required to induce true crystal plasticity (i.e. the creation and movement of dislocations through a crystal lattice). At MSH, the dacite magma is fully crystallized and therefore transitioned into a competent rock at 1 km depth. Deformation by brittle processes rather than by plasticity is explained by the combination of low confining pressure and fast strain rates (see next section).

Grain size reduction is therefore achieved through brittle grain boundary fracturing forming a 0.6 to 2 meter wide fault core that accommodates the majority of the 1 km displacement. Further grain size reduction can result from extreme localization of strain within the fault core along very thin planes that produce the ultrafine-grained slickensided surface or the ultrafine-grained black cataclasite. Amorphous material also occurs at the top of the ultrafine-grained, well-indurated slickensides and within the ultrafine-grained black cataclasite in Spine 7 (Appendix D). This ultrafine-grained, non-crystalline material is the result of localized shear and comminution. These surfaces could become well indurated and polished due to the excessive heat present within the conduit.

We propose that the solid rock composed of aphanitic, amorphous material found locally in the Spine 7 shear zones (i.e. the black aphanitic fault rock), represents ultrafine-grains of rounded dacite that was subsequently ‘sintered’ in the lower conduit by the high ambient temperatures in the conduit. A slower ascent rate in combination with a thinner zone of localization could result in sintering of the high surface area material.

2.5.2 Strain Variation within Each Spine and Throughout the Eruption

All conduit fault zones mapped exhibit a primary fault core, characterized by cataclasite and fault gouge with extreme grain size reduction and rounding of broken dacite, all of the same composition. Observed deformation is accommodated within the dacite with some interaction with the wall rock where the dacite to fault gouge is essentially the same composition (Appendix D). However, as the eruption continued, the conduit faults narrowed and changed in style (Fig. 2.11). The Spine 4 conduit fault contains a large damage zone that possesses various intensities of fracture distributions and a thick foliated fault core with numerous parallel y-shear, ultra-fine grained slickensides. Spine 5 fault contains a large damage zone that is cut by a secondary fault core of a weakly foliated cataclasite. The primary fault core is at the margin comprises foliated cataclasite with parallel Y-shears, ultrafine grained slickensides. The spine 7 conduit fault consists of a narrow foliated fault core of cataclasite and indurated gouge with no appreciable damage zone.

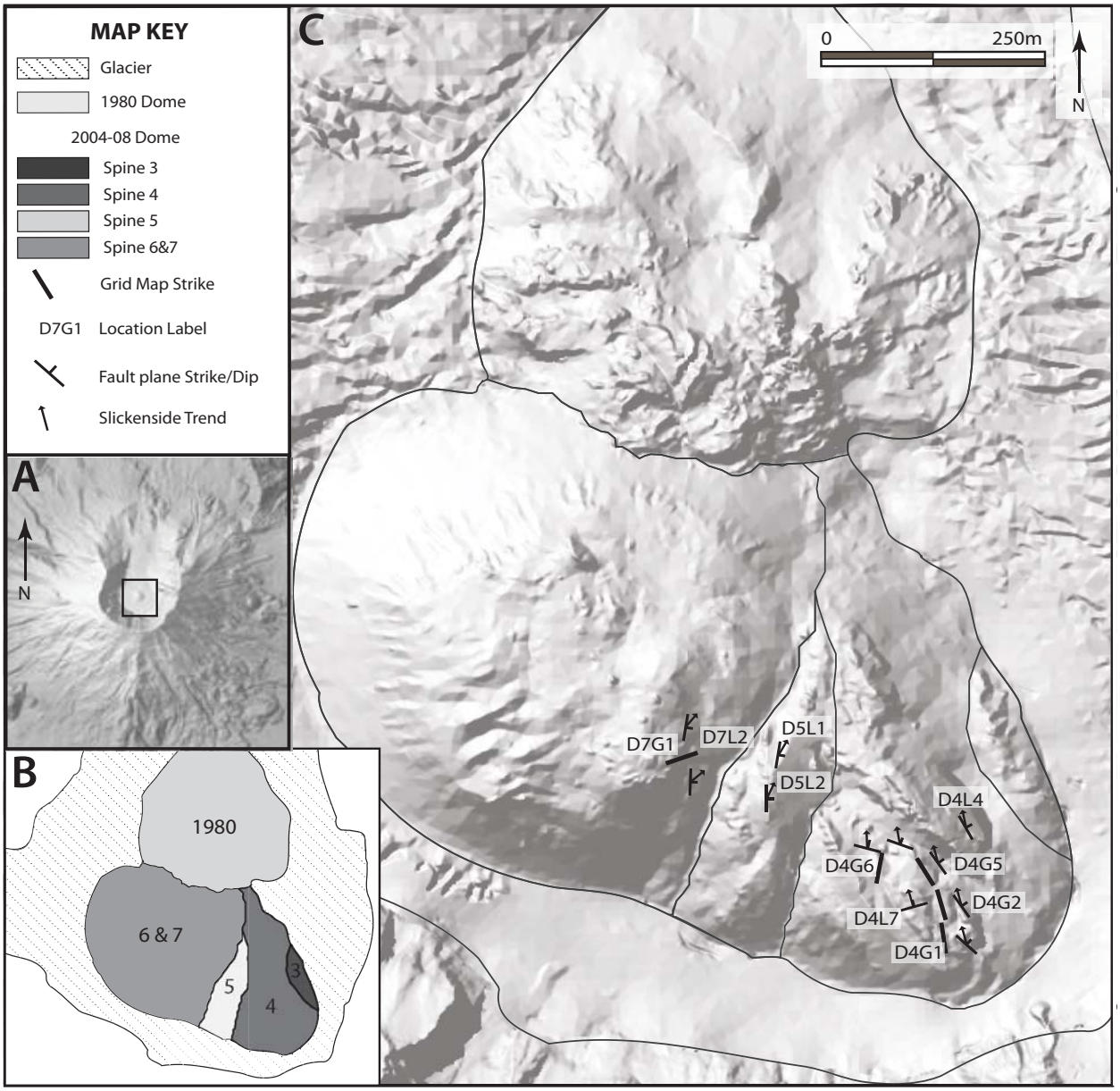

Figure 2.1. Crater Map Overview. (A) Hill shade of a digital elevation model (DEM) of Mount St Helens, Washington, Latitude and Longitude: 46.2º N, 122.2º W/ Elevation of crater rim: 2,549 m (8,363 ft), elevation of crater floor: 1,913 m (6,276 feet). Black box indicates the boundaries for crater maps, B & C. (B) Map of the inside of the crater outlining the locations and boundaries of material (both talus and intact outcrops of spines) erupted throughout time: i. 1980 dome is comprised of all eruptive products from 1980-86. ii: The current 2004-2008 surface eruptive products are divided into four units centered around the distinct solid dacite spine: Spine 3 (Oct 27, 2004-Dec 14, 2004), Spine 4 (December 14, 2004-April 14, 2005), Spine 5 (April 15, 2005-July 23,2005) and Spine 6 &7 (July 24, 2005-January 2008). (C) A hill shared DEM map to highlight the topography of the interior of the crater. See B for dome, glacier and spine boundaries. Symbols noted in the key represent selected structural data of local fault planes of intact outcrop, slickenside lineations and orientation of grid maps were the dip is sub-vertical (example D4G1).

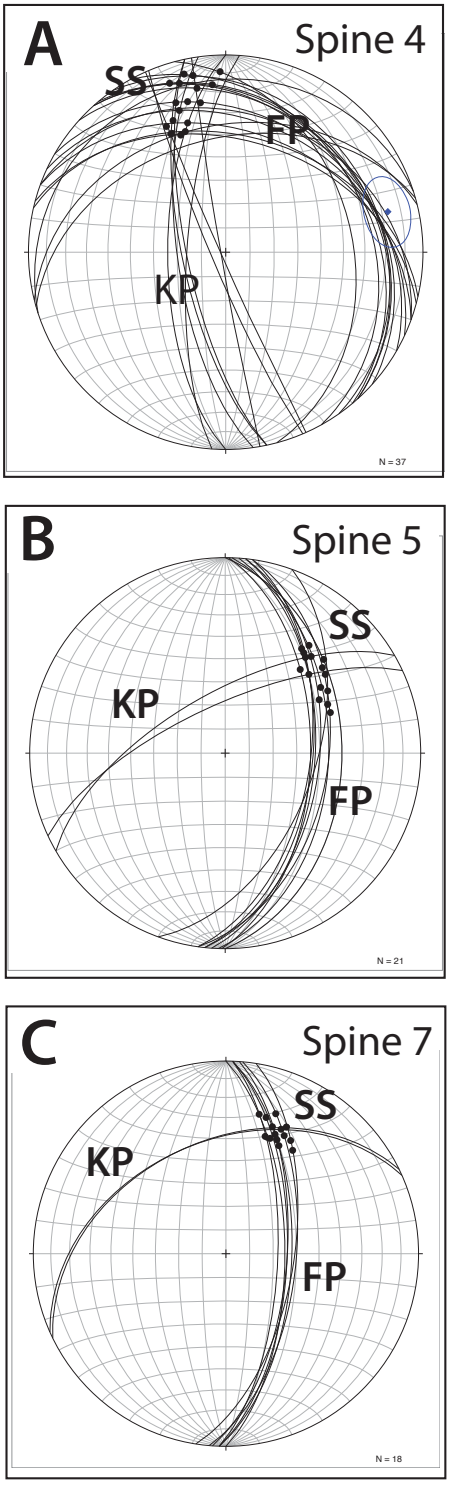

Figure 2.2. Kinematic Plane Solutions of Spine 4,5,7. Summary of structural data including measured fault planes (FP), slickensides (SS) and solutions to the local kinematic plane (KP) for each location displayed by spine. See Figure 2 and Table 1 for specific locations and details. (A) Spine 4 data. Note the variety of orientations of fault plane striking 312°Az to 335°Az due to the available outcrop encompassing the cylindrical nature of the extruded spine (Figure 4D). (B) Spine 5 data summary of local fault plane from one, excellent, planar outcrop striking 000°Az to 009°Az. (C) Spine 7 structural data summary of fault plane striking 002°Az to 010°Az

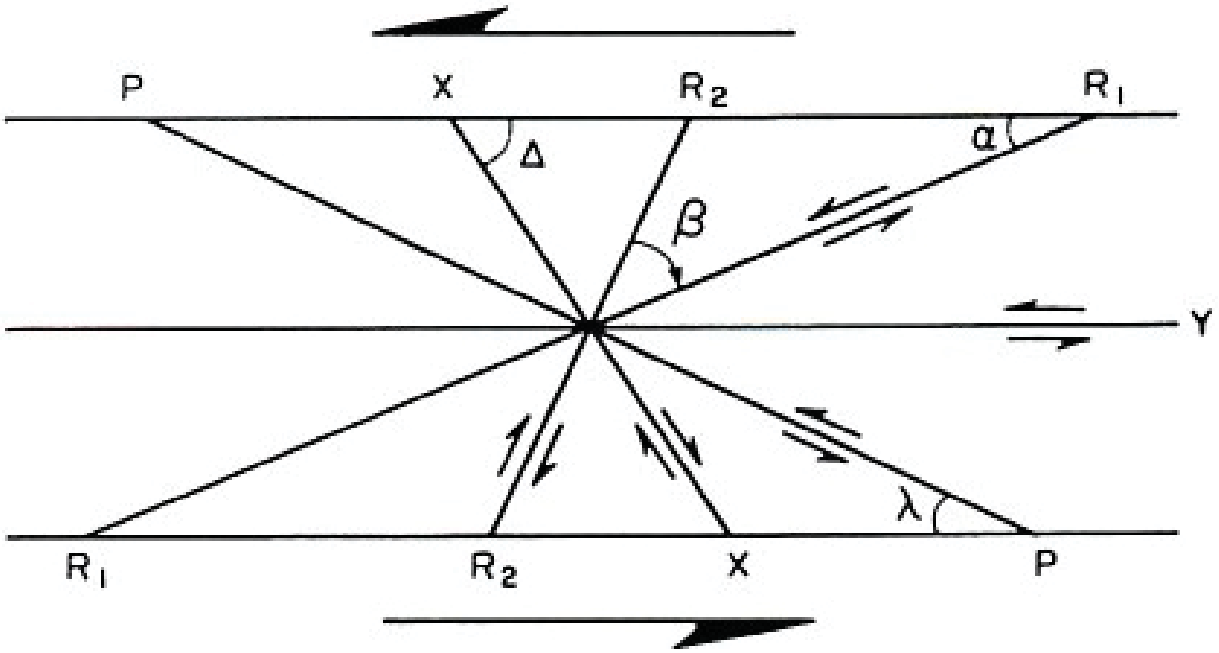

Figure 2.3. Riedel Shear Zone Terminology. Schematic diagram showing the various orientations of shear localization, and kinematic shear sense in typical experimental and natural shear zones (Logan et al. 1979).

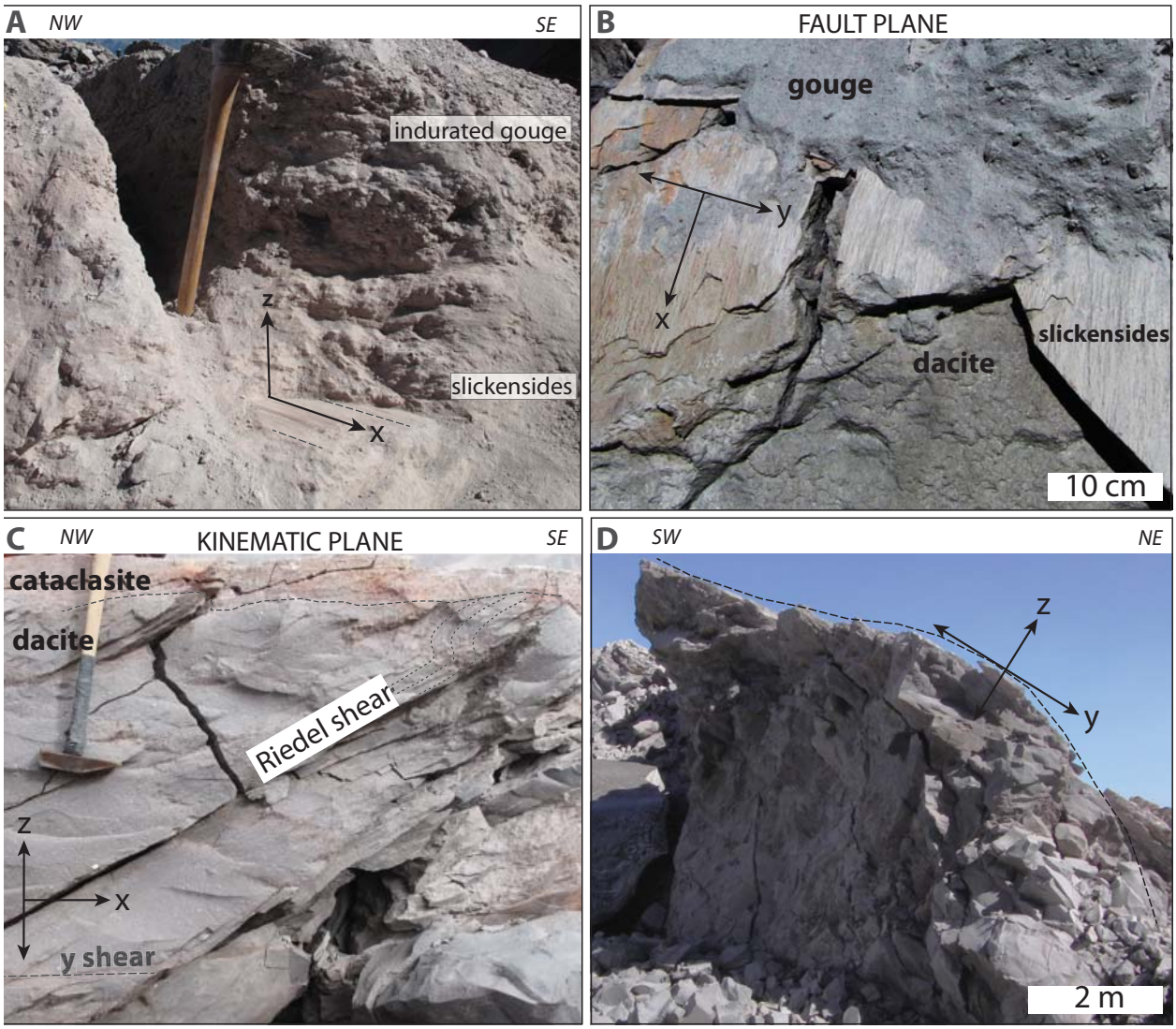

Figure 2.4. Spine 4 Field Observations. (A) fault gouge and indurated fault gouge that is interbedded with numerous surfaces of smooth, indurated slickenside surfaces. View looking (NE) oblique to the kinematic plane (x/z) of Extrusion direction marked by strain axis, x, to the southeast, as explained in Figure 1.3 (B) Fault plane (x/y) view of loose, unconsolidated gouge above cataclasite with numerous layers of thin indurated slickenside surfaces. Beneath the cataclasite is the scoured and rough surface of competent dacite. (C) Cross section example of the kinematic plane (x/z) at D4G4, with fractured cataclasite on top of fractured dacite. The fractured dacite, the damage zone, is comprised of meter scale y shears, riedel shears, and folded riedel shears. Extrusion direction is to the southeast, noted by the x-axis. (D) Cross section view perpendicular to the strike of long axis (y/z plane) of spine 4 revealing 10 m of exposure of fractured and friable dacite. Spine 4 has a curviplanar exterior covered in fault cataclasite and gouge highlighted by the dotted line.

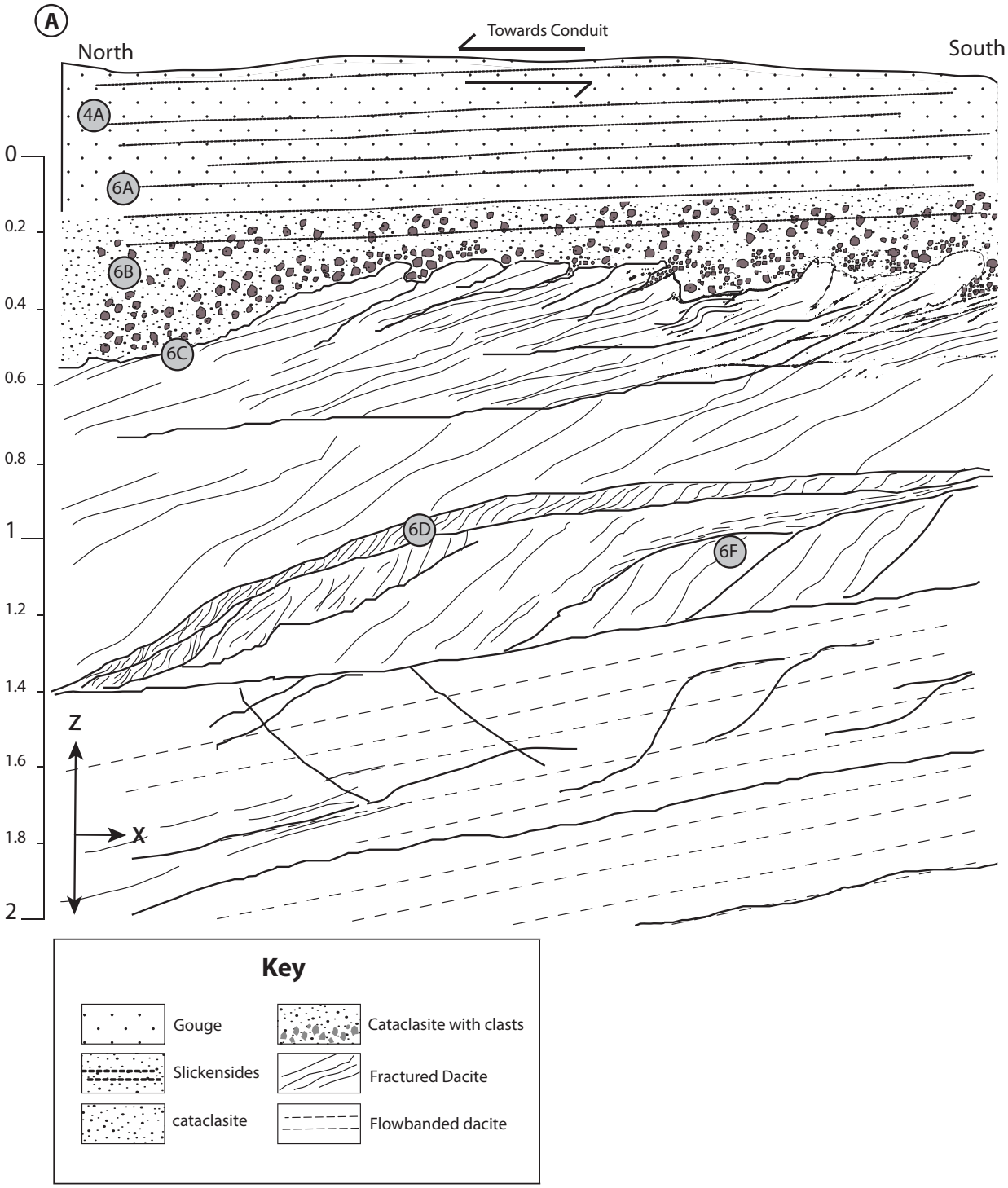

Figure 2.5. Spine 4 Kinematic Plane Map. (A) Sample grid map at location D4G2 (see Figure 2) of an exposed cross section oriented 165/85W that is essentially the local kinematic plane (x/z) of the fault zone. This map shows the transition from flow-banded dacite to the unconsolidated gouge at the margin of spine 4. The extrusion direction is noted by the fault arrow is to the south. Circled labels refer to locations of photos shown in Figure 2.6.

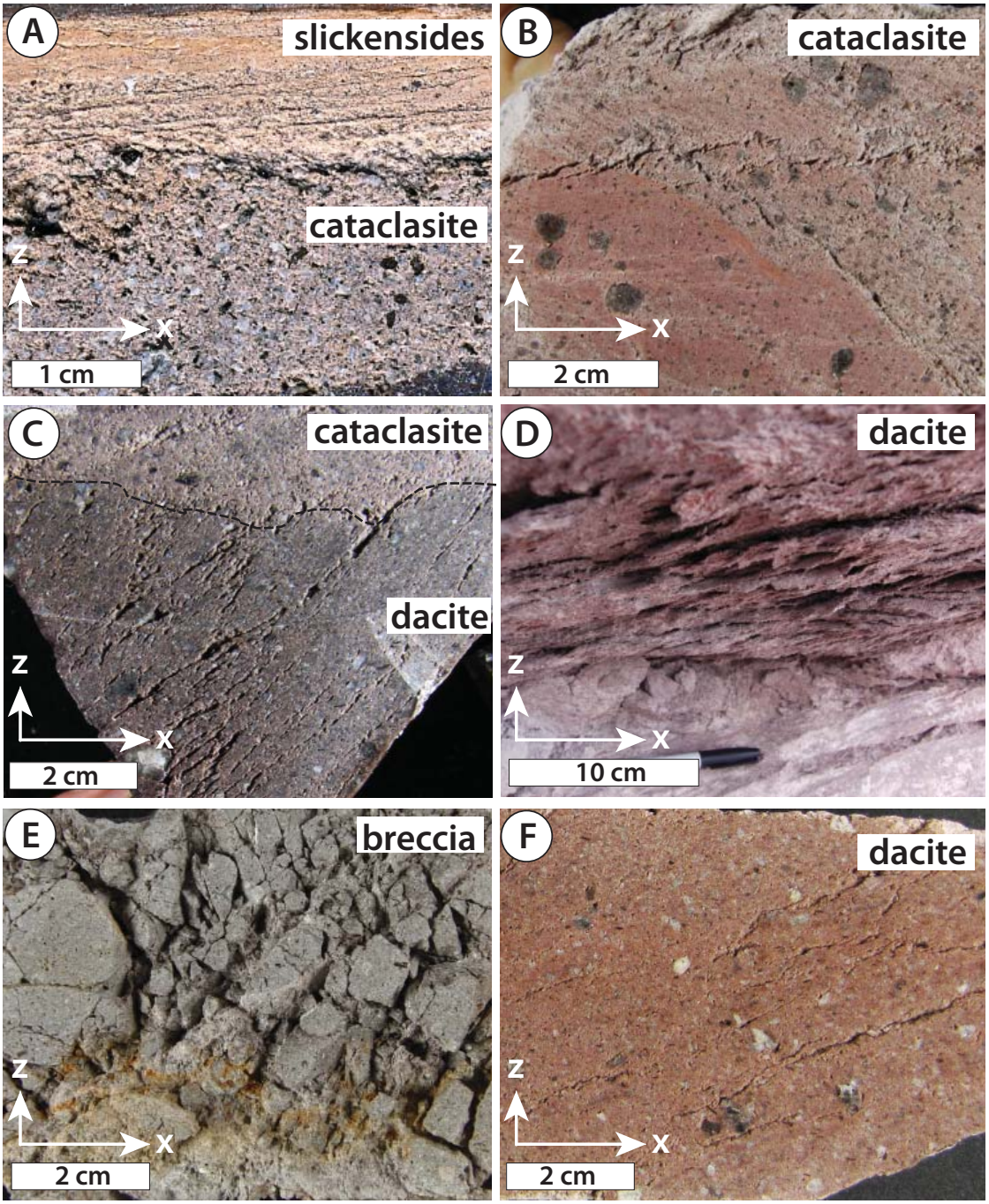

Figure 2.6. Spine 4 and 5 Hand Sample Photography. Hand sample textures from spine 4 and 5 cut in the local kinematic plane (x/z) of each sample. Extrusion direction is to the right noted by each x-axis arrow. Locations of samples noted in Figures 2.4 (A) Cross section of fine grained, layers of slickensides that define a foliation within the a cataclasite/indurated fault gouge. (B) Small, cm size riedel shear fractures within the poorly sorted, sub-rounded, non-foliated cataclasite with secondary red stain (mineralization) of from gas activity? (C) Cuspate boundary between cataclasite and fractured dacite. A high-density fracture network of riedel fractures (both R and R') is present in the dacite while a few riedel fractures cut the cataclasite. (D) Dacite with successive riedel shears spaced millimeters apart concentrated between two y-shears. (E) Angular brecciated dacite with a zone of yellow precipitate with network of pore space along fractures. (F) Dacite with a y-shear surface at the top and small cm size riedel and y shear cracks.

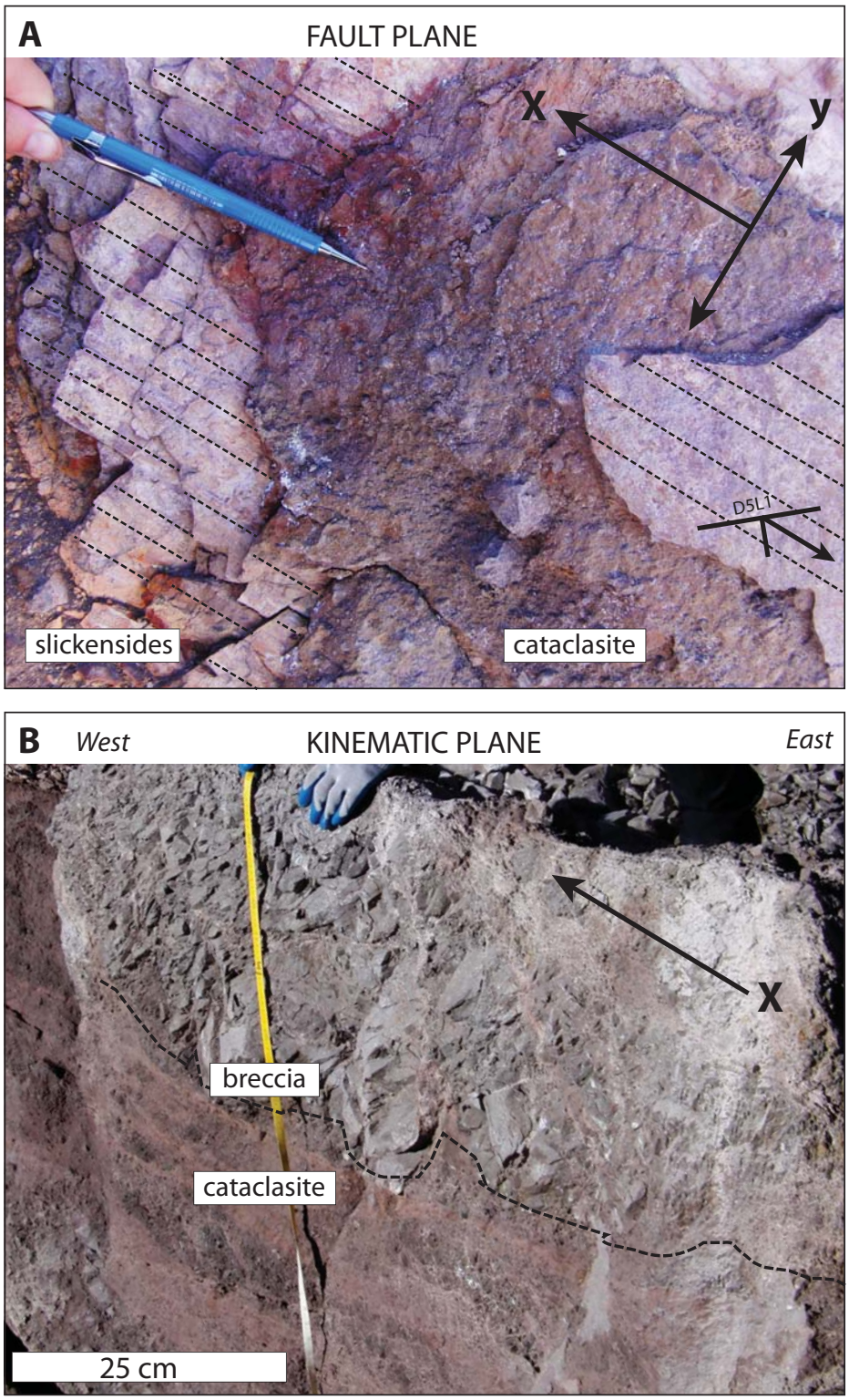

Figure 2.7 Spine 5 Field Observations. Field photos of spine 5 at D5L1 (Fig. 2). (A) Fault plane view above 5B of numerous layers of slickensides interbedded with sub-angular layers cataclasite. (B) Sub parallel to local kinematic plane. A layer of angular-breccia on top of layers of variably rounded and sized cataclasite with a cuspate boundary.

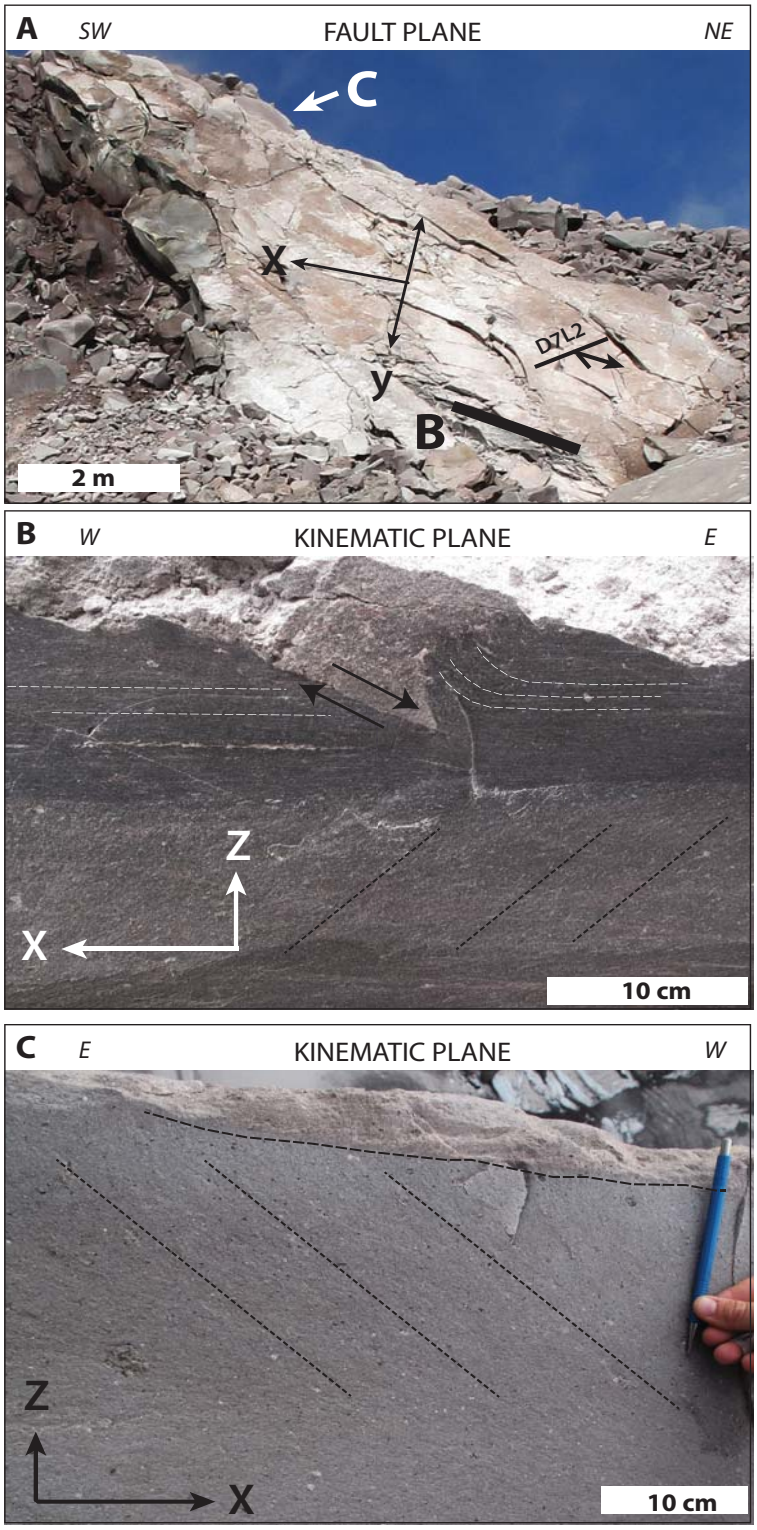

Figure 2.8. Spine 7 Field Observations. (A) Intact outcrop of spine 7 (D7G1 in Fig. 2.1). The smooth surface is the undulating exterior of the spine's fault surface oriented 009/60 E. Extrusion towards the west noted by the x-axis. B marks the location of figure 2.8B and grid map of Figure 2.9. The C marks the location of 8C. (B) The kinematic plane, looking south, at location 'B' with saw tooth contact between grey, variably consolidated cataclasite and black, low-porosity cataclasite. Flow-banded dacite with a shape fabric is located below the dark black layer. Extrusion is to the west noted by →X (C) Kinematic plane, looking north, at location 'C' of flow-banded dacite overlain by indurated fault gouge. Extrusion to the west is noted by →X.

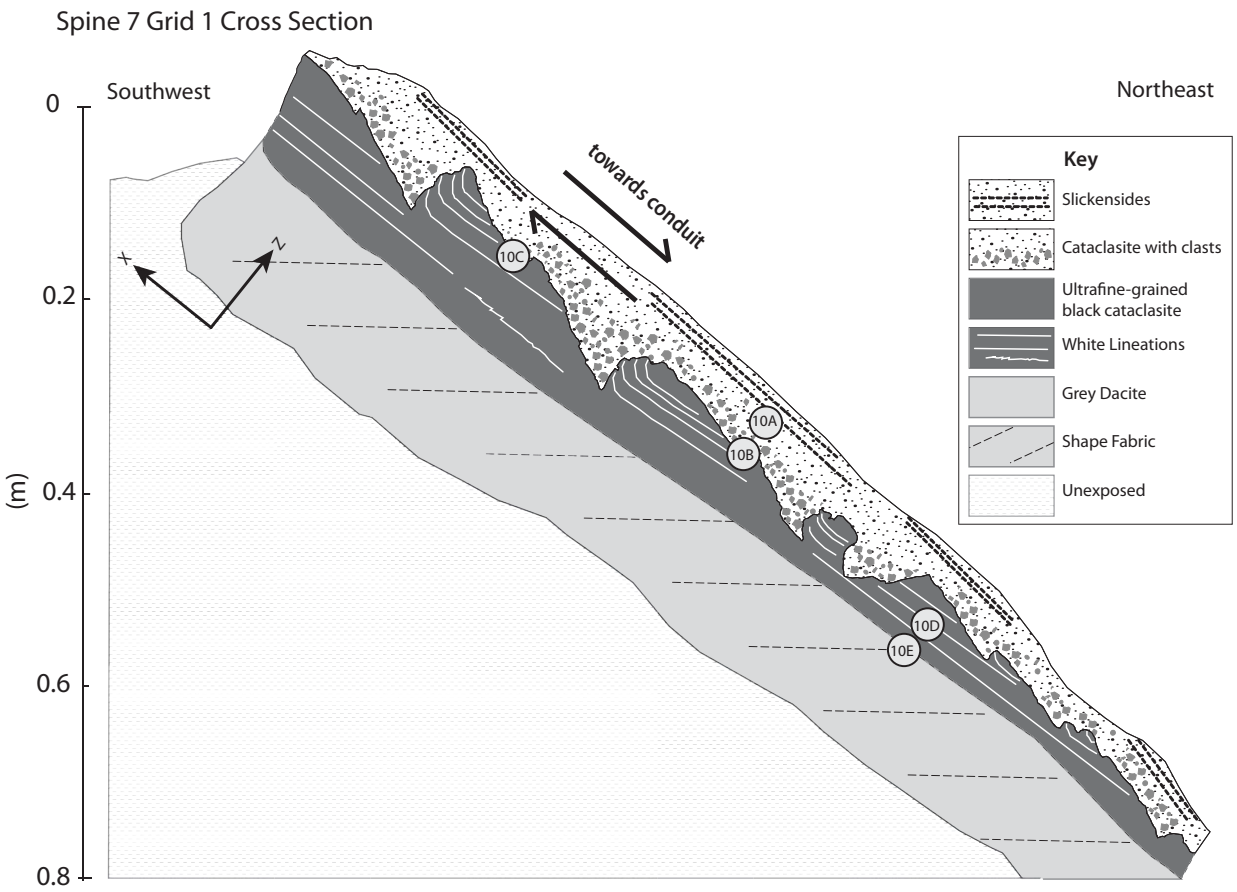

Figure 2.9. Spine 7 Kinematic Plane map. Spine 7 grid map at location D7G1 (see Fig. 2.1 and Fig. 2.8A) of a cross section, sub parallel to the local kinematic plane (x/z) 240/65 NW. Extrusion direction noted by the fault arrows and →X, is to the west. Grey circles note the locations of photographs in figure 2.10.

Figure 2.10. Spine 7 Hand Sample Photography. Spine 7 hand sample images cut to the local motion plane of 240/65 NW (Table 1) and re-oriented to fault orientation where the extrusion direction is noted by→X. (A) Cataclasite with C and S fabric developed across a foliation defined by layers of black cataclasite and pink cataclasite. (B/C) Serial saw cut sections of the same sample to reveal variation of contacts and textures between and within the indurated fault gouge, the grey to black ultrafine-grained cataclasite and the transition to the grey dacite. The boundary between the indurated fault gouge is cuspate and can be "fluid-like" and undulating (B) or distinct (C). The dark grey to black cataclasite is variable along strike and contains sub-rounded phenocrysts within a grey to black aphanitic matrix. Foliation is defined by elongate discontinuous white lineations of plagioclase cataclasite. (C) Along strike variation contact of grey-black cataclasite that is semi-gradational into grey dacite. The dacite has a weak to moderate shape fabric noted by the dashed lines. Black to grey layers are distinct, and have a foliation defined by stretched plagioclase. In the darker cataclasite layers, the plagioclase lineations are thinner and stretched longer in the direction of extrusion than those in the dark grey layers. (D) Dark grey cataclasite with a foliation defined by the stretched white bands of cataclasite feldspar. Some lineations are folded, exhibiting a shear sense that is consistent with the observed extrusion direction noted by the →X.

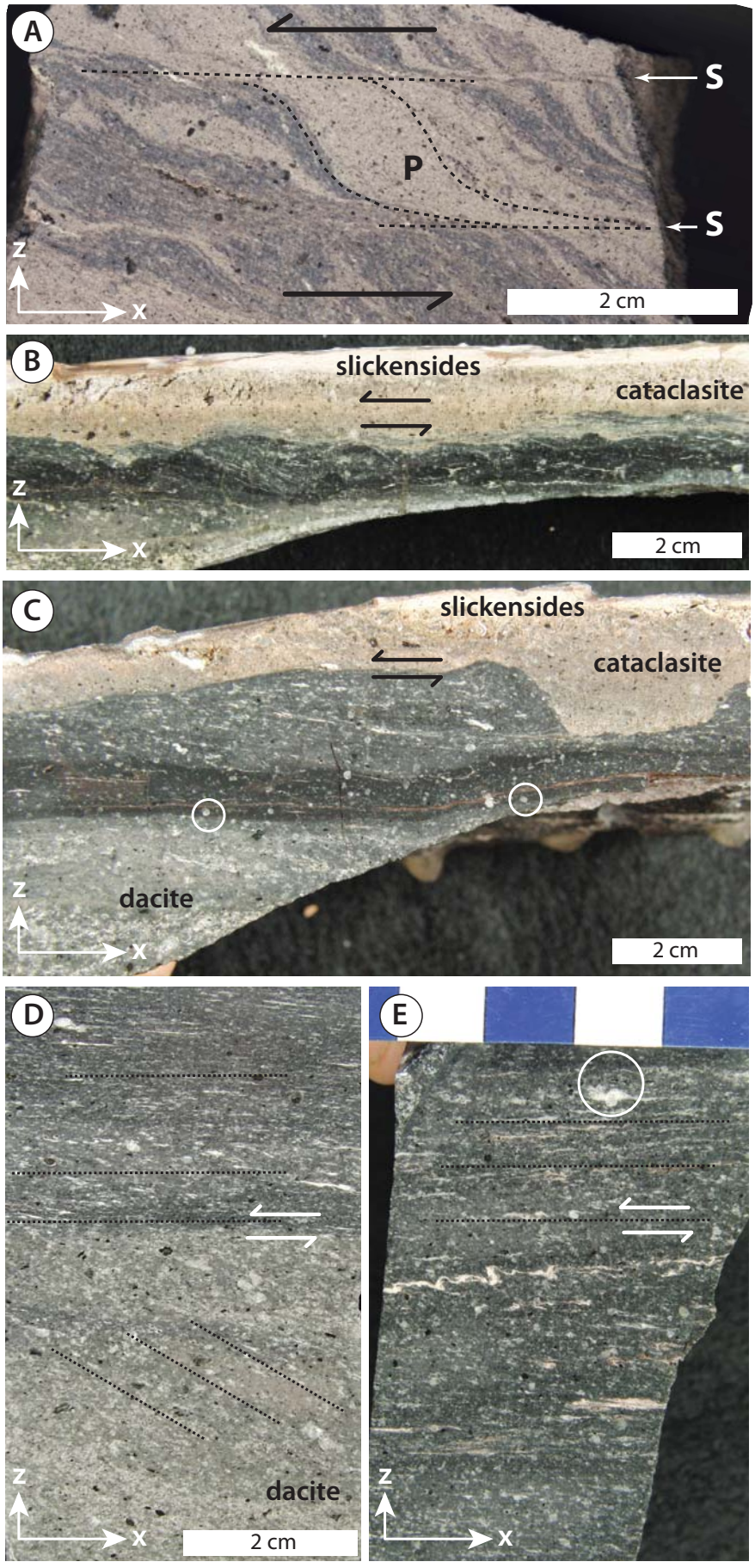
A
S
P
S
z
x
2 cm
B
slickensides
cataclasite
z
x
2 cm
C
slickensides
cataclasite
dacite
z
x
2 cm
D
dacite
z
x
2 cm
E
z
x

Figure 2.11. Spine 4, 5 and 7 Summary Logs. Composite logs summarizing the structures and the progression of fault rocks across the damage zone within the local kinematic plane. Each log is rotated horizontally to position the structures in the same orientation as they developed during the ascent through the conduit (i.e. Fig. 1.3e). The conduit wall is therefore fixed, the total thickness of the fault zones to the conduit wall is unknown due to the symmetrical side of the fault is detached from shear zone and left behind attached to the conduit wall. We can only discuss the evolution of structures observed in the asymmetrical fault zones that is erupted on the exterior of the spines. (A) Spine 4 exhibits one main fault core and a large brittle damage zone (B) Spine 5 is comprised of a primary and secondary fault core between two brittle damage zones and (C) Spine 7 has a narrow shear zone composed of foliated cataclasite and does not have any large scale brittle fractures.

Ⓐ ***SPINE 4***

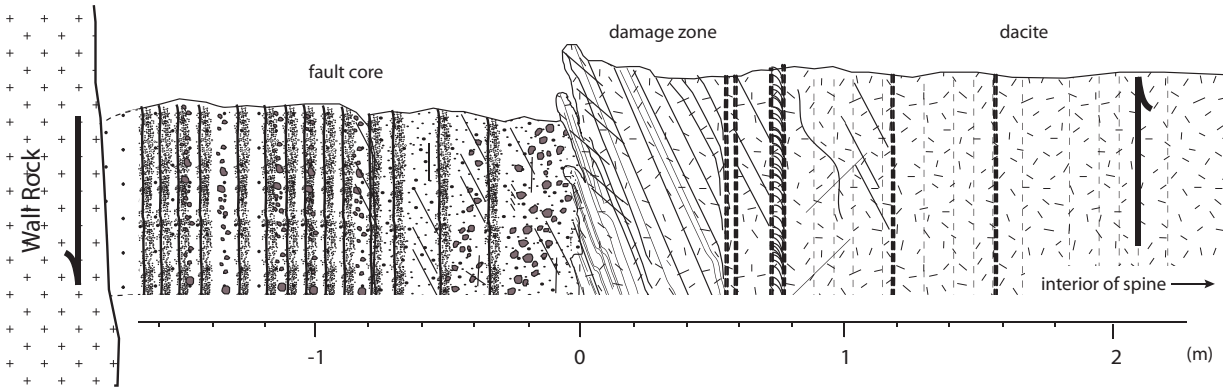

Ⓑ ***SPINE 5***

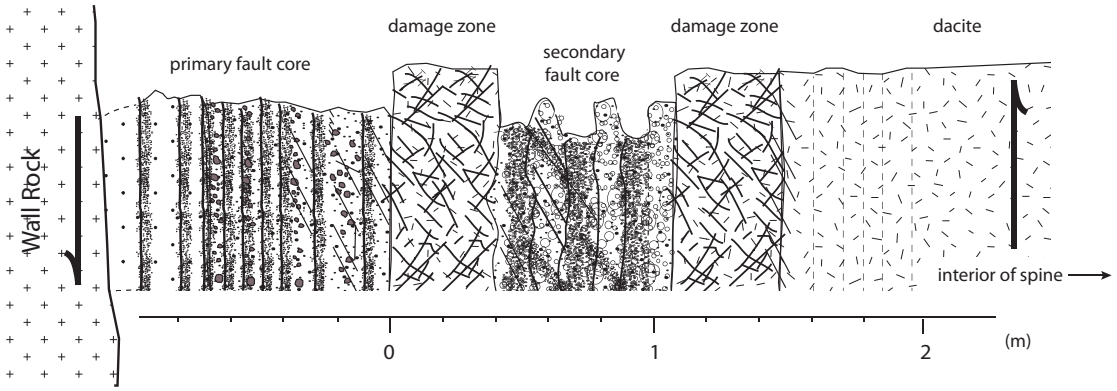

Ⓒ ***SPINE 7***

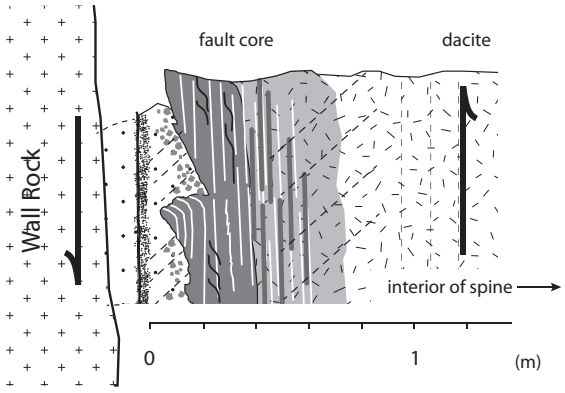

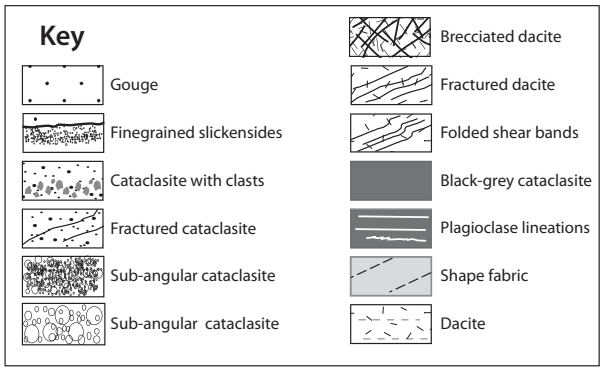

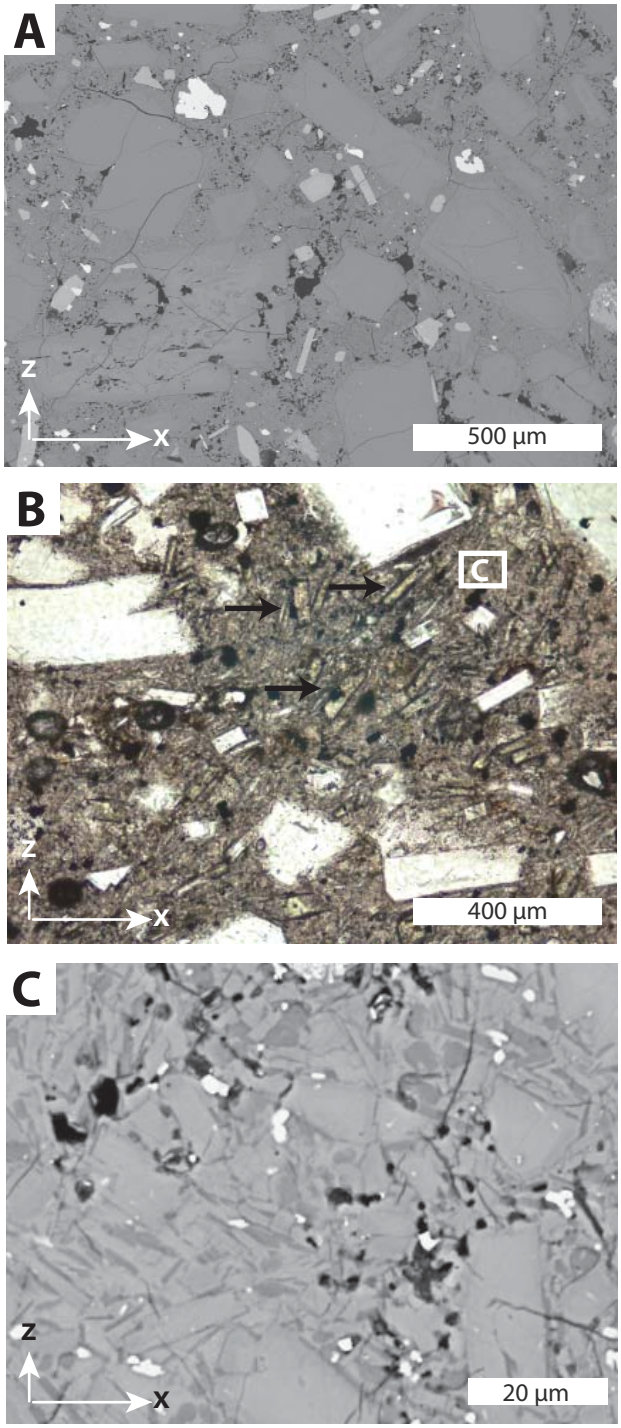

Figure 2.12. Petrography of Undeformed Dacite. Photomicrographs in plane polarized light (A&C) and SEM backscatter images (B&D) of undeformed dacite of the 2004-2008 eruption from Spine 4 (AK10-MSH-D4G1-A). The →X notes extrusion and →Z notes towards the exterior of the spine. (A) Holocrystalline, low porosity (10-15%) dacite with 41-45 % euhedral to subhedreal phenocrysts of plagioclase, amphibole and orthopyroxene (hyperthene) within a microcrystalline groundmass. (B) Porosity is evenly distributed throughout the groundmass as irregular pockets (2-50 µm in diameter) between groundmass microlites and at the edges of phenocrysts. (C) Groundmass is comprised of microlites (<30 µm) and laths of plagioclase and orthopyroxene, tridymite (quartz polymorph), and microlites of Fe-Ti oxides and (D) micro-porosity.

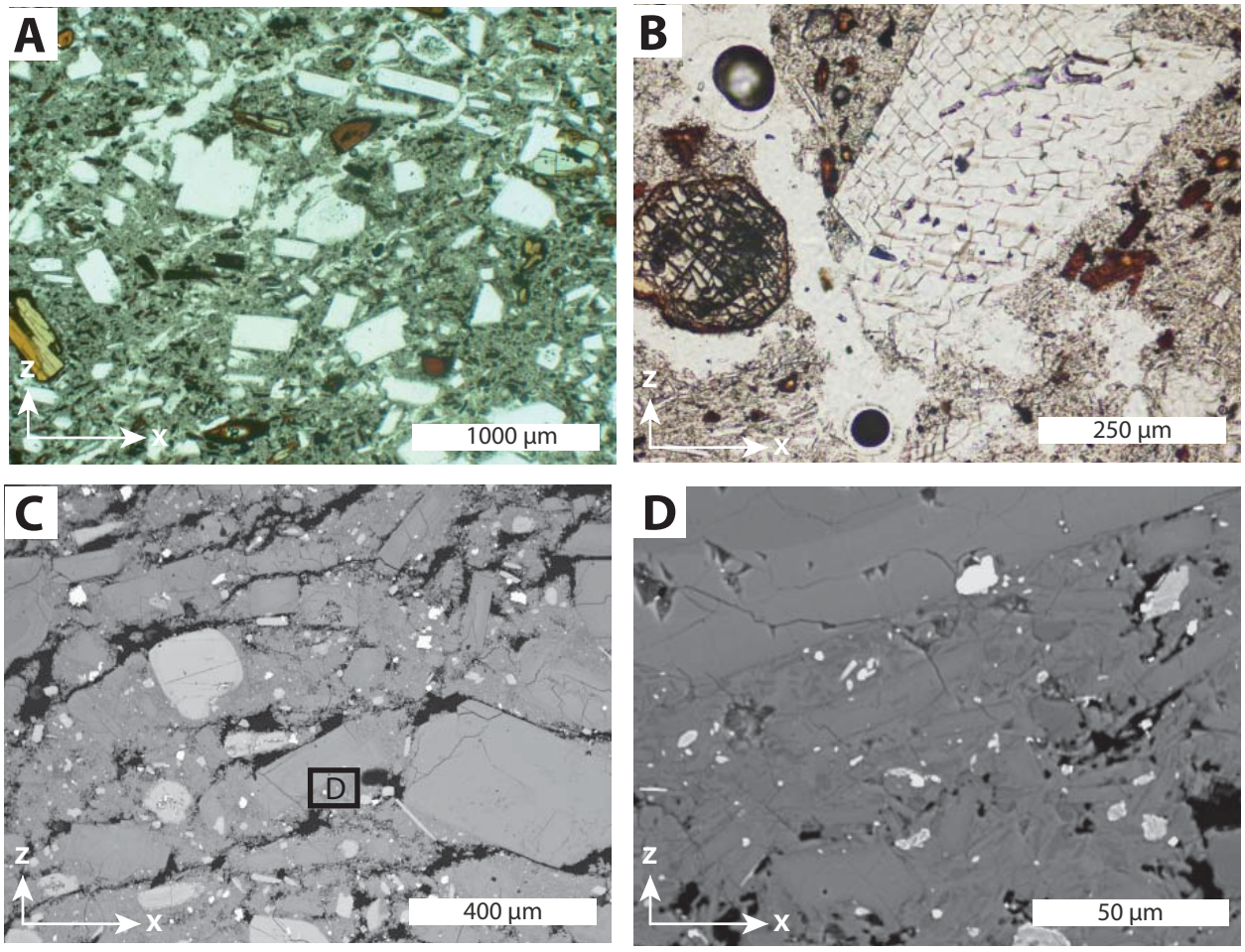

Figure 2.13. Spine 4 Damage Zone Microstructures. Photomicrographs in plane polarized light (B, C&D) and SEM backscatter images (E&F) of selected samples across the damage zone. The →X notes extrusion and →Z notes towards the exterior of the spine. (A) BF10-MSH-D4G1-E with multiple micro-cracks in the R and X orientation. (B) BF10-MSH-D4G1-J weakly flow-banded dacite defined by the alignment of phenocrysts parallel to the →X and incipient fractures in the R orientation. (C) BF10-MSH-D4G1-F fractured plagioclase feldspars within a competent microcrystalline groundmass (D) BF10-MSH-D4G2-C shattered plagioclase and pyroxene within micro-cracks within the groundmass and adjacent to phenocrysts. (E) Detailed image of micro-cracks and dilation between phenocrysts and the groundmass and within the groundmass. (F) Competent groundmass textures of laths of plagioclase, tridymite and pyroxene adjacent to a large plagioclase with pervasive micro-fractures.

Figure 2.14. Spine 4 Fault Core Microstructures. Photomicrographs in plane polarized light (A&D) and SEM backscatter images (B,C,E&F) of selected samples across the spine 4 fault core. Locations are noted in figure 11A. The →X notes extrusion direction and →Z notes towards the exterior of the spine. (A) Photomicrograph of consolidated, matrix-supported cataclasite with sub-rounded to sub-angular phenocrysts of plagioclase and amphibole. A Riedel fracture propagates through the three phenocrysts while the matrix remains cohesive has no visible micro-fractures. (B) Variety of clasts that comprise the cataclasite/gouge. Clasts include single competent phenocrysts ranging in size from > 1 μm to 500 μm, phenocrysts that are coated with smaller grains and rounded grains that contain euhedral phenocrysts surrounded by competent, igneous groundmass with smaller laths. (C) Impingement micro-cracks forming at two contact points between grains within the cataclasite. (D) BF10-MSH-D4G4-E Cataclasite with sharp transition to ultrafine-grained slickensides surfaces that are sub-parallel to the Y-orientation. (E) Close up of slickenside surfaces that reveal extreme grain size reduction at the top surface of the slickensides that grade to coarser cataclasite of sub-angular grains of fractured plagioclase. (F) Close up of extreme grain size reduction of the sharp upper boundary of a single slickenside surface. Note the sharp angular edges and the ultra fine grain breccia filling in the cracks

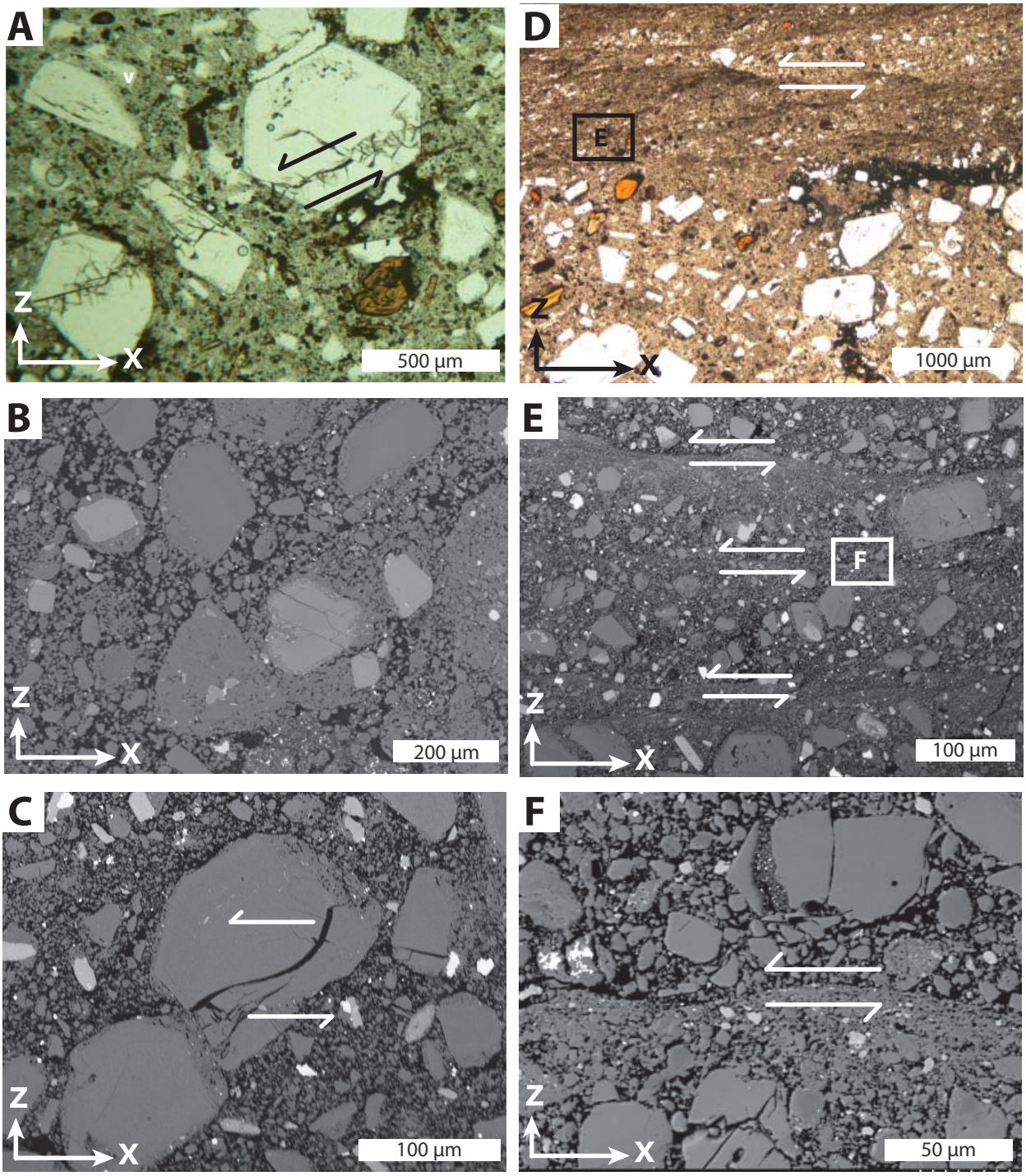
A
v
Z
X
500 µm
D
E
Z
X
1000 µm
B
Z
X
200 µm
E
F
Z
X
100 µm
C
Z
X
100 µm
F
Z
X
50 µm

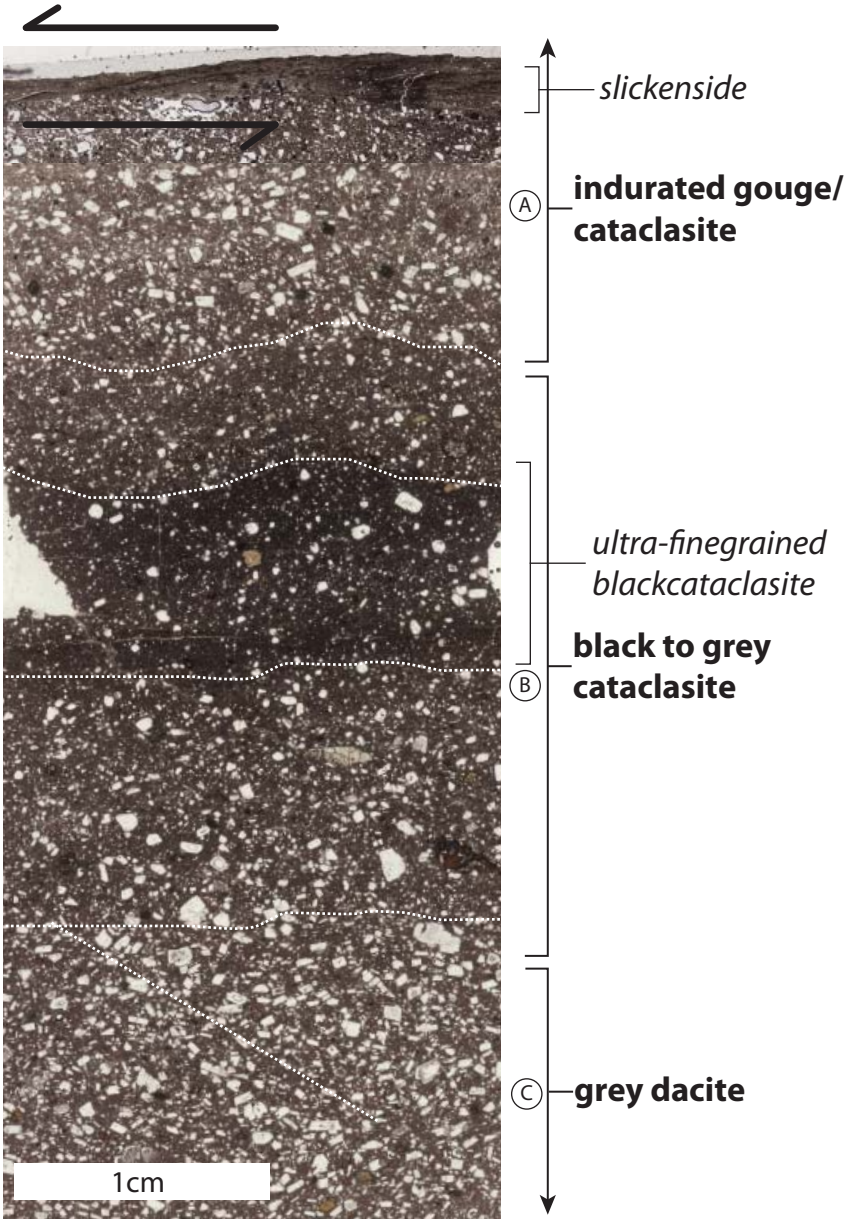

Figure 2.15. Spine 7 Thin Section Scan. Thin section scan highlighting the following facies described in the text (C) grey dacite, (B) ultrafine-grained black cataclasite, (A) cataclasite/gouge/slickensides. Zones grain size reduction and grain rounding within a (B) narrow zone producing ultrafine-grained black to dark grey cataclasite in comparison to the (C) grey dacite below and (A) indurated gouge and light-pink cataclasite above. This thin section scan illustrates the reduction in grainsize accommodated in the slickensides and black cataclasite.

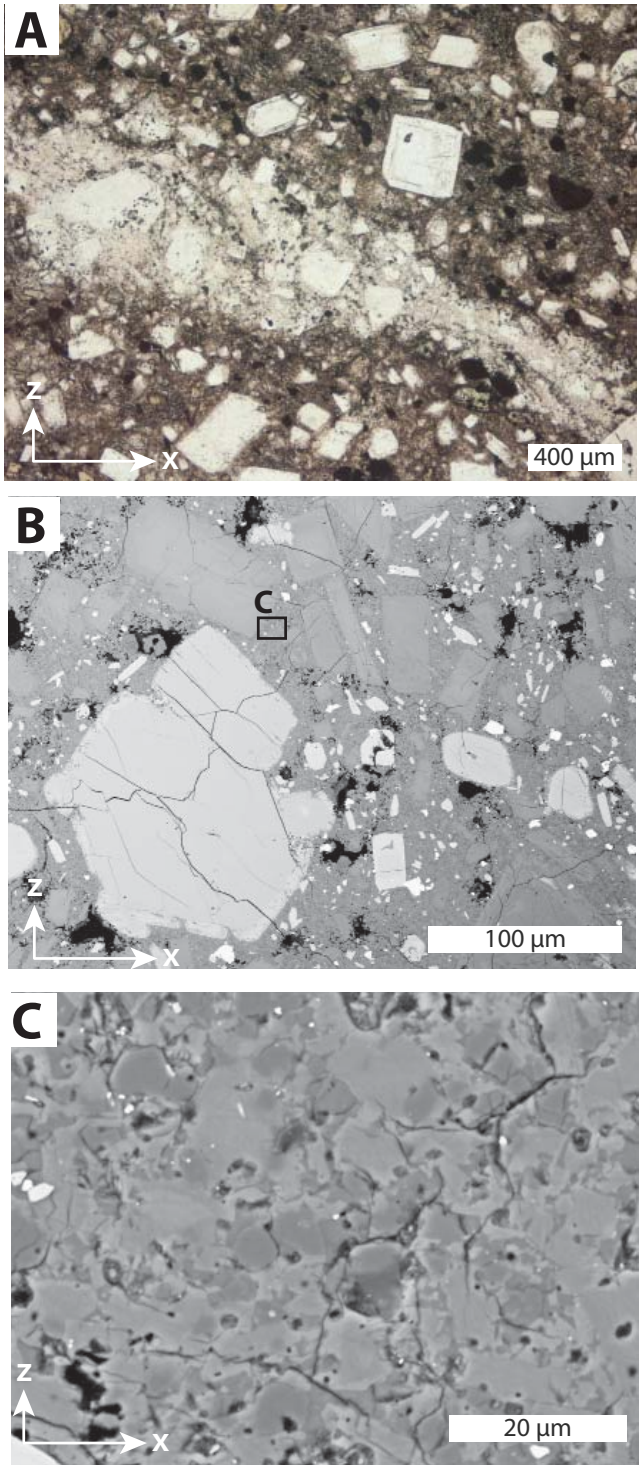

Figure 2.16. Spine 7 Damage Zone Microstructures. Photomicrographs in plane polarized light (A) and SEM backscatter images (B&C) of dacite from Spin 7 exhibiting macroscopic shape fabric. The →X notes extrusion direction and →Z notes towards the exterior of the spine. (A) Photomicrograph of dacite with a shape fabric defined by the alignment of phenocrysts in a micro-groundmass and fractured and ground lineations of broken plagioclase and amphibole. (B) Fractures crosscut phenocryst/groundmass contacts. (C) Location noted in B, groundmass consists of small <10 µm subhedreal to anhedreal microcrysts or (sub-rounded to sub-angular clasts) of plagioclase and quartz.

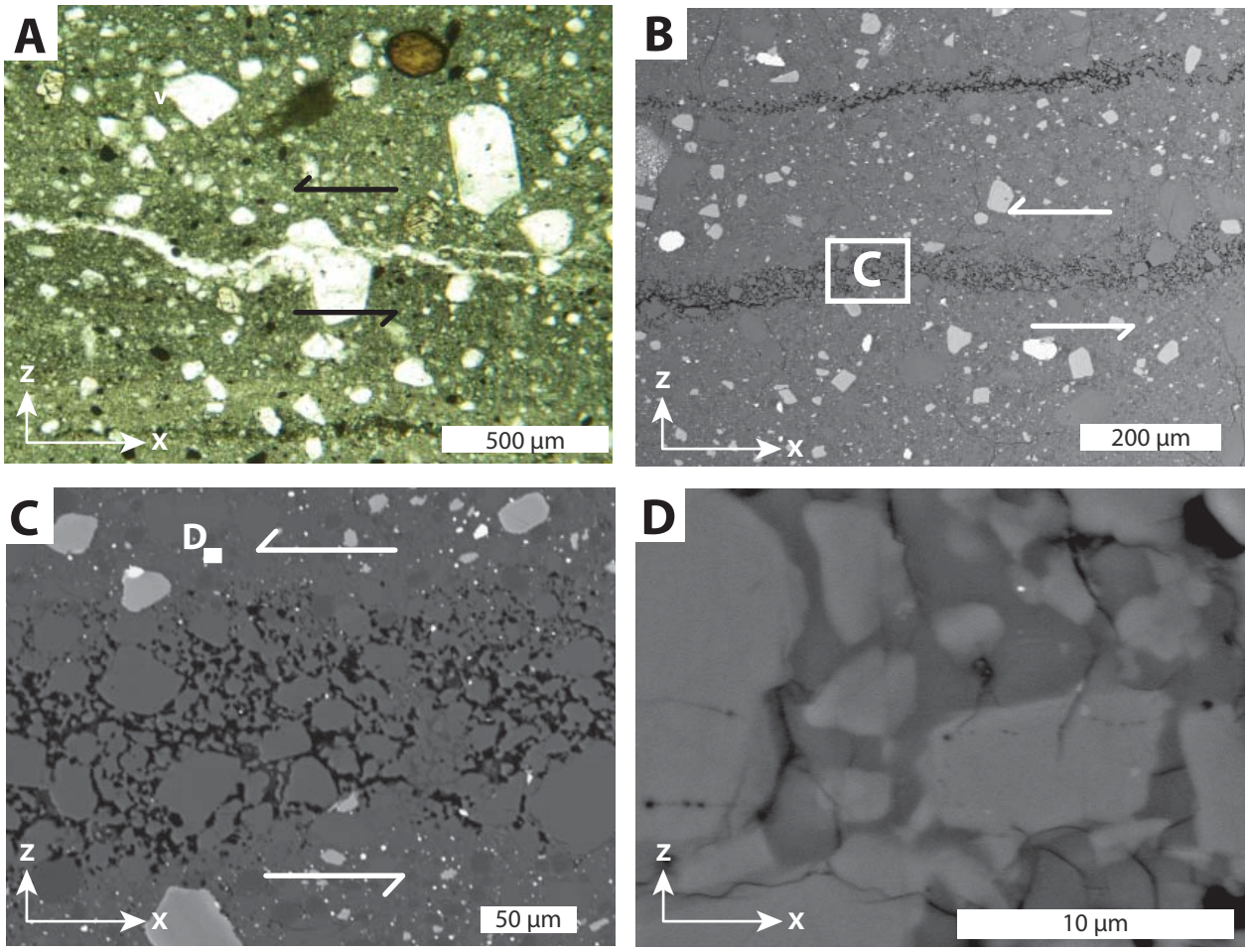

Figure 2.17. Spine 7 Black Cataclasite Microstructures. Photomicrographs in plane polarized light (A) and SEM backscatter images (B,C&D) of specific locations within the black cataclasite unit. Locations are noted in figure 11C. The →X notes extrusion direction and →Z notes towards the exterior of the spine. (A) Photomicrograph of sub-angular to sub-rounded grains of plagioclase, amphibole and orthopyroxene within a ultrafine-grained matrix. Note the white lineation of cataclasite plagioclase that has offset a single subhedral (sub-angular) phenocryst of plagioclase (B) Black cataclasite with two parallel cataclasite lineations where (C) porosity exists between sub-angular, fractured grains of plagioclase and rip-up clasts of black, cataclasite. Location noted by white box in B. (D) Highest magnification of black cataclasite that is matrix supported consisting of sub-angular to sub rounded grains <10 µm with a non-crystalline (or anhedral) matrix that consists primarily of SiO2.

Figure 2.18. Spine 7 Fault Core Microstructures. SEM backscatter images of selected samples from the boundary of the black cataclasite into the gouge/cataclasite and slickensides. The →X notes extrusion direction and →Z notes towards the exterior of the spine. (A) Cross section of slickenside strain localization within indurated gouge. The strain localization is defined by layers of extreme grain-size reduction. Cataclasite consists of fractured phenocrysts, rip-up clasts of black cataclasite below and clasts that are coated with smaller grains. (B) Boundary of black cataclasite and overlying gouge. Pervasive fractures within the black material increase into the gouge where grain size reduction is achieved through grain collision and rotation. (C) Cross section close up slickensides: foliated strain localization defined by layers of extreme grain size reduction and sub-angular grains of fractured phenocrysts in the Y orientation. Location of C is noted by the white box in A. (D) Close up of slickenside surfaces that reveal extreme grain size reduction at the top surface, parallel to Y orientation, where individual grains are hard to distinguish. Slickenside surface is subsequently faulted by R fractures. Specific location is noted by white box in A. (F) Close up of extreme grain size reduction of the upper surface of the slickensides. Individual grains cannot be distinguished.

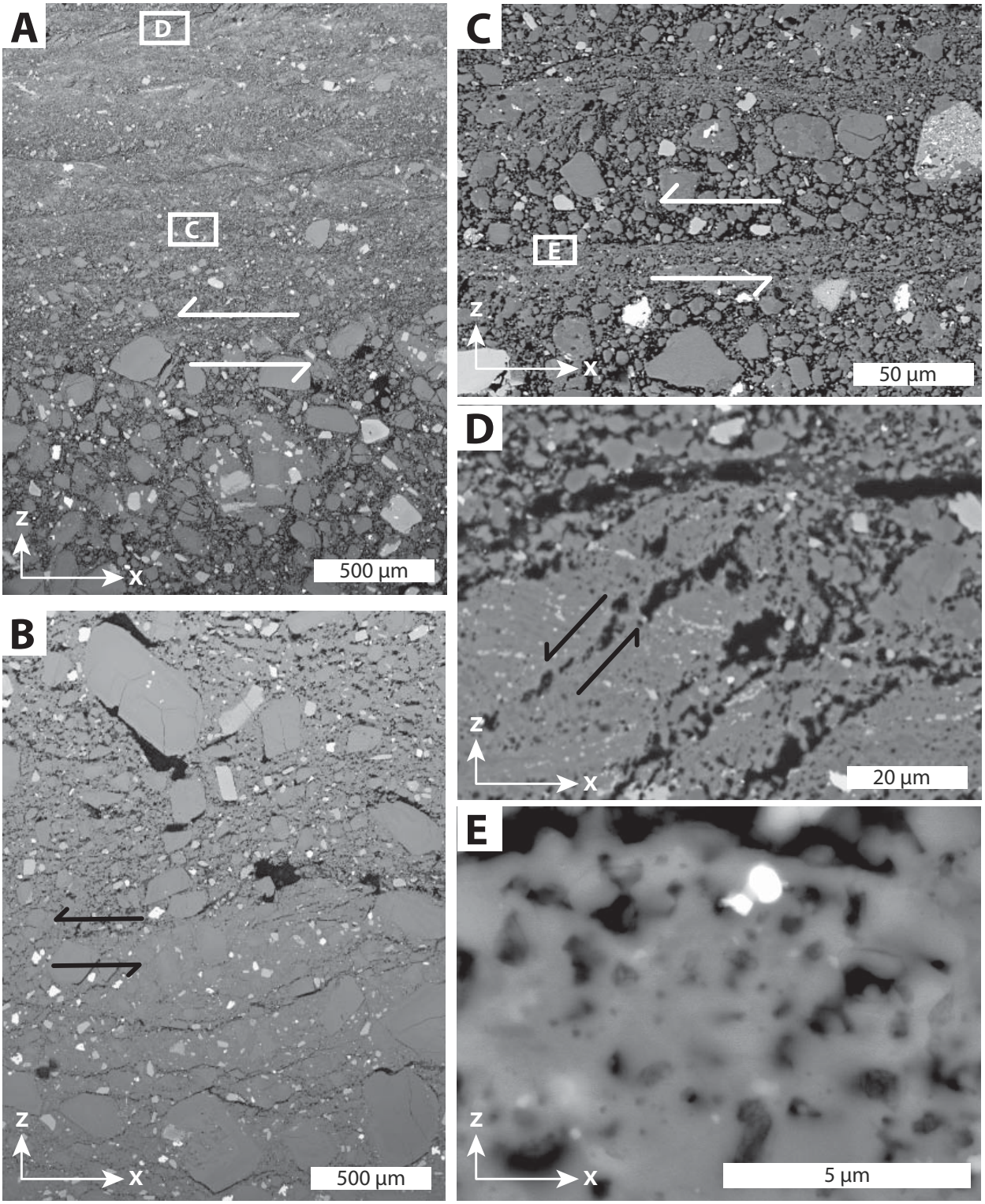
A
D
C
Z
X
500 µm
B
Z
X
500 µm
C
E
Z
X
50 µm
D
Z
X
20 µm
E
Z
X
5 µm

3. Extrinsic conditions attending MSH lava dome growth

3.1 Introduction

Here, surface observations and field data (Chapter 2) are used to produce a model for the origin and evolution of the fault zones that envelope the 2004-2008 Mount St Helens lava dome (i.e. spines). The aim is to recover the extrinsic conditions including, velocity (extrusion rate) and strain rate each spine underwent while ascending to the surface after solidification at ~1 km depth.

The 2004-2008 extrusion of MSH lava domes constitutes as one of the best-monitored lava dome eruptions on record and therefore provides detailed data including surface resolved linear extrusion rate (U), volumetric growth rate (Q) and duration of each sequential spine (Δt) (Sherrod et al., 2008). This data is used to reconstruct the amount of dacite extrusion at the surface. I then reconstruct the pre-2004 eruption magma column in order to model the ascent of the magma from the perspective of the packets of magma that traveled up the same conduit and fed each individual spine. This allows me to explore the relationships between conduit and eruption processes - for example, I can monitor the variations in subsurface ascent rate for each magma packet and compute model values of velocity and associated shear strain rate.

3.2 Surface Observations of Dome Growth from September 2004-June 2008

The MSH 1980-1986 lava dome eruption occurred as discontinuous extrusions of viscous, high-porosity lobes (Fink and Malin, 1990; Swanson and Holcomb, 1990). In contrast, the 2004-2008 eruption was continuous and erupted exclusively solid, low-porosity dacite (Cashman et al., 2008; Pallister et al., 2008b; Vallence et al., 2008). Solidification occurred within the conduit at a depth of ~1 km as a result of degassing-induced

crystallization (Cashman et al., 2008). The 2004-2008 eruption consisted of seven sequential solid spines that now make up a 95 million m^3 lava dome to the south of the 1980-86 dome (CVO-USGS, 2009). The vent was located on the southeast flank of the 1980-86 dome and remained more or less fixed throughout the entire eruption (Scott et al., 2008; Vallence et al., 2008). Each spine emerged over a period of several weeks to several months and eventually disintegrated as a consequence of fracturing and avalanching of rock from its exposed surfaces. By late 2005, the sequence of spines had formed a composite dome with the appearance of multi-crested piles of rubble, and distinguishing individual spines would have been difficult in retrospect without knowledge of their emplacement history (Iverson, 2008; Sherrod et al., 2008). In 2008, the new dome reached 132 m above the 1980 dome and 237 m below the crater rim.

During the eruption, Mount St. Helens was monitored closely by the USGS Cascades Volcano Observatory (CVO), and the Pacific Northwest Seismic Network (PNSN) to document the seismic activity and the day-by-day surface observations to resolve changing growth rates and extrusion directions of the evolving dome growth (Fig. 3.1) (Sherrod et al., 2008). On September 23, 2004, a shallow swarm of hybrid earthquakes of >1.5 M_d (magnitude) began and further increased to M_d =2.5-3.5 in the days following (Moran et al., 2008a). On October 1, 2004, the vent-clearing phase began, marked by five steam and ash explosions puncturing the crater glacier, three of which sent ash >1 km up into the atmosphere and 80 km NNE to Mt Rainer (Scott et al., 2008). The size and frequency of earthquakes decreased after the explosions, but in each case, earthquake activity increased within hours to the pre-explosion levels (Moran et al., 2008b). By October 16, seismic events of M_d <2 were occurring at a rate of ~1 per minute and became so regular they were coined “drum-beats”

(Moran et al., 2008a). While this drumbeat seismicity continued throughout the eruption, there were significant changes in size and variation that correlated the changes in the style of extrusion at the surface (Moran et al., 2008a).

The following extrusion direction is summarized in Figure 3.1. The first dacite spine appeared on October 11, 2004 erupting through the welt at a linear extrusion rate 15-20 m/day towards 235°Az (Major et al., 2008; Schilling et al., 2008; Vallence et al., 2008). This initial rate of eruption continued producing the second spine 'Spine 2' with long axis growth direction of and 180°Az. These spines were disrupted by subsequent eruptions and are now buried. Spine 3 began the main 'whaleback' phase of eruption (11/04/04 to 12/11/04) with an extrusion rate of 8-11 m/day towards 153-162°Az. Breaking off from Spine 3, Spine 4 erupted as the dominate recumbent whaleback spine with a slower rate of extrusion of 4-7 m/day towards 162-140°Az from (12/11/04 to 4/19/05).

On April 19, 2005, Spine 5 thrust over Spine 4, extruding at a slower rate of 2-4.5 m/day from (4/19/05 to 8/10/05). Spine 5 was emplaced as a near-vertical spine towards 155-175°Az The eruption then started to shift to the west of Spine 5, as Spine 6 appeared on August 10, 2005 and extruded at a rate of 3-4 m/day towards 223°Az. Spine 6 quickly crumbled into talus as Spine 7 thrust top of it, and extruded another near-vertical spine on October 24, 2005. Spine 7 started to extrude at a rate of 3-4 m/day and slowed to 2 m/day towards 224-263°Az until March 2007. The extrusion rate steadily decreased to the final waning stage of endogenous dome growth. Activity subsided to no activity in January 2008. On July 10, 2008 it was determined that the eruption that began in 2004 had ended (USGS, CVO 2008).

3.3 A Top-Down Model: Putting Magma Back into the Conduit

The observed extrusion and growth rates are specific to each spine episode and generally decrease over time. However, these extrusion rates do not necessarily represent the subsurface ascent rates of each spine within the conduit. In order to model the velocity of each spine in the subsurface, we begin by reconstructing the dacite column within the conduit during the eruption (Fig. 3.2). This model assumes that the 2004-2008 eruption was essentially continuous, the conduit diameter is 200 meters and all 7 spines extruded from the same vent (Table 3.1) (Scott et al., 2008; Vallence et al., 2008). We assume that a continuous column of magma fed the eruption of the individual spines and track each package of magma (i.e. spine 1-7) individually in the surface. For example when the top of Spine 5 is erupted (i.e. at the surface) the top of Spine 7 magma is ~750 meters the vent (Figure 3.2).

The following calculated parameters are summarized in Table 3.1 and 3.2. The maximum and minimum volume (V) of each spine (x 10^6 m^3) is calculated by:

$$V = Q * (\Delta ts * 24 * 60^2)$$

where Q is the minimum and maximum observed growth rate (m^3/s), Δt_s is the duration of the surface eruption of each spine in days. The minimum and maximum long axis (H) in meters of each spine is independently calculated by:

$$H = U * \Delta ts$$

where U is the minimum and maximum linear extrusion rate of each spine (m/s). The conduit is assumed to cylindrical in shape and the diameter (m) is modeled as:

$$D = 2 * \sqrt{(\frac{V}{\pi * H})}$$

where V is the calculated volume of each spine and H is the calculated length of the long axis of each spine. Therefore the minimum and maximum total height (Ht) of the column of dacite put back into the conduit is then calculated:

$$Ht = \sum_{i}^{7} H_i$$

Because the total volume of 95 x 10^6 m^3 is known, and the average calculated volume ($V_{average}$) is 97 x 10^6 m^3, we use the average height (H) of each spine to model the locations of the top of each spine in the conduit through the duration of the eruption. The pre-eruptive length of the entire dacite column is 2728 m. We assume that the entire column of dacite is continuous, and therefore the bottom of the previous spine is the top of the next spine, i.e. Spine 4 occurs at the top of Spine 5.

We can also use the reconstructed magma column, combined with the observed extrusion rates (U), growth rates (Q), and duration (Δt), and our field observed strain localization to calculate the minimum and maximum shear-strain rates the conduit fault zones accommodated during each spine's ascent. To model the position of each spine within the conduit through time, we assume the solidified dacite within the upper conduit ascends as one unit, and therefore the velocity of upward extrusion within the conduit can be modeled from the surface observed extrusion rate (U), (Fig. 3.3). Figure 3.3B provides the day of the eruption (t) for the position of the top of the spines at three waypoints at 0, 500, and 1000 meters depth in the conduit (t_s / t_{500} / t_{1000}). The velocity from 500-0 m (v_{500}) and the velocity in m/s from 1000-500 m within the conduit (v_{1000}) of the top of each spine is calculated from the basic equation:

$$v = \frac{500}{\Delta t}$$

The model velocities of each package of magma at depth within the conduit are used with the observed fault zone thicknesses to calculate the minimum (homogeneous) shear strain rate the dacite experienced. The calculation is made for: i) fully distributed strain across the diameter of the spine, (γ'h), ii) strain accommodated across the largest observed conduit fault zones (γ'fz), and iii) the maximum shear strain rate where strain is accommodated on a single slickenside surface (γ'ss) within the fault core. Homogeneous strain (γ'h), is calculated by:

$$\gamma' h = \frac{v}{Dav}$$

where $D_{av}$is the average diameter of the dacite column, and v is the calculated v. The shear strain rate the fault zone experienced is calculated by (γ'fz):

$$\gamma' fz = \frac{v}{2 * Tfz}$$

where Tfz is the field measured fault zone for spines 4, 5 and 7. We assume a similar thickens fault zone is mirrored across the spine by doubling the thickness that accommodates the displacement. As described in detail in Chapter 2, there is further strain localization within the fault zone. Therefore the maximum shear strain rate within the fault zone along a single slickenside surface is calculated by:

$$\gamma' ss = \frac{v}{2 * Tss}$$

where Tss is $\geq$ 0.001 m.

3.4 Results of Calculated Velocity Path and Shear Strain Rate

The calculated velocities and shear strain rates are summarized in Tables 3.1 & 3.2. Although the velocity of each spine through the upper conduit decreased over time from $8.7x10^{-5}$ m s^{-1} to $<1.7x10^{-5}$ m s^{-1}, the shear strain rate varies due to the degree of strain

localization observed within the conduit faults (Fig. 3.4). If strain was not localized and accommodated across the diameter of the spine, strain rate would decrease from 10^{-6} s^{-1} to 10^{-7} s^{-1}. However, this is not the case, and strain is localized increasing the shear strain rates achieved at the contact between the spine and the conduit wall. If strain was distributed across width of fault zone, the shear strain rate each fault zone achieved (Spine 4, 5 and 7) is about the same from 1.2-7.9x10^{-5} s^{-1}. Higher strain rates are achieved due to extreme localization within the fault core of each spine up to 10^{-1} s^{-1}.

3.5 Ascent Velocities and Shear Strain Rates

The extrinsic conditions attending this dome growth vary in space and time. Although pressure and temperature increase with depth, they remain consistent throughout the entire eruption. The confining pressure at 1 km depth is 25 MPa decreases to atmospheric pressure, <0.1 MPa at the surface. The temperature of the dacite at crystallization is 857-936-°C (Blundy et al., 2008; Pallister et al., 2008a; Pallister et al., 2008b). This temperature decreases to 400-750°C by the time the dacite is erupted (Moran et al 2008). Because the pressure and temperature gradients remain fixed in space throughout the duration of the eruption, these conditions help explain fault evolution throughout the conduit. They do not, however, elucidate the cause for the diversity in the nature of conduit faults of from Spine 4, Spine 5 and Spine 7. The reconstructed ascent velocity and strain rate of each spine experienced during the ascent path through the same conduit varies and therefore each spine has a unique ascent journey. This changes both in space within the conduit and time through the eruption help elucidate the causes for deformation from dacite to fine-grain fault gouge.

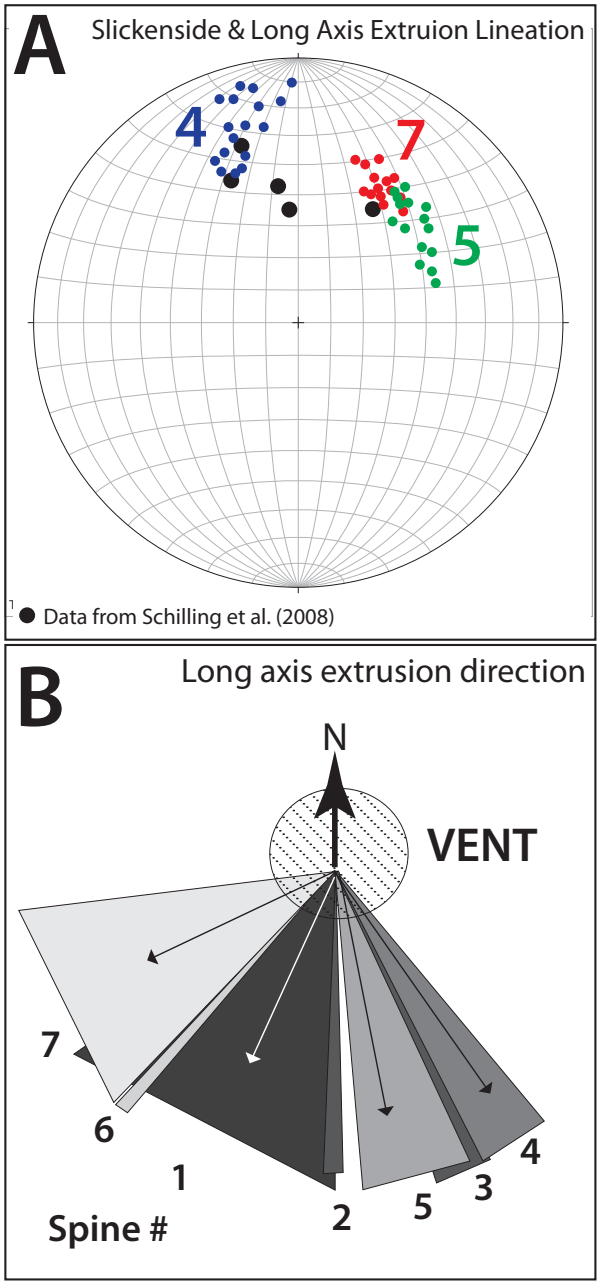

Figure 3.1. Linear elements in MSH Spines. (A) Stereonet representation of long axis of spines during the eruption from Schilling et al. (2008) and slickenside lineations from this study (Appendix A). (B) Rose diagram showing the ranges of linear extrusion directions measured in the horizontal plane (Schilling et al. 2008, Major et al., 2008 LaHusen et al. 2008 and Vallence et al. 2008).

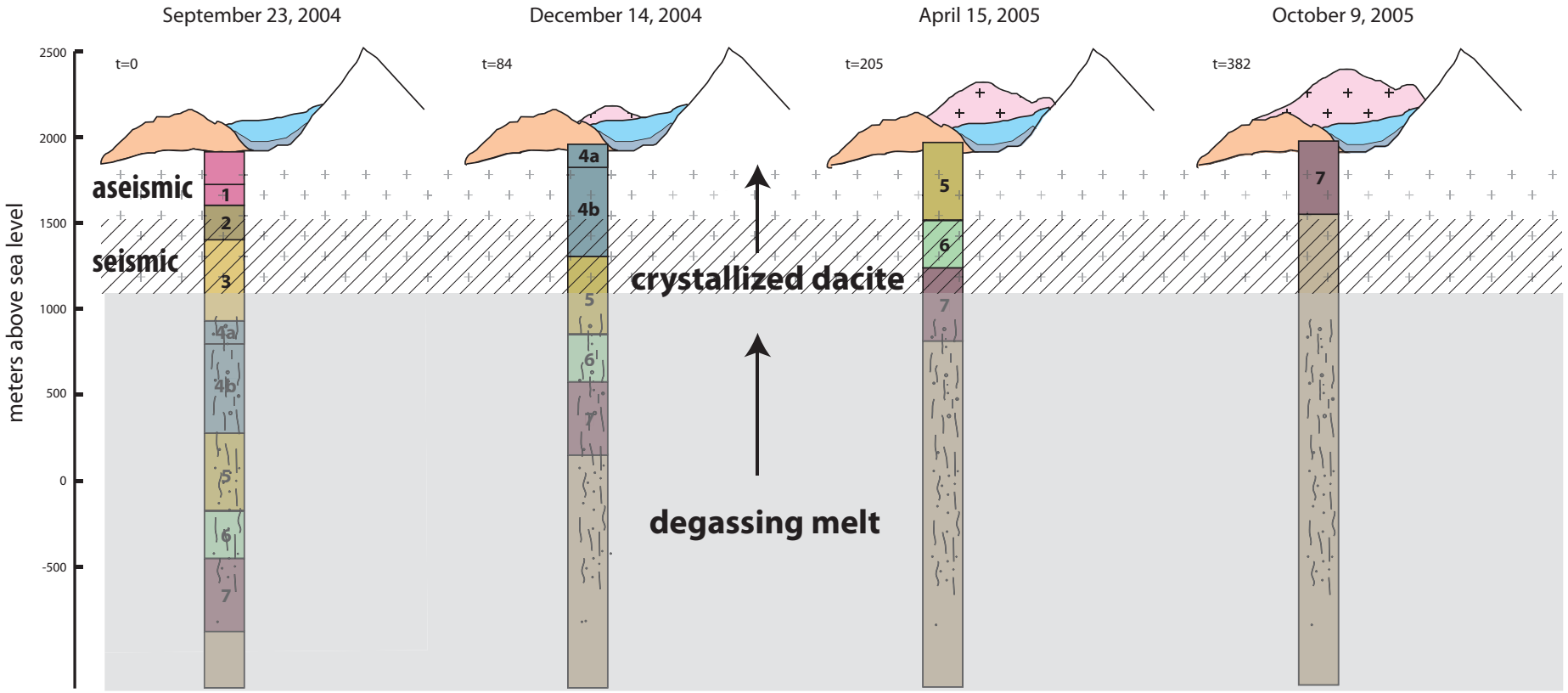

Figure 3.2. Schematic Model For Ascent and Eruption of 2004-2008 MSH Dome. Drawn to scale with no vertical exaggeration showing the time and depth position of the spines at 4 time intervals: (A) t=0 days on September 23, 2004 coinciding with the onset of seismicity. Total height of the column is calculated to be about 2728 meters in length (B) t=84 days on December 14, 2004 when the top of Spine 4 was at the surface, (C) t=205 days, when the top of Spine 5 was at the surface, and (D) t=382 days, when the top of Spine 7 had reached the surface.

Table 3.1. Summary of surface observations of spine growth with day of first appearance at the surface, dates and duration of each episode. The ranges of calculated volumetric growth rate (Q), linear growth rate (μday) were used to model the height and diameter of each spine (see text). The total volume of the 2004-2008 dome was 95 x10^6 m^3 measured in June 2008[e]. Conduit fault thickness (shear zone thickness) is summarized from table 4.

Episode	Day	Dates[a]	Duration at surface [ab]	Extrusive Spine Dimensions[b]	Growth Rate[c]		Extrusion Rate[d]		Calculated Volume			Column Height			Model diameter			Conduit Fault Thickenss
			days		m^3 / s		m / day		x 10^6 m^3			meters			meters			meters
	t		Δt_s	meters	Q_{min}	Q_{max}	U_{min}	U_{max}	V_{min}	V_{max}	V_{avg}	H_{min}	H_{max}	H_{avg}	D_{min}	D_{max}	D_{avg}	T_{fz}
Pre-Seismicity	0	Sept. 23-30, 2004	7	-	-	-	-	-	-	-	-	-	-	-	-	-		-
Vent Clearing	9	Oct. 1-10, 2004	10	470x380	7	12	15	20	6	10	8	150	200	175	227	257	242	-
Spine 1	19	Oct. 11-18,2004	7	150x45	2	3	15	20	1	2	2	105	140	123	121	128	125	-
Spine 2	27	Oct. 19-26,2004	8	240x50	3	3	25	25	2	2	2	200	200	200	115	115	115	-
Spine 3	35	Oct. 27-Dec.14, 2004	49	460x120	4	6	8	11	17	25	21	392	539	466	235	245	240	-
Spine 4a	84	Dec. 14-Jan. 2, 2005	19	340x145	3	5	4	11	4	8	6	76	209	143	262	217	240	3.2
Spine 4b	103	Jan. 3-April 14, 2005	102	490x140	2	3	3	7	13	22	18	265	714	490	252	198	225	3.2
Spine 5	205	April 15-July 23, 2005	101	285x105	1	2	3	6	9	13	11	303	606	455	191	166	179	2
Spine 6	306	July 24-Oct. 8, 2005	76	350x280	2	2	3	4	10	13	11	228	304	266	235	235	235	-
Spine 7	382	Oct. 9, 2005-Aug 2007	275	310x300	1	1	1	2	12	24	18	275	550	413	235	235	235	0.6
Endogeneous	657	Aug. 2007-Jan. 2008	182	-	-	-	-	-	-	-	-	-	-	-	-	-	-	-
Total									74	119	97	1994	3462	2728	208	199	204	

[a] (Herriott et al. 2008)

[b] (Vallence et al. 2008)

[c] (Major et al. 2008, LaHusen et al. 2008)

[d] (Schilling et al. 2008)

[e] (USGS, 2009)

Table 3.2. Summary model of position, velocity and shear strain rate of the top of each spine from September 23,2004 (t=0) at the surface, 500 and 1000 meters below the vent.

Episode	Day			Duration			Velocity			Shear Strain Rate								
	day			days			m/s			Conduit Fault Zone			Slickenside			Homogeneous		
	t_s	t_{500}	t_{1000}	Δt_s	Δt_{500}	Δt_{1000}	$U_{surface}$	U_{500}	U_{1000}	$\gamma'_0 fz$	$\gamma'_{500} fz$	$\gamma'_{1000} fz$	$\gamma'_0 ss$	$\gamma'_{500} ss$	$\gamma'_{1000} ss$	$\gamma'_0 h$	$\gamma'_{500} h$	$\gamma'_{1000} h$
Pre-Seismicity	0	-	-	7	-	-	-	-	-	-	-	-	-	-	-	-	-	-
Vent Clearing	9	-	-	10	-	-	1.7E-04	2.3E-04	2.0E-04	-	-	-	-	-	-	-	-	-
Spine 1	19	-	-	7	19	-	1.7E-04	2.3E-04	2.0E-04	7.2E-05	7.6E-05	NaN	2.9E-01	3.0E-01	NaN	2.9E-06	3.0E-06	-
Spine 2	27	-	0	8	27	-	2.9E-04	2.9E-04	2.9E-04	2.7E-05	5.4E-05	NaN	1.1E-01	2.1E-01	NaN	1.1E-06	2.1E-06	-
Spine 3	35	25	0	49	10	25	9.3E-05	1.3E-04	1.1E-04	2.2E-05	1.4E-04	5.8E-05	8.7E-02	5.8E-01	2.3E-01	8.7E-07	5.8E-06	-
Spine 4a	84	29	5	19	55	24	4.6E-05	1.3E-04	8.7E-05	1.3E-05	2.4E-05	5.6E-05	5.6E-02	1.1E-01	2.4E-01	5.6E-07	1.1E-06	2.4E-06
Spine 4b	103	84	29	102	19	55	3.0E-05	8.1E-05	5.6E-05	1.2E-05	7.1E-05	2.4E-05	5.2E-02	3.0E-01	1.1E-01	5.2E-07	3.0E-06	1.1E-06
Spine 5	205	103	65	101	102	38	3.5E-05	6.9E-05	5.2E-05	1.6E-05	2.3E-05	6.1E-05	4.1E-02	5.7E-02	1.5E-01	4.1E-07	5.7E-07	1.5E-06
Spine 6	306	160	92	76	146	68	3.5E-05	4.6E-05	4.1E-05	4.3E-06	9.9E-06	2.1E-05	1.7E-02	4.0E-02	8.5E-02	1.7E-07	4.0E-07	8.5E-07
Spine 7	382	260	115	275	122	145	1.2E-05	2.3E-05	1.7E-05	2.9E-05	7.9E-05	3.7E-05	1.7E-02	4.7E-02	2.2E-02	1.7E-07	4.7E-07	2.2E-07
Endogeneous	657	502	190	182	155	312	-	-	-	-	-	-	-	-	-	-	-	-

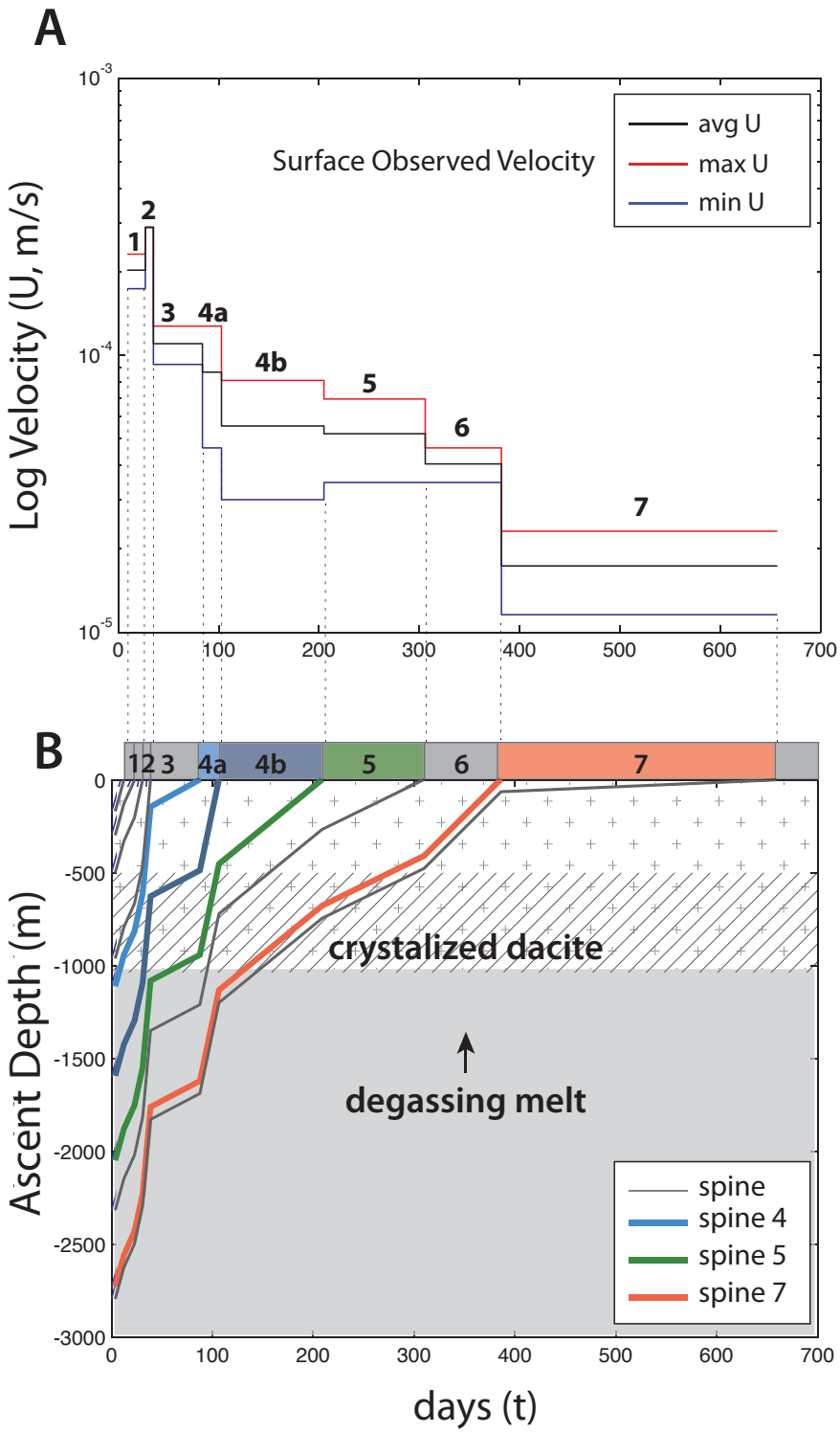

Figure 3.3. Reconstructed Position from Surface Extrusion Rates. Velocity and shear strain rate of ascending column of dacite magma differentiated in terms of individual spines. (A) The linear extrusion rate (U) is plotted as a function of duration in days beginning September 23, 2004. (B) Reconstructed depth of magma that fed each spine plotted against time (days). The field of crosses (+) above 1000 m denotes crystallized dacite resulting from degassing (Cashman et al. 2008; Pallister et al. 2008); crosshatched pattern denotes the estimated source depth of microsiesmicity (Thelen et al. 2008, Moran et al. 2008)

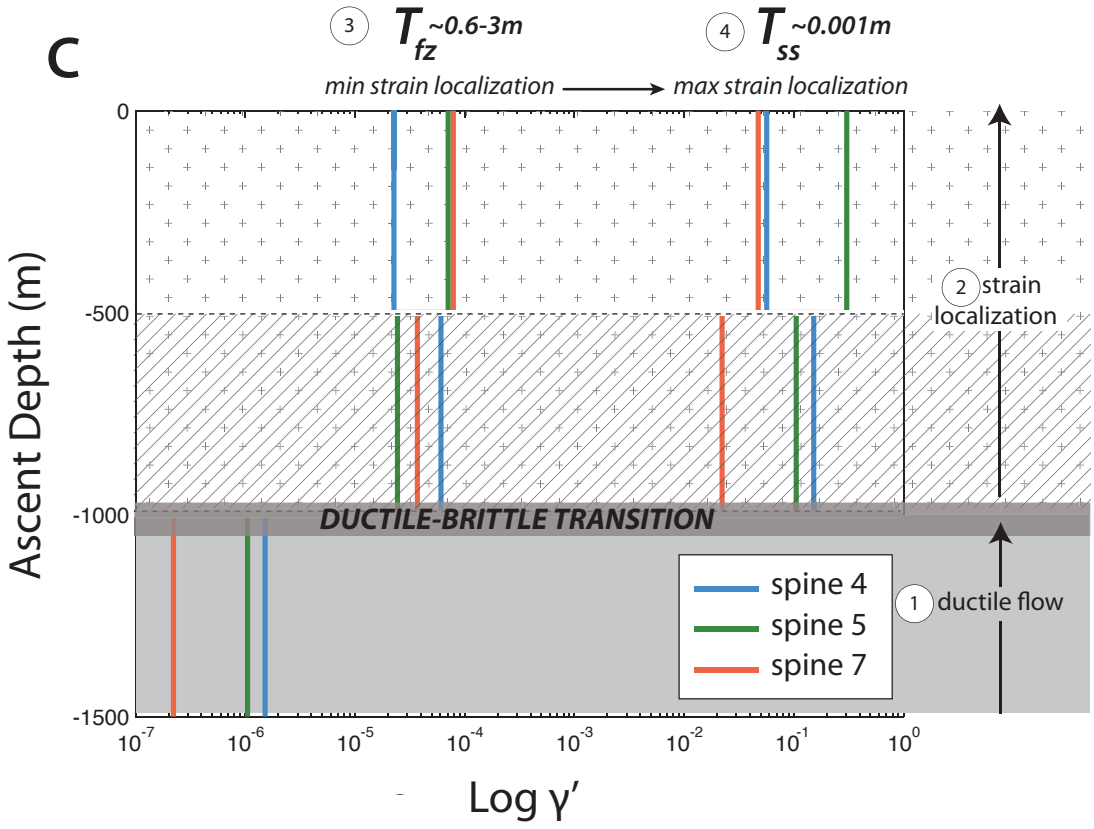

Figure 3.4. Shear Strain Rate of Spines within Conduit. Calculated shear strain rates are plotted as a function of depth for magmas feeding spines 4, 5, and 7. The shear strain rates are based on the observed extrusion velocities and for several model thicknesses of shear zones, including: 1) deformation is accomodated through ductile flow of magma and thickness is diameter of the conduit 200m. This homogeneous strain occurs below the ductile-brittle transition, before final crystallization of the magma 2) deformation is localized after the ductile-brittle transition. 3) The minimum shear strain rate calculated from the modeled maximum thickness of conduit faults where Tfz~0.6-3m. 4) The maximum shear strain rate calculated from the modeled minimum thickness of strain localization within one slickenside surface where Tss~0.001m.

4. Discussion

4.1 Origin and Evolution of the 2004-2008 Mount St. Helens Conduit Faults

The transition from ductile flow of ascending magma to strain localization and brittle failure is due to the change in the intrinsic properties of the magma caused by solidification (Cashman et al. 2008). Prior to crystallization, the magma provides resistance through its viscosity - the ratio of applied stress (rise pressure) to strain rate (rate of flow). A Newtonian viscous magma will flow, with any rise pressure, at a time scale dictated by its viscosity. While brittle behavior can be induced in magma where the rise in pressure builds a rate higher than the relaxation time scale of magma, all fault textures observed in this study resulted from brittle fragmentation of wholly crystalline dacite. The onset of brittle failure is therefore constrained to 1000-500 m depth (the final solidification front of the magma). This inference is supported by the depth and location of the drumbeat earthquakes restricted to depths of 500 m- 1km (Cashman et al 2008, Pallister et al 2008; Major et al. 2008).

The exhumed faults record the cumulative finite strain produced by ascent from ~1 km depth in the conduit. The fault zones that envelope the extruded magma record the accumulated deformation induced by friction and fracture along the conduit wall and the margin of the spine. The following model for the deformational history of MSH dacite magma ascending from a depth of 1 km has been developed (Fig 4.1):

Magmatic flow: Below the rheological boundary, magmatic flow-banding is a result of frictional drag along the conduit wall. This is achieved through magmatic flow resulting in alignment of phenocrysts and broken phenocryst trails.

Onset of brittle failure: Faulting is localized in the dacite against the conduit walls. At this ductile/brittle transition depth, the dacite is solid and will not flow. Rather, low-porosity

dacite is mechanically strong and has the capacity to build shear stresses at the contact with the conduit wall. When the peak failure strength of the fresh dacite at ~25 MPa (confining pressure at 1 km), 100 to 400 MPa, is exceeded, brittle failure occurs and is accompanied by a substantial stress drop (Kennedy et al., 2009; Smith et al., 2011).

Production of gouge and widening of conduit fault: The dacite fails initially at the margin of the dacite due to boundary shear and an increase in the differential stress along the conduit wall. Initial failure of the recently solidified dacite is by a combination of Mode I extensional fractures and by shear fractures. Continued fracturing and movement along these fractures results in the production of gouge. Further ascent generates more damage and faulting within the dacite that generates progressively more gouge. Fracturing is distributed across the marginal dacite rocks, resulting in a widened damage zone and fault core as the spine ascends towards to the surface. Fracturing of dacite produces fine particles along failure surfaces (<2 μm; Kennedy and Russell, 2011). Fracturing also results in zones of breccia that, with further ascent, will roll and abrade and contribute to widen the gouge zone.

Evolution of gouge: Increasing displacement results in a wider gouge zone and a finer grain size in the gouge (as a result of milling, abrasion and microcracking) as discussed in in detail in Chapter 2. The abrupt transition between the damage zone and fault core is evident by the character of the sub-rounded, grain size reduced grains that make up the fault gouge and cataclasite units. Thick layers of cataclasite within the fault core indicate periods of macroscopic ductile movement within the conduit through a combination of microcracking, frictional sliding of fragments past one another, and rotation and transport of grains.

Within the fault core, with increasing shear strain, a mature fault fabric composed of R, P and Y shears is developed. Field observations and experimental studies indicate that Y shears

(shear zone parallel surfaces) are developed with increasing shear strain and are surfaces of strain localization. These Y surfaces are manifested in the MSH shear zones as well developed slickenside surfaces. They are defined by highly polished and striated surfaces with grain sizes < 1 μm and by the presence of amorphous material. We interpret that high strain rate events within the gouge/cataclasite layers (i.e. stress drops and earthquakes) occurred and formed these Y surface, thus they must have accommodated considerable displacement during ascent up the conduit.

The comminution of the gouge particles and production of amorphous material are interpreted to occur as a result of cyclic deformation within the gouge as the fault continues to develop up the conduit. While the production of amorphous material is sometimes related to fast slip events, the presence of amorphous material does not necessarily correspond to the sliding velocity, but rather can be the result of localized shear strain (high shear strain rates) and also large amounts of shear strain (Yund et al. 1990). Both scenarios are likely within the Mount St. Helens conduit faults where the high shear strain rates have potential to generate extreme localization (below 500 meters) and accommodates meters of displacement. The slickensides within the gouge of Spines 4, 5, 7 are similar in character, while Spine 7 is the only spine with an ultrafine-grained black cataclasite.

The upper 500 meters of the conduit is dominated by aseismic rolling of fault gouge. Aseismic creep is common in most shallow continental faults (<500 meters from the surface) where confining pressure is too low to localize strain and produce co-seismic stress drops and slip. In Spine 4 and 5, the gouge is made up of fractured and sub-rounded clasts of dacite with trace amounts of wall rock. The unconsolidated gouge of Spine 7, contains clasts of fractured

dacite, and clasts of black to grey cataclasite. This cross cutting relationship dictates that the black cataclasites formed before aseismic rolling and 'creep' from 500-0 meters.

The damage zone continues to grow and deform where strain oscillates from localization within the fault core to the dacite whereby Riedel further kink. Strain can be accommodated within the damage zone as evidence from Spine 4 along zones of dense fracturing or in Spine 5 where a secondary fault core can form.

Surface expression of spines: The spines emerged from the conduit bound by andesite and basalt products of the Castle Creek period into fractured 1980-86 dome rock and crater-floor debris at about 100-200 m below the vent. The surface eruption and subsequent bending and settling in each spine were accommodated by listric normal faults that are observed on meter to centimeter scales.

The fault evolution up the conduit is complex where strain is accommodated initially through fracturing of the dacite and initial production of the gouge. Continued ascent causes widening of the damage zone, which in turn, contributes new brecciated and fractured dacite to widening the fault core. The fault core evolves with further rounding and grain size reduction, fabric development and extreme strain localization. While this model presented is a summary of fault evolution up the conduit from the origin at 1 km depth, the variety in textures and widths of Spines 4, 5 and 7 conduit fault zones is further discussed when considering the modeled ascent velocities and shear strain rates.

4.2 Geometric Variability of the Shear Zones in Spines 4, 5 and 7.

The conduit fault zones that encase each spine narrow and exhibit less macroscopic brittle fractures within the damage zone from Spine 4 to 7. The magma extrusion rate (U) decreased with time during the MSH eruption, and therefore, each successive spine has a

decrease in rate of magma supply, at the ductile/brittle transition (i.e. 1 km depth, the depth of magma solidification). At the onset of brittle failure, each packet of magma has similar intrinsic rock properties; for example, mineralogy, chemistry (Appendix D) and porosity (Kennedy et al. 2009; Smith et al 2011). All extrinsic properties are also essentially the same at this boundary: confining pressure ~25 MPa and temperature 734-800°c (Pallister et al. 2008). The main difference is the rate of supply of fresh dacite that is expressed by the reconstructed ascent velocity at specific waypoints up the conduit (Table 3.2). At 1 km depth the reconstructed ascent velocities for spines 4, 5 and 7 are 5.6-8.7 $x10^{-5}$ m/s, 5.2-5.6 $x10^{-5}$ m/s, $\leq$1.7 $x10^{-5}$ m/s, respectively.

At higher ascents rates, a thick gouge and damage zone develops (Spine 4 and 5), resulting in a wide shear zone at 1 km –to 500m depth. As lower ascent rates (e.g. Spine 7) there a lower driving force from beneath and hence there is less intense fracturing at 1km depth and the shear zone is relatively thin at 1 km- 500 m depth. Therefore the initial frequency of fracture and fault production is lower, allowing the Spine 7 fault zone to start narrower than those in Spine 4 and 5.

Although the ascent rate is decreasing with time, narrowing of shear zones counteracts this where the shear strain rates across the fault zone are similar in each spine despite the decrease in magma supply rate (Fig. 4.2). Spine 7 achieved similar minimum shear strain rates as Spines 4 and 5 across the entire fault zone, however, the maximum shear strain rate was less than in Spine 4 and 5 (Fig. 4.2, Table 4.1). Figure 4.2 displays the range of potential shear strain rates within the conduit faults. The reconstructed ascent velocity binds the regions on Figure 4.2 from 1000-500 meters (seismic) and 500 m to the surface (aseismic zone) and the observed maximum and minimum thickness of strain localization (i.e. the thickness of the

slip zone in which displacement was accommodated Tfz or Tss). Spine 7 has a narrower shear zone than Spines 4 and 5 and therefore, the minimum shear strain rate, if accommodated across the conduit fault zone, is similar to Spines 4 and 5, despite the decrease in magma supply rate. In fact, the potential for strain further strain localization can result in similar shear strain rates within the seismic and aseismic parts of the conduit (Fig. 4.2).

Moreover, if strain is localized within a fine-grain slickensided surface or the narrowest zone of ultrafine-grained black aphanitic zones, where Tss = 0.001m, Spines 4 and 5 experienced shear strain rates, on average, 6 to 7 times higher than shear strain rates within Spine 7. The shear strain rate within Spine 4 was 2.4 $x10^{-1}$ s^{-1}, and Spine 7 can experience a maximum shear strain rate of $2.2x10^{-2}s^{-1}$ (Table 4.1). Therefore the finest grained zones with amorphous material in Spine 7 formed under lower shear strain rates than the slickensides in Spines 4 and 5.

Table 4.1. Summary Shear Strain Rate. See text for calculations.

	Shear Strain Rate – FZ	**Shear Strain Rate – SS**
Spine 4	$1.3\ x10^{-5}$ - $5.6\ x10^{-5}$	$5.6\ x10^{-2}$ - $2.4x10^{-1}$
Spine 5	$1.6\ x10^{-5}$ - $6.1\ x10^{-5}$	$4.1\ x10^{-2}$ - $1.5x10^{-1}$
Spine 7	$2.9\ x10^{-5}$ - $7.9\ x10^{-5}$	$1.7\ x10^{-2}$ - $2.2x10^{-2}$

The amount of time each packet of dacite spent traveling up through the earthquake zone (1000-500 m) and aseismic zone (500-0 m), increased throughout the eruption due to the lower ascent velocity. Spine 7 took up to 6 times longer to ascend through the 1000-500 m depth in the conduit, and three times longer to ascend through the 500-0 m upper conduit (Table 4.2). The fragmented, grain size-reduced fault rocks dwelled at ambient conduit temperatures of 700-800°C for longer time intervals in Spine 7 than previous spines. The

ultrafine-grained zones of Spine 7 had more time to sit at ambient temperatures, which may contribute to the difference in black cataclasite texture resulting in a more indurated competent cataclasite rock that exhibits macroscopic ductility. That is, after the formation of fine-grained gouge, the material has time to 'weld'. This is supported by whole clasts of sub-rounded black cataclasite within the gouge where it was further broken to form the gouge.

Table 4.2. Summary Residence Time. See text for details.

	1000-500 meters	**500-Surface**
Spine 4	*24 days*	*55 days*
Spine 5	*38 days*	*102 days*
Spine 7	*145 days*	*122 days*

To summarize, in continental faults and experimental observations it is widely accepted that a higher rate of deformation rates result in more localization of strain. At Mount St Helens, the opposite is true, higher rates of displacement result in more diffuse damage (Spine 4 and 5), and lower rates of displacement result in shear localization (Spine 7). After the initial narrower onset, a damage zone does not develop in Spine 7 due to the steady decrease in ascent velocity. This decrease continues to result in intense localization of strain within very narrow ultrafine-grained cataclasite zones. The resulting high shear strain rates along the narrow zone, formed ultrafine-grained cataclasites that accommodated 'ductile' cataclastic flow and also lubricated the solid spine up the conduit. The lubricating nature of the ductile cataclasite facilitated further shear strain localization in the fine-grained cataclasite and in the development of a foliation. These cataclasites had a relatively long dwell time under high temperatures (Table 4.2). The dwell time resulted in welding the fine cataclasites

into black aphanitic material, which is subsequently incorporated as clasts into the overlying, younger gouge.

Factors that contribute to the differences in shear zone character at each dome are: 1) differences in ascent rates at the origin of brittle failure, 2) variations in shear strain rates ranging from relatively slow if displacement was accommodated across entire fault zone to relatively fast if displacement was accommodated along thin slickensided surfaces, 3) and the residence time that the fault rocks experienced at high temperatures within the conduits with dwell time increasing with decreasing magma supply rate.

4.3 Seismic Insights to Mount St. Helens Conduit Faults

Volcanic conduit fault zones and the mechanisms responsible for their formation are of interest because of the implications for earthquake energy release (Wilson et al., 2005). At MSH, earthquakes are located 1000-500 meters below the vent (Moran et al. 2008). As discussed above, the structures and fault rocks observed within the conduit faults in MSH reveal distributed strain within the fault core and strain localization along slickensided surfaces. The existence of these structures that records both localized slip and distributed flow within continental faults indicate repetitive deformation sequences characteristic of seismic cycling (Chester and Chester, 1998; Hobbs et al., 1986; Power and Tullis, 1989). At Mount St. Helens changes in drumbeat character were unrelated to variations in magma flux at the conduit; thus, drumbeat size and spacing are more likely a function of extrusion mechanics than of extrusion rate (Moran et al 2008).

There are two proposed sources for seismicity at Mount Saint Helens: Kennedy and Russell (2011) argue that stress drops are generated 1) by the formation of shear fractures in fresh dacite can generate drumbeat seismicity and 2) by stick slip behavior within 1 mm thick,

slickensided planes (Fig. 4.3) where fast shear strain rates can produce co-seismic slip. The 2004-2008 Mount St Helens dome growth produced 'multiplets' known as families of earthquakes that are similar and persistent in their waveform that they must have originated from the same, stationary source over a long period of time (Moran et al 2008). This stationary source is at the solidification boundary and is the result of initial production of shear fractures at the spine conduit boundary (Kennedy and Russell 2011). Iverson et al. (2008) proposed a stick slip model for this mechanism where two parameters have to be met: the gouge has to have rate-weakening behavior and the driving for (magma) has to be more pliable than the dacite and the gouge.

Field evidence from this study supports both mechanisms as sources of seismicity: 1) abundant shear fracturing at the onset of deformation, and 2) numerous parallel layers of ultrafine-grained well-indurated slickensides. All spines failed at the ductile/brittle boundary, therefore released some seismic energy. Seismicity was also sourced along thin, discrete surfaces.

The relationship between displacement rate (velocity), shear-strain rate and fault zone width in continental shear zones and Mount Saint Helen's shear zones is plotted in figure 4.3A. MSH shear zone ascent velocity is three magnitudes smaller than dike-fed magma ascent rates, but eight magnitudes larger than aseismic creep along deep, wide continental shear zones. Shear strain localization within the conduits, results in fast shear strain rates that are comparable to co-seismic slip events that occur on discrete thin, fault surfaces (Fig. 4.2B). Slickenside planes within Spine 4 and 5 achieved the fastest shear strain rates capable of coseismic slip. Spine 7 slickensides also achieved high shear strain rates, however, not capable of coseismic slip. Rather, after initial failure and stress drop of fresh, solid dacite,

aseismic cataclasitic flow, and extreme localization and displacement within the gouge dominated the waning of the 2004-2008 Mount St. Helens lava dome eruption.

Figure 4.1 Space/time Model of Conduit Fault Origin and Evolution. (A) Schematic cross section of the MSH 2004-2008 dike/conduit. The 1980 conduit/dike is shown in grey that extends to the bottom of the 1980 dome deposit in the crater. The top of the magma chamber and the source for the 2004-2008 eruption is located ~5km below the vent (Pallister et al. 2008; Clynne et al. 2008; Rutherford and Devine, 2008, Blundy et al 2008). (a) The dacite ascends through an initial dike/conduit ~60 meters in diameter at 4 km depth then opens to ~120 meters wide at 2 km depth (Thornber et al, 2008; Streck et al 2008). The conduit opens to ~200 meters at about 1 km depth (Iverson 2008, Pallister et al 2008). At <1 km depth, the dacite is fully crystallized (Cashman et al 2008, Pallister et al 2008). The sources for the earthquakes are noted by the dashed zone (Moran et al. 2008; Thelen et al. 2008). The blue box indicates the position of B. (B) Not drawn to scale. Schematic cross section in the kinematic plane (X/Z) showing the evolution of deformation events from magmatic flow, to brittle failure and fault production that lubricates the solid dacite spine to the surface. Sequence of events follows: 1. degassing magma with magmatic flow banding, and shape fabric from the (friction/drag/interaction) with the conduit wall 2. The onset of brittle failure at the final solidification front, and deepest location of earthquake sources. 3. The production of gouge by further breakdown of fractured dacite and entrainment of wall rock. 4. The dynamic interplay between the following deformation types: evolution of gouge by cataclasitic flow and further grain size reduction and rounding, localized slip within the cataclasite/gouge along y-surfaces creating ultrafine-slickensided surfaces, further fracturing of dacite, folding r-shears, localizing creating breccia, fracturing within gouge and cataclasite along Y and R surfaces as gouge/cataclasite behaves as a competent material.

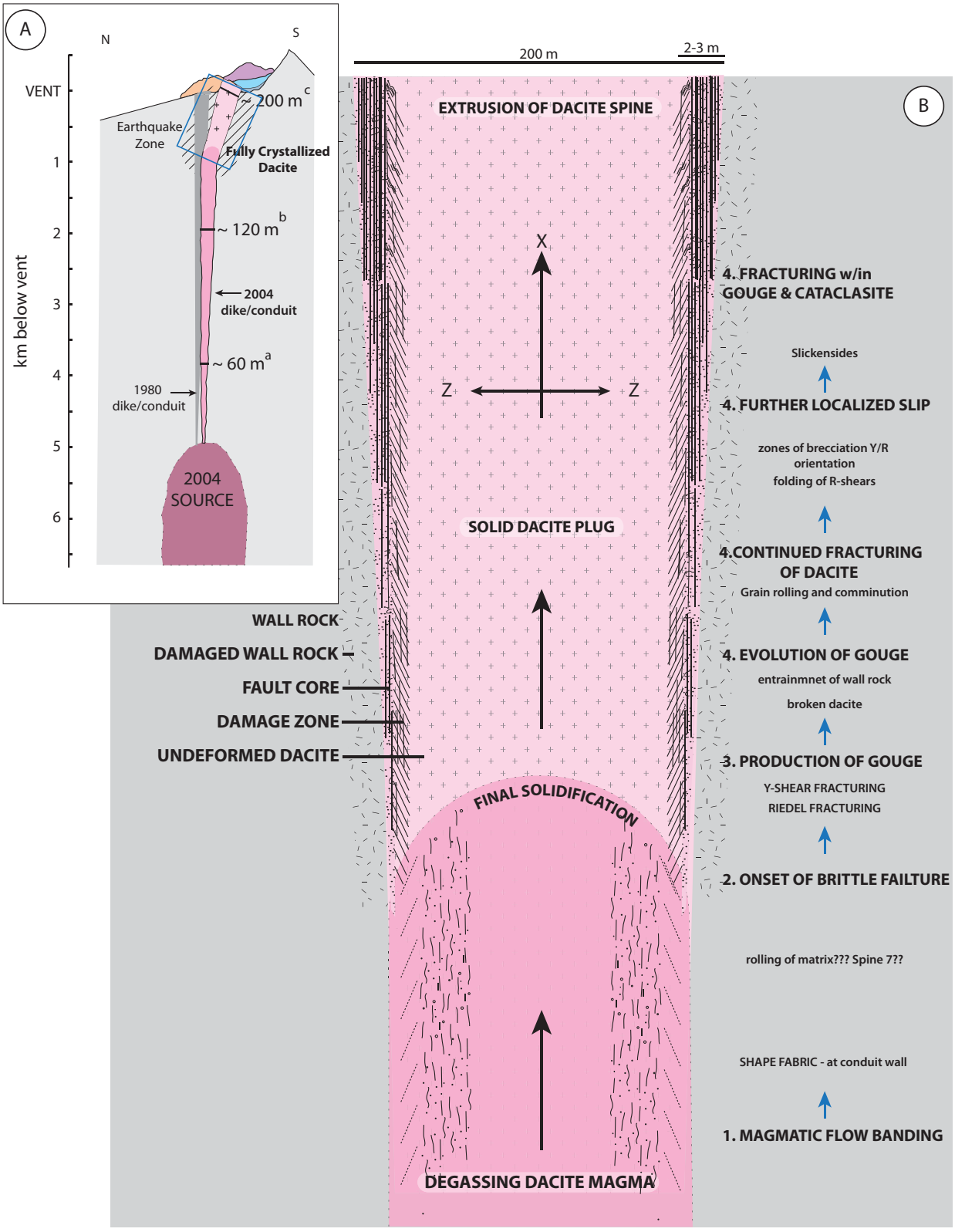
A
N
S
VENT
km below vent
1
2
3
4
5
6
~ 200 m c
Earthquake Zone
Fully Crystallized Dacite
~ 120 m b
2004 dike/conduit
~ 60 m a
1980 dike/conduit
2004 SOURCE
200 m
2-3 m
B
EXTRUSION OF DACITE SPINE
X
Z
Z
SOLID DACITE PLUG
WALL ROCK
DAMAGED WALL ROCK
FAULT CORE
DAMAGE ZONE
UNDEFORMED DACITE
FINAL SOLIDIFICATION
DEGASSING DACITE MAGMA
4. FRACTURING w/in GOUGE & CATACLASITE
Slickensides
4. FURTHER LOCALIZED SLIP
zones of brecciation Y/R orientation
folding of R-shears
4.CONTINUED FRACTURING OF DACITE
Grain rolling and comminution
4. EVOLUTION OF GOUGE
entrainmnet of wall rock
broken dacite
3. PRODUCTION OF GOUGE
Y-SHEAR FRACTURING
RIEDEL FRACTURING
2. ONSET OF BRITTLE FAILTURE
rolling of matrix??? Spine 7??
SHAPE FABRIC - at conduit wall
1. MAGMATIC FLOW BANDING

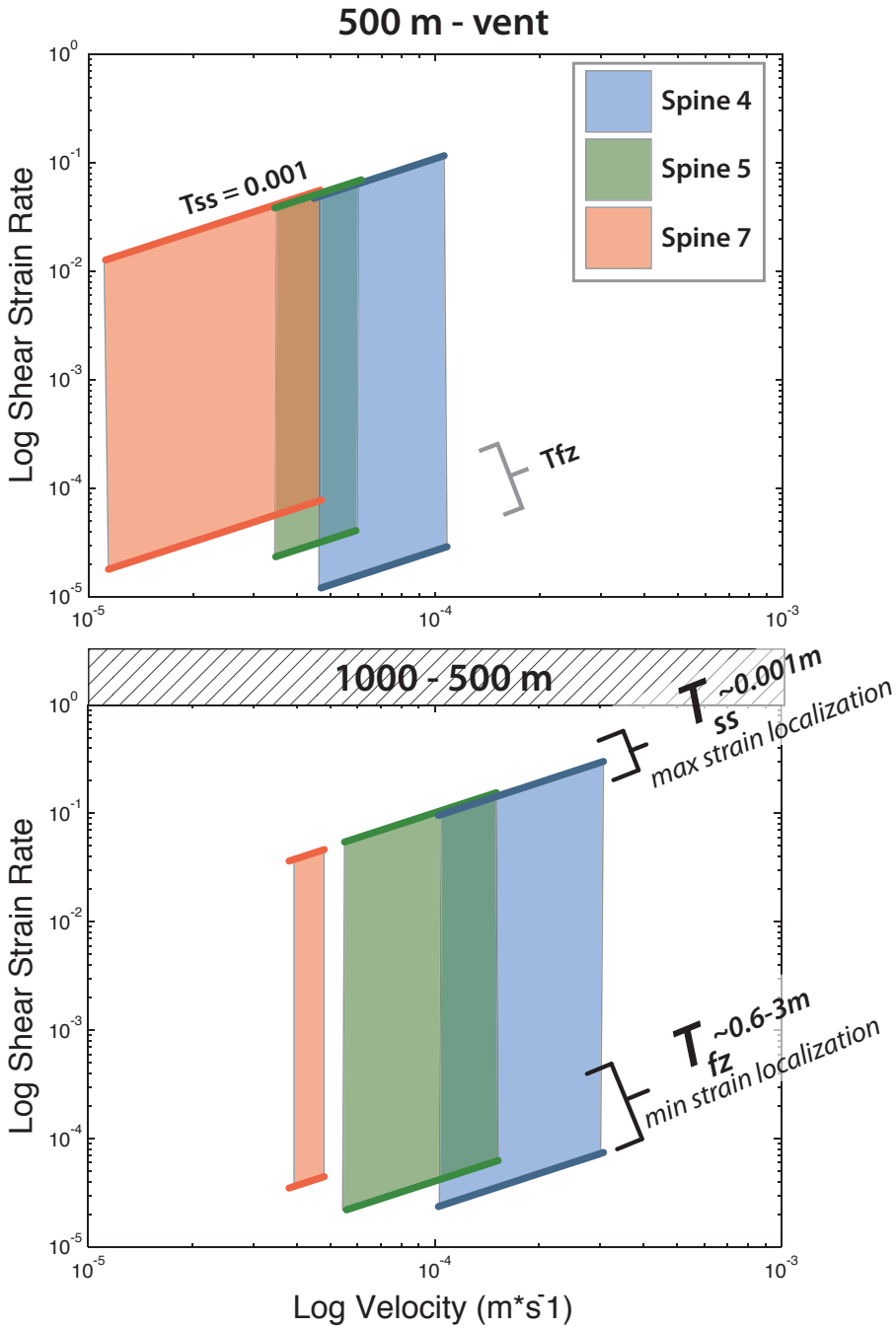

Figure 4.2 Log Shear Strain Rate vs. Log Interval Velocity. Ranges of shear strain rate experienced during ascent within each spine from two depth intervals: 1000-500 meters and 500 to the surface. The interval velocity is a reconstructed ascent rate (Fig. 3.3, Table 3.2) for the specific ascent depth intervals. The shear strain rate is dependent upon the reconstructed ascent velocity and the model Tfz (fault zone maximum thickness) or Tss (minimum thickness if strain accommodated along a single plane of slickensides).

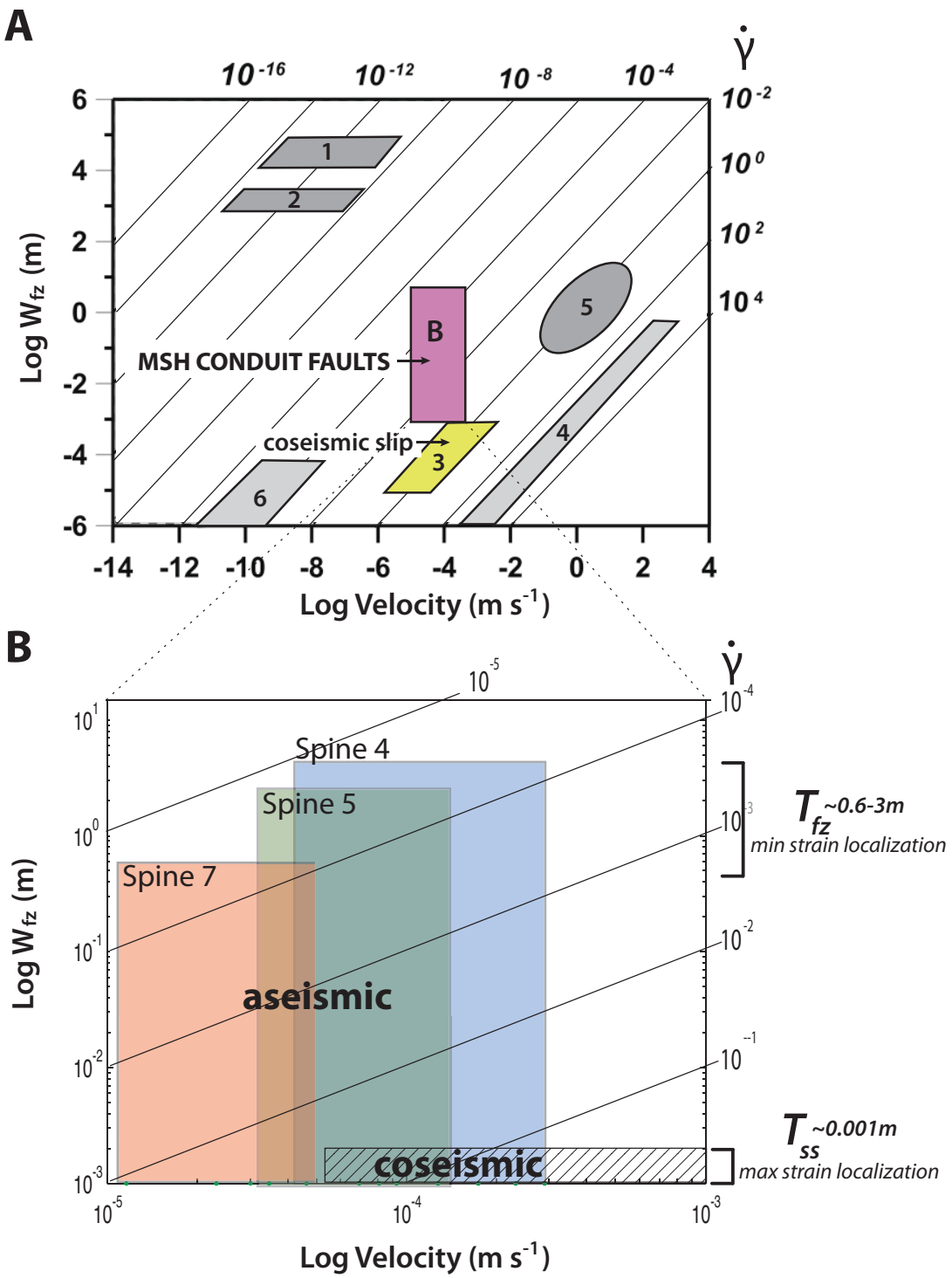

Figure 4.3. Application to Other Shear Zones. (A) Modified from Kennedy et al. (2002), relationships among velocity, shear-strain rate and fault zone (shear zone) width (Tfz). Range of strain rates (γ) possible within the Mount St. Helens 2004-2008 conduit faults. Also shown are characteristic field for (grey shaded areas):1=foliated lower crustal terrenes, 2=kilometer-scale crustal high-strain zones, 3=coseismic slip of discrete fault surfaces driven by large earthquake events, 4=crack propagation, 5=dike-fed magma ascent processes and 6=high-temperature experimental rock deformation. (B) Range of strain rates possible within each spine. where spine 4 and 5 slickenside thicknesses approach coseismic slip, where spine 7 ascent rate (velocity) is not large enough to generate coseismic slip.

5. Conclusions

In conclusion, the contents of this thesis do the following:

1. Document the nature strain distribution and accommodation within three dacite spines from center of the spines to the margin to describe the variable nature of these conduit faults that bound the solid dacite spines in the MSH eruption.
2. Demonstrate that strain is a result of shearing along the conduit wall during ascent from 1 km to the surface and is localized along narrowing fault zones as throughout the eruption. While the mechanisms of deformation reveal exclusively brittle processes at the microscopic scale, there is a scale dependent ductility by catalases.
3. Present a model derived from surface observations of the eruption and from field data to show each package of magma that ascended through the same conduit suffered decreasing ascent velocities and variable shear strain along various planes within the conduit fault.
4. Discuss the origin and evolution for these conduit faults both up the conduit and throughout time to understanding the transport of solid dacite to the surface along and the role of ascent velocity and shear strain rate in controlling the nature of the conduit faults.

References

Blundy, J., Cashman, K.V. and Berlo, K., 2008. Evolving magma storage conditions beneath Mount st. Helens inferred from chemical variations in melt inclusions from the 1980-1986 and current (2004-2006) eruptions. Sherrod, D.R., Scott, W.E., and Stauffer, P.H., eds., 2008, A volcano rekindled; the renewed eruption of Mount St. Helens, 2004-2006: U.S. Geological Survey Professional Paper 1750: 755-790.

Carn, S.A., Watts, R.B., Thompson, G. and Norton, G.E., 2004. Anatomy of a lava dome collapse: the 20 March 2000 event at SoufriËre Hills Volcano, Montserrat. Journal of Volcanology and Geothermal Research, 131(3-4): 241-264.

Cashman, K.V., Thornber, C.R. and Pallister, J.S., 2008. From dome to dust: shallow crystallization and fragmentation of conduit magma during the 2004-2008 dome extrusion of Mount St Helens, Washington. Sherrod, D.R., Scott, W.E., and Stauffer, P.H., eds., 2008, A volcano rekindled; the renewed eruption of Mount St. Helens, 2004-2006: U.S. Geological Survey Professional Paper 1750: 387-415.

Chester, F.M. and Chester, J.S., 1998. Ultracataclasite structure and frictional processes of the PUnchbowl fault, San Andreas system, California. Tectonophysics 295: 199-221.

Chester, F.M., Evans, J.P. and Beigel, R.L., 1993. Internal structure and weakening mechanics of the San Andreas Fault. Journal of Geophysical Research, 98: 771-786.

Clynne, M.A., Calvert, A.T., Wolfe, E.W., Evarts, R.J. and Lanphere, M.A., 2008. The Pleistocene eruptive history of Mount St. Helens, Washington, from 300,000 to 12,800 years before present. A VolcanoRekindled: the Renewed Eruption of Mount St. Helens, 2004-2006: USGS Professional Paper 1750: 593-628.

Faulkner, D.R., Jackson, C.A.L., Lunn, R.J., Schlische, R.W., Shipton, Z.K., Wibberley, C.A.J. and Withjack, M.O., 2010. A review of recent developments concerning the structure, mechanics and fluid flow properties of fault zones. Journal of Structural Geology, 32(11): 1557-1575.

Fink, J.H. and Anderson, S.W., 2000. Lava Domes and Coulees. Sigurdsson, H. (ed) Encyclopedia of Volcanoes: 307-318.

Fink, J.H. and Griffiths, R.W., 1998. Morphology, eruption rates, and rheology of lava domes: Insights from Labratory models. Journal of Geophysical Research, 103(B1): 527-545.

Fink, J.H. and Malin, M.C., 1990. Intrusive and extrusive growth of the Mount St Helens lava dome. Nature, 348(29 November 1990): 435-437.

Hobbs, B.E., Ord, A. and Teyssier, C., 1986. Earthquakes in the ductile regime? Pure Application of Geophysics, 124(309-336).

Iverson, R.M., 2008. Dynamics of seismogenic volcanic extrusion resisted by a solid surface plug, Mount St. Helens, 2004-2005. A VolcanoRekindled: the Renewed Eruption of Mount St. Helens, 2004-2006: USGS Professional Paper 1750: 461-494.

Iverson, R.M., Dzurisin, D., Gardner, C.A., Gerlach, T.M., LaHusen, R.G., Lisowiski, M., Major, J.J., Malone, S.D., Messerich, J.A., Moran, S.C., Pallister, J.S., Qamar, A.I., Schilling, S.P. and Vallence, J.W., 2006. Dynamics of seismogenic volcanic extrusion at Mount St Helens in 2004-05. Nature, 444(23 November 2006): 439-443.

Jaggar, T.A., 1904. The initial stages of the spine on Pelée American Journal of Science, 17: 34-40.

Kaneko, T., Wooster, M.J. and Nakada, S., 2002. Exogenous and endogenous growth of the Unzen lava dome examined by satellite infrared image analysis. Journal of Volcanology and Geothermal Research, 116(1-2): 151-160.

Kennedy, L.A. and Russell, J.K., 2011. Cataclastic production of volcanic ash at Mount Saint Helens. Physics and Chemistry of the Earth, Parts A/B/C(0).

Kennedy, L.A., Russell, J.K. and Edward, N., 2009. Origins of Mount St. Helens cataclasites: Experimental insights. American Mineralogist, 94: 995-1004.

Lacroix, A., 1904. La Montagne Pelée et ses éruptions. Paris, Masson et Cie: 662p.

Logan, J.M., Dengo, C.A., DHiggs, N.G. and Wang, Z.Z., 1992. Fabrics of experimental fault zones:Their development and relationship to mechanical behavior. Fault Mechanics and Transport Properties of Rocks, International Geophysics Series, 127: 33-67.

Major, J.J., G., K.C., P., P.M. and G., L.R., 2008. Extrusion rate of the Mount St Helens lava dome estimated from terrestrail imagery November 2004-December 2005. A VolcanoRekindled: the Renewed Eruption of Mount St. Helens, 2004-2006: USGS Professional Paper 1750: 20.

Moran, S.C., Malone, S.D., Qamar, A.L., Thelen, W.A., Wright, A.K. and Caplan-Auerbach, J., 2008a. Seismicity associated with renewed dome building at Mount St Helens, 2004-2005. Sherrod, D.R., Scott, W.E., and Stauffer, P.H., eds., 2008, A volcano

rekindled; the renewed eruption of Mount St. Helens, 2004-2006: U.S. Geological Survey Professional Paper 1750: 27-53.

Moran, S.C., McChesney, P.J. and Lockhart, A.B., 2008b. Seismicity and infrasound associated with explosions at Mount St. Helens, 2004-2005. Sherrod, D.R., Scott, W.E., and Stauffer, P.H., eds., 2008, A volcano rekindled; the renewed eruption of Mount St. Helens, 2004-2006: U.S. Geological Survey Professional Paper 1750: 111-129.

Pallister, J., Cashman, K. and Hagstrum, J., 2008a. Conduit-margin Faulting at Mount St. Helens - a seismogenic process?, American Geophysical Union, Fall Meeting 2008.

Pallister, J.S., Thornber, C.R., Cashman, K.V., Clynne, M.A., Lowers, H.A., Mandeville, C.W., Brownfield, I.K. and Meeker, G.P., 2008b. Petrology of the 2004-2006 Mount St. Helens lava dome - implication for magmatic plumbing and eruption triggering. Sherrod, D.R., Scott, W.E., and Stauffer, P.H., eds., 2008, A volcano rekindled; the renewed eruption of Mount St. Helens, 2004-2006: U.S. Geological Survey Professional Paper 1750: 647-702.

Power, W.L. and Tullis, T.E., 1989. The relationship between slickenside surfaces in fine-grained quartz and the seismic cycle. Journal of Structural Geology, 11: 879-894.

Rowe, M.C., Thornber, C.R. and Kent, A.J.R., 2008. Identification and Evolution of the Juvenile Component in 2004-2005 Mount St. Helens Ash. Sherrod, D.R., Scott, W.E., and Stauffer, P.H., eds., 2008, A volcano rekindled; the renewed eruption of Mount St. Helens, 2004-2006: U.S. Geological Survey Professional Paper 1750: 629-646.

Rutter, E.H., 1986. On the Nomenclature of Mode of Failure Transitions in Rocks. Tectonophysics, 122(3-4): 381-387.

Schilling, S.P., A., R.R., A., M.J. and Y., I.E., 2008. Use of Digital aerophotogrammetry to determine rates of lava dome growth, Mount St. Helens, Washington. Sherrod, D.R., Scott, W.E., and Stauffer, P.H., eds., 2008, A volcano rekindled; the renewed eruption of Mount St. Helens, 2004-2006: U.S. Geological Survey Professional Paper 1750: 24.

Scott, W.E., R., S.D. and A., G.C., 2008. Overview of the 2004-2006, and continuing, eruption of Mount St. Helens, Washington. Sherrod, D.R., Scott, W.E., and Stauffer, P.H., eds., 2008, A volcano rekindled; the renewed eruption of Mount St. Helens, 2004-2006: U.S. Geological Survey Professional Paper 1750: 23.

Sherrod, D.R., Scott, W.E. and Stauffer, P.H., 2008. A volcano rekindled; the renewed eruption of Mount St Helens, 2004-2006. Sherrod, D.R., Scott, W.E., and Stauffer, P.H., eds., 2008, A volcano rekindled; the renewed eruption of Mount St. Helens, 2004-2006: U.S. Geological Survey Professional Paper 1750: 856.

Skempton, A., 1966. Some observations of tectonic shear zones. paper presented at Proc. 1st International Conferecne of Rock Mechanics.

Smith, R., Sammonds, P.R., Tuffen, H. and Meredith, P.G., 2011. Evolution of the mechanics of the 2004-2008 Mt. St. Helens lava dome with time and temperature. Earth and Planetary Science Letters, 307(1-2): 191-200.

Snoke, A.W., Tullis, J. and Todd, V.R., 1998. Fault-related rocks-a photographic atlas: . Princeton University Press.

Sparks, Murphy, Lejeune, Watts, Barclay and Young, 2000a. Control on the emplacement of the andesite lava dome of the Soufriere Hills volcano, Montserrat by degassing-induced crystallization. Terra Nova, 12(1): 14-20.

Sparks, R.S.J., Murphy, M.D., Lejeune, A.M., Watts, R.B., Barclay, J. and Young, S.R., 2000b. Control on the emplacement of the andesite lava dome of the Sourfiere Hills volcano, Montserrat by degassing-induced crystallization. Terra Nova, 12(1): 14-20.

Sparks, R.S.J., Young, S.R., Barclay, J., Calder, E.S., Cole, P., Darroux, B., Davies, M.A., Druitt, T.H., Hartford, C., Herd, R., James, J., Lejeune, A.M., Loughlin, S.C., Norton, G.E., Skerrit, G., Stasiuk, M.V., Stevens, N.S., Toothill, T., Wadge, G. and Watts, R.B., 1998. Magma production and growth of the lava dome of the Soufriere HIlls Volcano, Montserrat, West Indies: November 1995 to December 1997. . Geophysical Research Letters, 25: 3421-3424.

Swanson, D.A. and Holcomb, R.T., 1990. Regularities in growth of the Mount St. Helens dacite dome. in Fink, J.H., (ed) Lava Flows and Domes: IAVCEI Proceedings in Volcanology: Berlin, Springer: 3-25.

Tanguy, J.-C., 2004. Rapid dome growth at Montagne Pelée during the early stages of the 1902-1905 eruption: a reconstruction from Lacroix's data. Bulletin of Volcanology, 66(7): 615-621.

Thornber, C.R., Pallister, J., Rowe, M.C., McConnell, S., Herriott, T.M., Eckberg, A., Stokes, W.C., Johnson Cornelius, D., Conrey, R.M., Hannah, T., Taggart, J.E., Adams, M.,

Lamothe, P.J., Budahn, J.R. and Knaack, C.M., 2008a. Catalog of Mount St. Helens 2004-2007 Dome Samples with Major and Trace-element Chemistry. U.S. Geological Survey Open-File Report 2008-1130 version 1.1.

Thornber, C.R., Pallister, J.S., Lowers, H.A., Rowe, M.C., Mandeville, C.W. and Meeker, G.P., 2008b. Chemsitry, mineraology and petrology of amphibole in Mount St Helens 2004-2006 dacite. Sherrod, D.R., Scott, W.E., and Stauffer, P.H., eds., 2008, A volcano rekindled; the renewed eruption of Mount St. Helens, 2004-2006: U.S. Geological Survey Professional Paper 1750: 727-754.

Vallence, J.W., J., S.D. and P., S.S., 2008. Growth of the 2004-2006 lava-dome complex at Mount St. Helens, Washington. Sherrod, D.R., Scott, W.E., and Stauffer, P.H., eds., 2008, A volcano rekindled; the renewed eruption of Mount St. Helens, 2004-2006: U.S. Geological Survey Professional Paper 1750: 40.

Van der Pluijm, B.A. and Marshak, S., 2004. Earth Structure Norton & Company, Inc. .

Watts, R.B.H.R.A., Sparks, R.S.J. and Young, S.R., 2002. Growth patterns and emplacement of the andesitic lava dome at Soufriere Hills Volcano, Monterrat. The eruption of Sourfiere Hills Volcano, Montserrat from 1995 to 1999: Geological Socity of London Memoir, 21: 37.

Wibbereley, C.A.J., Yielding, G. and Di Toro, G., 2008. Recent advances in the understanding of fault zone internal structure: a review Wibberley, C.A.J., Kurz, W., imber, J., Holdsworth, R.E. & Collettini, C. (eds) The Internal Structure of Fault Zones: Implications for Mechanical and Fluid-Flow Properties., The Geological Society of London 5-33.

Williams, H., 1932. THe history and character of volcanic domes. University of California, Bulletin of the department of Geological Sciences, 21: 51-146.

Wilson, B., Dewers, T., Reaches, Z. and Brune, J., 2005. Particle size ad energetics of gouge from earthquake rupture zones. Nature, 434(7 April 2005): 749-752.

Yund, R.A., Blanpied, M.L., Tullis, T.E. and Weeks, J.D., 1990. Amorphous Material in High Strain Experimental Fault Gouges. Journal of Geophysical Research, 95(B10): 589-602.

Appendices

APPENDIX A: Structural Data

Table A.1. Structural Data. Field structural data that is summarized in Table 1 of local fault plane, the rake of slickenside lineations and the local kinematic plane. Locations of data collection points are provided in Figure 2, map of the crater.

Spine	Location	Fault Plane	Rake of slickensides	Motion Plane	Sample/Notes
4	D4G1	320/28	x	x	
4	D4G2	325/23	26 N	180, 66 W	epoxied samples
		312/26	41 N		
		318/25	40 N		
		318/26	26 N		
4	D4L4	331/28 E	18 SE	132, 50 W	just sample collection n of helicopter
		345/36 E	16 SE	144, 55 W	
4	D4G5	290/30 NE	54 NW	168, 74 W	folding
4	D4G4	285/42 N	62 NW	168, 72 W	normal faulting - photo
		283/40 N	60 NW		BF10-D4X-A
4	D4L7	254/35 N	83 W	156, 88 W	BF10-MSH-D4Y-A
		256/36 N	86 W	157, 84 W	BF10-MSH-D4Y-B
		252/14 N	X		BF10-MSH-D4Y-C
4	D4G6	290/38 N	60 NW	184, 74 W	horizontal joining -cooling fractures
		300/30 N	50 NW	172, 70 W	
		295/33 N	52 NW	170, 88 W	
5	D5L1	009/61 E	38 NE	246, 41 NW	Bf-D5-A
		002/68 E	40 NE		BF-D5-B
		005/60 E	38 NE		
		002/62 E	39 NE		
		004/64 E	40 NE		General Strike of top of Ridge
5	D5L2	000/65 E	41 NE	244, 46 NW	
		002/62 E	40 NE		
7	D7G1	009/60 E	46 NE	060, 65 NW	BF10-D6-D
		008/46 E	54 NE		BF10-D6-C
		000/48 E	56 NE		BF10-D6-B

Table A.1. Structural Data. Field structural data that is summarized in Table 1 of local fault plane, the rake of slickenside lineations and the local kinematic plane. Locations of data collection points are provided in Figure 2, map of the crater.

Spine	Location	Fault Plane	Rake of slickensides	Motion Plane	Sample/Notes
7	D7L2	008/54 E	50 NE	070, 70 NW	surface of fault
		006/53 E	52 NE		
		002/46E	46 NE		
		000/40 E	54 NE		
		008/46 E	54 NE		
		001/54 E	56 NE		
		004/52 E	46 NE		
		006/50 E	48 NE		
7	D7L3	020/52 E	58 NE	088, 62 N	BF-D6-C

APPENDIX B: Grid Maps

The following are field grid maps from Spine 4. See Table 2.1 and Figure 2.1 for structural details and locations within the crater.

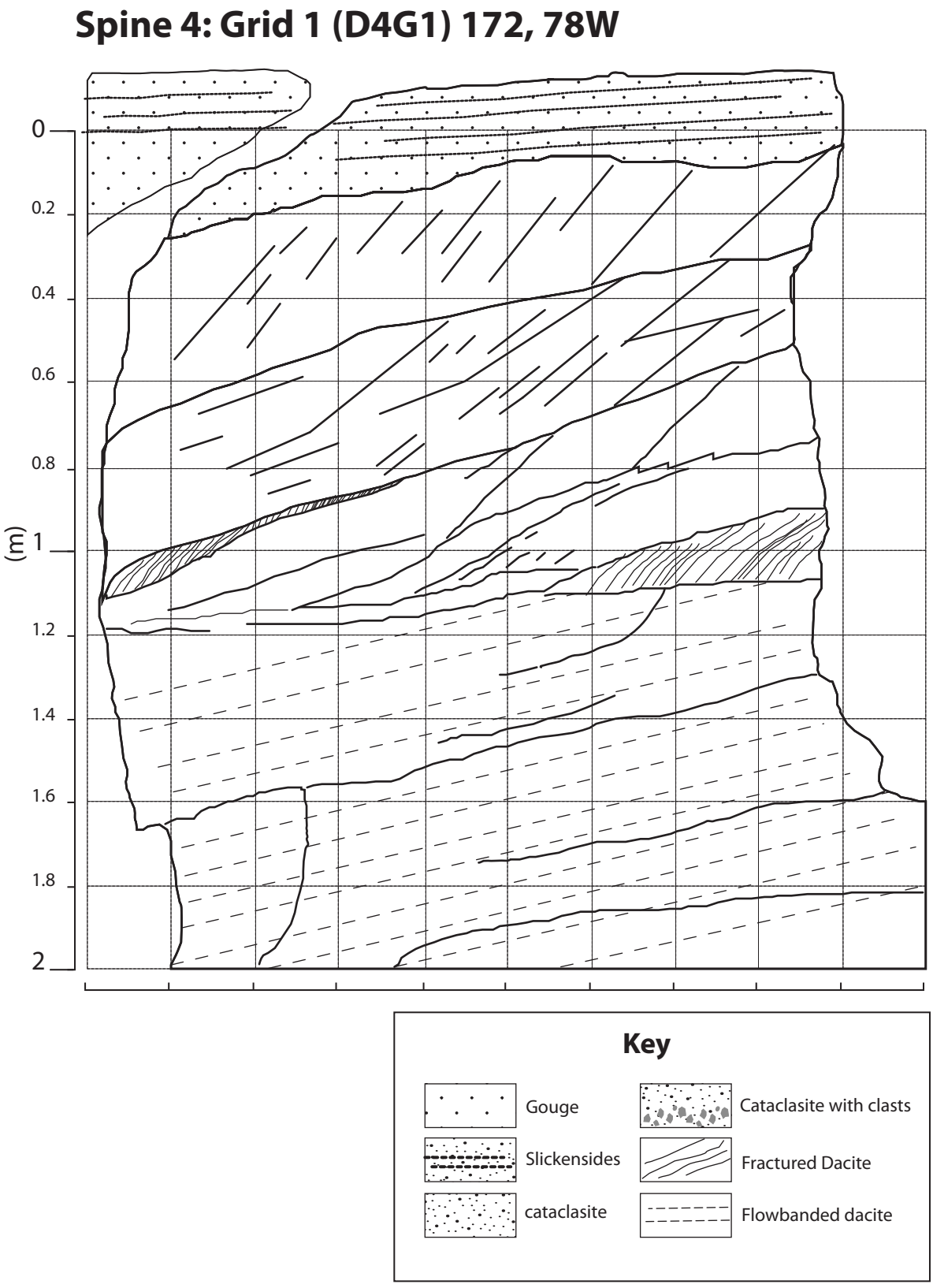

Figure B.1. Field Map of D4G1. See Figure 2.1 for location and Table 2.1 for structural details.

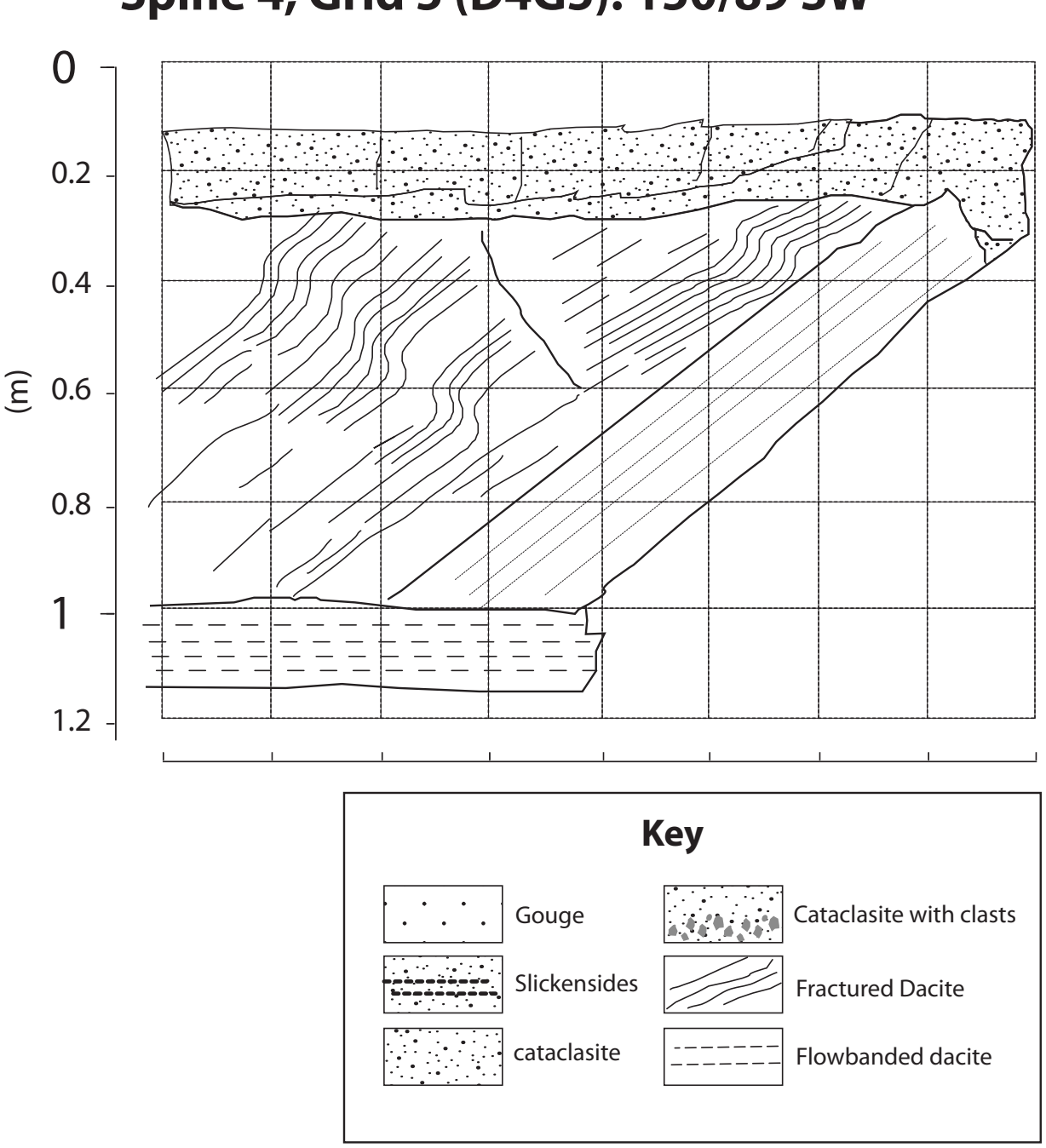

Figure B.2. Field Map of D4G5. See Figure 2.1 for location and Table 2.1 for structural details.

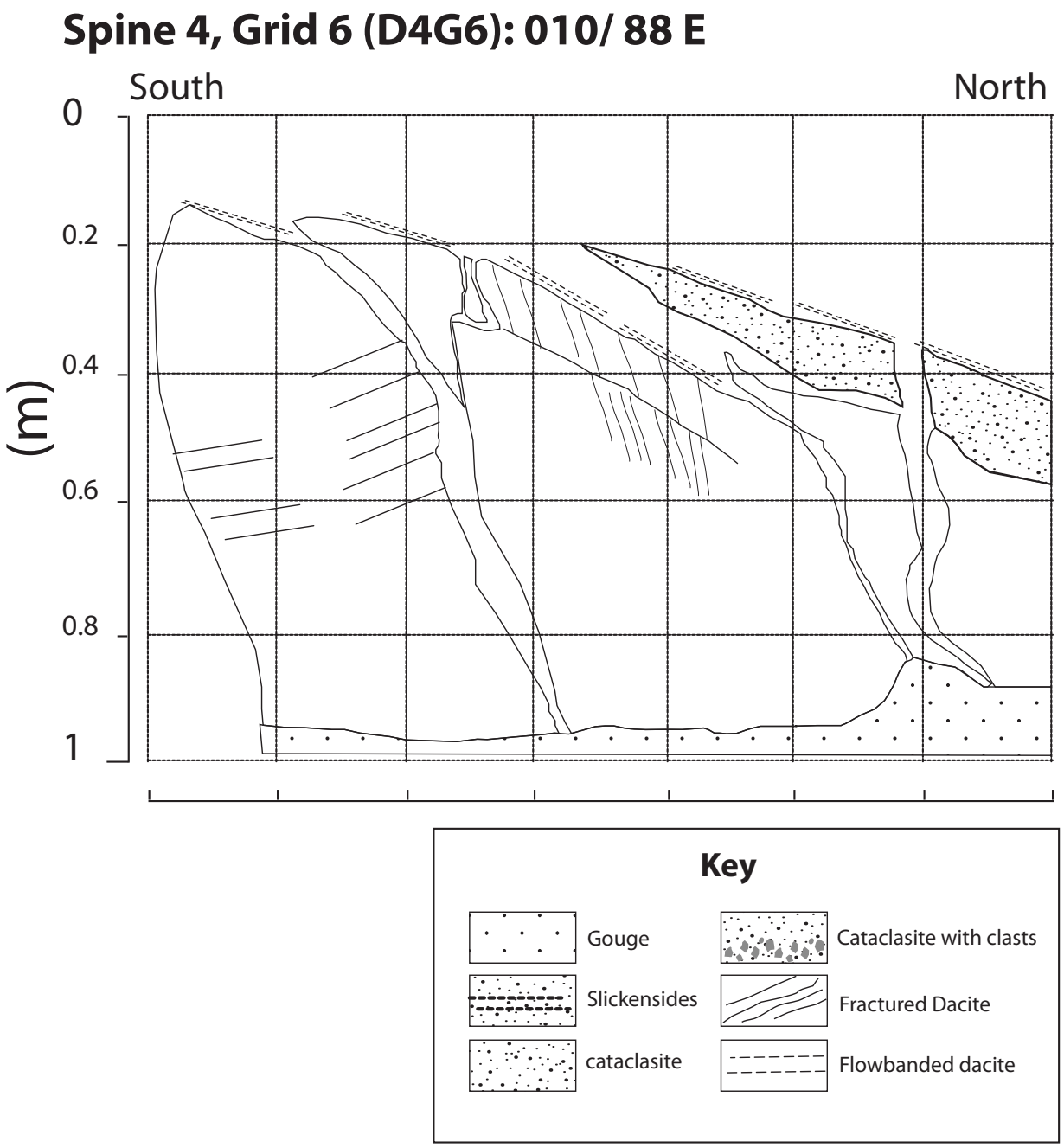

Figure B.3. Field Map of D4G5. See Figure 2.1 for location and Table 2.1 for structural details.

Appendix C. List of Samples

Table C.1. Master Sample List: Sample list with specific locations, orientations and depth from the main fault-core/damage zone boundary.

SPINE	SAMPLE LABEL	Distance (m)	SIZE (cm)	DESCRIPTION	FP	GRID	KP	Thin Section
	Spine 4 Grid 5 (D4G5)				*290/30 N*	*150/89 SW*	*168/74 W*	
4	BF10_MSH_D4G5_A	0.20	Med	contact between cohesive gouge and finely ridel fabricated cohesive dacite				TS
	Spine 4 Grid 6 (D4G6)				*285/24 N*	*010/88 E*	*168/72 W*	
4	BF10_MSH_D4GX_a	0.15	8x20x25	Cohesive dacite with rough slicknsides same plane as A				
4	BF10_MSH_D4GX_B	0.15	bag	Fragile - see Grid X				
	Spine 4 Location 7 (D4L7)				*254/35 NW*	-	*157/84 W*	
4	BF1-_MSH_D4Y_A	0.61	big 40x20	In place sample, same plane as sample B, granny skin/folding texturs etc				
4	BF10_MSH_D4Y_B1	0.55	y	EXCELLENT example of microfolding within cohesive layer of dome rock - small folds inbetween				TS
4	BF10_MSH_D4Y_B2	0.59	y	EXCELLENT example of microfolding within cohesive layer of dome rock - small folds inbetween				TS
4	BF10_MSH_D4Y_C	0.10	20x18	CONDOM LOCATION TOP of spine 4, spine surface with slickmsides on top				TS
	SPINE 5 Location 1			*strike of ridge = ~ 004 see field notebook for more data*	*009/61 E*	-	*246/41 NW*	
5	BF10_MSH_D5_A	0.10	20x33 slab	perfectly oriented sets of slicknsides - RAKE = 38, 40, 37, NE				TS
5	BF10_MSH_D5_B	0.14	slab	perfectly oriented sets of slicknsides				TS
5	BF10_MSH_D5_C	0.00	6x6x2	gouge - on top of sample B				
5	BF10_MSH_D5_D	0.14	15x20x6	gouge to slicknside				
5	BF10_MSH_D5_E	0.40	30x20x20	cataclasite - still cohesive, see in "strat" log				
5	BF10_MSH_D5_F	2.40	30x20x21	Cohesive dacite - at bottom				TS
	Spine 7 Grid 1				*009/60 E*	*235/82 NW*	*240/65 NW*	
7	BF10_MSH_D7_A	0.05	4cm slabs	perfectly oriented slicknsides about 4 cm thick slabs				TS
7	BF10_MSH_D7_B	0.10	4cm slabs	perfectly oriented slicknsides about 4 cm thick slabs				
7	BF10_MSH_D7_D1	0.02	22x15x8	of slicknsides also				TS
7	BF10_MSH_D7_D3	0.02	22x15x8	of slicknsides also				TS
7	BF10_MSH_D7_D4	0.02	22x15x8	of slicknsides also				TS
7	BF10_MSH_D7_E	0.00	10z10z8	gouge layer above the rest of samples, not oriented				
7	BF10_MSH_D7_F	0.20	25x10x15	Also discrete fault layers throughout sample				
7	BF10_MSH_D7_G	0.00	fist	slicknsides on gouge - fragile				
7	BF10_MSH_D7_H	0.15	LARGE	Gouge to black C/S fabric!!! CHECK THIS OUT - lots of BRITTLE/DUCTILE !!!				
7	BF10_MSH_D7_I	0.20	LARGE	See discrete slip and more brittle textures off first glace than sample H				
7	BF10_MSH_D7_J	0.15	20x20x20	Transition between lighter dacite to black				
7	BF10_MSH_D7_K1	0.22		Transition between dark to gouge with steps, mineral stretching, fracturing and rotation				TS
7	BF10_MSH_D7_K2	0.25		Transition between dark to gouge with steps, mineral stretching, fracturing and rotation				TS
7	BF10_MSH_D7_K3	0.28		Transition between dark to gouge with steps, mineral stretching, fracturing and rotation				TS
7	10-SK-MSH-3-1	-	30x20x5	Flowbanded dacite with band restricted defromation				
7	10-SK-MSH-3-2	-	20x15x5	Flowbanded dacite with band restricted defromation				
7	AK10_MSH_D6_F1	-	Big und	White cohesive Dacite				

Appendix C. List of Samples

Table C.1.: Master Sample List: Sample list with specific locations, orientations and depth from the main fault-core/damage zone boundary.

SPINE	SAMPLE LABEL	Distance (m)	SIZE (cm)	DESCRIPTION	FP	GRID	KP	Thin Section
	Spine 7 Location 2							
7	BF10_MSH_D7_C	0.50	of 40x30	from the north side of Spine 7 - looking south. Plane is plane of rock, not plane of motion		*009/60 E*	-	*240/65 l*
7	BF10_MSH_D7_L	0.05		stretching, fracturing and rotation				
7	BF10_MSH_D7_O	-	med	light and dark mixing shear etc		float		
7	BF10_MSH_D7_M	-	med	light dacite with fiame looking black materail dispersed throughout		float		
7	10-SK-MSH-5-1	0.15	15x15x5	Mylonite/Pseudotachylite				
7	10-SK-MSH-5-2	0.15	15x15x10	Mylonite/Pseudotachylite with ash veins				
7	10-SK-MSH-5-3	0.20	20x5x3	Mylonite/Pseudotachylite				
	Misc Gouge Samples							
DOME	***SAMPLE #***		***SIZE cm***	***DESCRIPTION***				
4	10-SK-MSH-2-1	0.00	5x2x2	Dacite-gauge interface with aaflow like structures				
4	10-SK-MSH-2-2	0.00	5x5x5	Dacite-gauge interface with aaflow like structures				
4	10-SK-MSH-2-3	0.00	15x10x15	Dacite-gauge interface with aaflow like structures				
7	10-SK-MSH-4-1	-0.20	20x10x5	Consolidated gauge for grainsize analysis				
7	10-SK-MSH-4-2	-0.20	20x10x10	Consolidated gauge for grainsize analysis				
7	10-SK-MSH-4-3	-0.20	20x10x10	Consolidated gauge for grainsize analysis				
7	10-SK-MSH-5-4a	-0.10	25x10x10	Gauge overlying Mylonite/Pseudotachylite				
7	10-SK-MSH-5-4b	-0.10	25x10x10	Gauge overlying Mylonite/Pseudotachylite				
4	10-SK-MSH-6	-0.20	20x10x5	Gauge overlying dicected fault zone in Spine 4 on the way to 5				
4	10-SK-MSH-8-1	-0.50	10x10x10	Loose gauge for grainsize, spine 4 close to extrusionsite (to outside)				
4	10-SK-MSH-8-2	-0.50	10x10x10	Loose gauge for grainsize, spine 4 close to extrusionsite (to dacite)				
3	10-SK-MSH-9	-0.40	15x15x5	Consolidated gauge for grainsize analysis				
4	10-SK-MSH-10	-0.40	30x25x20	Consolidated gauge for grainsize analysis at condom bomb				
	1980 DOME							
1980	BF10_MSH1980_A		13x12cm	rough top - flow pattern - not quite slicknside - maybe? Xenolith turned and stretched				
1980	BF10_MSH1980_C		15x8	lower porosity from top of "spine"				
1980	BF10_MSH1980_D		10x10	lower porosity from top of "spine"				
1980	BF10_MSH1980_aD		3 cmx10	lower porosity from top of "spine"				
1980	BF10_MSH1980_E		BAG	layer of small broken stretches bubbles				
1980	BF10_MSH1980_F		6X2	small sample - bubble variety nucleation around zenolith				
1980	BF10_MSH1980_G		16x9 cm	strain of stretched bubbles around xenolith				
1980	BF10_MSH1980_H		8x3	slicknside surface				
1980	BF10_MSH1980_I		Bag	"gouge" type layer between cohesive				
1980	BF10_MSH1980_M		23x10 cm	dark: variations in porosity?				
1980	BF10_MSH1980_N		17x20 cm	shows bubble wall stretching				
1980	BF10_MSH1980_O		30x30	high porosity sample				
1980	BF10_MSH1980_misc		Bag	Bag of misc samples showing the porosity variation				
1980	AK10_MSH_1980_A		BIG-und	higher porosity				
1980	AK10_MSH_1980_B		BIG-und	lower porosity				

Appendix C. List of Samples

Table C.1, Master Sample List: Sample list with specific locations, orientations and depth from the main fault-core/damage zone boundary.

SPINE	SAMPLE LABEL	Distance (m)	SIZE (cm)	DESCRIPTION	FP	GRID	KP	Thin Section
	Spine 4 Grid 1 (D4G1)				*312/28 NE*	*172/78 W*	*171/62 W*	
4	BF10_MSH_D4G1_A	0.00	Bag	Unconsolidated gouge from top layer				
4	BF10_MSH_D4G1_J	0.65	3x10x6	cohesive dacite bottom fine gouge				TS
4	BF10_MSH_D4G1_H	0.90	15x15x4	layers of small fault surfaces				
4	BF10_MSH_D4G1_F1	1.00	20x20x5	small micro fracture surfaces aligned fabric is in same plane of ridel zone				TS
4	BF10_MSH_D4G1_F2	1.04	20x20x5	small micro fracture surfaces aligned fabric is in same plane of ridel zone				TS
4	BF10_MSH_D4G1_B1	1.98	24x5	elongate sample, intact check for banding				TS
4	BF10_MSH_D4G1_B2	2.05	24x5	elongate sample, intact check for banding				TS
4	BF10_MSH_D4G1_C	1.40	12/19/201	cohesive dacite :note the fine ash layer/slicknsides on top of sample - very fragile				
4	BF10_MSH_D4G1_D	1.10	20x20x5	cohesive dacite at the north tip of onion skin on grid : coarse "slicknsides" on top and bottom surface				
4	BF10_MSH_D4G1_E	0.95	10x5x5	small micro fracture surfaces aligned fabric is in same plane of ridel zone				TS
4	BF10_MSH_D4G1_G	1.10	flakes	Flakes of onion skin layered damage				TS
4	AK10_MSH_D4G1_D1	2.20	large	Large undeformed block - AK sample				
4	BF10_MSH_D4G1_N	3.00	50x30	Large, long "undeformed" sample as possible in place check sample for flow banding				
4	AK10_MSH_D4_A	3.13	BIG-und	Cohesive dacite				
	Spin 4 Grid 2 (D4G2)				*325/23 NE*	*169/85W*	*180/66 W*	
4	BF10_MSH_D4G2_A	1.10	22x12x4	top is contact between two "y " sandwitched surfaces				
4	BF10_MSH_D4G2_B	0.60	15x6x5	fractured dacite, still cohesive				
4	BF10_MSH_D4G2_C	0.80	4x3x3	coarse slicknsides on top with layers of slip				TS
4	BF10_MSH_D4G2_D	1.20						
4	BF10_MSH_D4G2_E	0.10	bulb"	bulb that pushed its way into gouge - see photos and close up sketch				
4	BF10_MSH_D4G2_F	0.00	bag	unconsolidated gouge				
4	SK10-MSH-D4G2-L1	-0.10	10x10x5	Loose gauge profile through gauge overlying JP wall				
4	SK10-MSH-D4G2-L2	-0.20	10x10x5	Loose gauge profile through gauge overlying JP wall				
4	SK10-MSH-D4G2-L3	-0.30	10x10x5	Loose gauge profile through gauge overlying JP wall				
4	SK10-MSH-D4G2-L4	-0.40	10x10x5	Loose gauge profile through gauge overlying JP wall				
4	SK10-MSH-D4G2-L5	-0.50	10x10x5	Loose gauge profile through gauge overlying JP wall				
4	SK10-MSH-D4G2-L6	-0.60	10x10x5	Loose gauge profile through gauge overlying JP wall				
4	10-SK-MSH-1-1a	-0.10	10x10x5	Fault gauge over JP wall in epoxy				
4	10-SK-MSH-1-1b	-0.10	15x20x10	Fault gauge over JP wall in epoxy				
4	10-SK-MSH-1-2	-0.20	10x10x5	Fault gauge over JP wall in epoxy				
4	10-SK-MSH-1-3	-0.30	10x10x5	Fault gauge over JP wall in epoxy				
4	10-SK-MSH-1-4	-0.40	10x10x5	Fault gauge over JP wall in epoxy				
4	10-SK-MSH-1-5	-0.50	10x10x5	Fault gauge over JP wall in epoxy				
	Spine 4 Location 4 (D4L4)				*331/28 NE*	-	*132/50 SW*	
4	BF10_MSH_D4G4_A	0.00	bag	unconsolidated poorly sorted gouge				
4	BF10_MSH_D4G4_B	0.10	bag	Chunkjs of fine SS out of gouge				
4	BF10_MSH_D4G4_C	0.18	bag	Coarse gouge in layed				
4	BF10_MSH_D4G4_D	0.22	15x6	cohesive gouge				
4	BF10_MSH_D4G4_E	0.12	pankake	slicknsides (fine) on top of gouge				TS
4	BF10_MSH_D4G4_F	0.10	pankake	slicknsides (fine) on top of gouge				

APPENDIX D: Geochemistry

The bulk chemistry of the erupted dacite and deformed fault rocks is fairly consistent through the entire eruption from 2004-2008 (Sherrod et al., 2008; Thornber et al., 2008a). Deviations were observed in the early-erupted gouge samples of Spines 3 and 4 with lower SiO_2 values. This decrease results from the abrasion between the erupting dacite and conduit wall rock that is basalt and andesite from the Castle Creek eruptive period 100-200 m from the vent, under the 1980-86 dome (Clynne et al., 2008; Pallister et al., 2008a). For the duration of the eruption the gouge and dacite remained consistent at a 65% SiO_2 as the conduit wall became well lubricated with fault gouge with the exception of a dip in SiO_2 values when Spine 6 erupted at the surface in July 2005. This may be the result of a slight shift in conduit position, incorporating more andesite and basalt wall rock (Clynne et al., 2008; Pallister et al., 2008a).

XRF

While the geochemical record of the eruption is thorough, we analyzed in place samples and targeted the high strain zone in Spine 7. The bulk chemical composition of four samples across this high strain zone was analyzed using X-Ray Fluorescence (XRF) through the fused beads prepared from ignited samples. Analysis of the minor elements was conducted on pressed powder pellets and volatile species were analyzed using an ELTRA CS-800 automated analyzer. The XRF analyses were carried out on samples from each fault texture from various locations on the spine 7 outcrop: cataclasite interbedded with ultracataclasite-slickensides, no-porosity ultrafine-grained black cataclasite, grey dacite with a p-shape fabric, cohesive pink flow banded dacite. The depths of each sample within the shear zone are provided in Table D-1.

The results of the XRF analyses are shown in Table D-1. The major element content is essentially identical within the local shear zone in Spine 7 and with the previous erupted dacite spines. These results are two fold: (1) they indicate that the cataclasite, gouge and ultrafine-cataclasite, dense, black zone are formed in-situ at the exterior of Spine 7 and (2) these textures are a result of deformation path that is unique to Spine 7 as it is geochemically identical to Spine 1-6.

XRD

To determine the glass content and the presence of mineral modes, sixteen samples were analyzed using the X-Ray powder Diffraction smear mount method (Program EP Stand 05S 50) at UBC. The samples were ground into fine powder with a corundum mortar and smeared on to glass slides with ethanol. Step-scan X-ray powder-diffraction data were collected over a range 3-80°2q with CoKa radiation on a Bruker D8 Focus Bragg-Brentano diffractometer equipped with an Fe monochromator foil, 0.6 mm (0.3°) divergence slit, incident- and diffracted-beam Soller slits and a LynxEye detector. The long fine-focus Co X-ray tube was operated at 35 kV and 40 mA, using a take-off angle of 6°. Mineral identification was done using the International Centre for Diffraction Database PDF-4 and Search-Match software by Siemens Bruker.

The XRD analyses were carried out on samples from Spine 4 and Spine 7 on the following units: slickenside surfaces, cataclasite, and protolith dacite. Specific samples from the black, aphanitic, ultrafine-cataclasite were also run. In two of these Spine 7 samples, phenocrysts were picked out of the dense black material to understand the componentry of t the matrix and test the presence of non-crystalline material.

Results are summarized in Table D-2. Every sample has roughly the same mineralogy with a strong modal abundance of plagioclase feldspar, quartz, amphibole and orthopyroxene.

There is a clear peak presence for tridymite occurrence, but not cristobalite. This does not discount the occurrence of this quartz polymorph, observed by Pallister et al. (2008), because cristobalite cannot be deciphered from quartz using the XRD method of analysis. Some diffractograms of the ultrafine-grain slickensides and ultrafine-grained cataclasite from spine 4 and spine 7 exhibit a weak non-crystalline hump.

Table D.1. Geochemistry (XRF). Whole rock Chemical compositions details of samples from spine 7 fault zone in comparison and the undeformed dacite sample (SH305-1;Thornber et al. 2008).

SAMPLE	BF10-MSH-D6A	BF10-MSH-D7G	BF10-MSH-D7F	BF10-MSH-D7C	SH305-1 Dacite1
DETAILS	Cataclasite with slicknsides	black material	Grey matieral	pink dacite near xenoliths	Spine 3 float
Distance (cm)	0 cm	3 cm	10 cm	26 cm	
MAJORS					
SiO2	64.85	64.29	64.60	65.19	65.31
TiO2	0.63	0.62	0.62	0.62	0.61
Al2O3	17.26	17.31	17.26	17.00	17.35
Fe2O3	4.66	4.66	4.69	4.59	3.82
MnO	0.07	0.08	0.07	0.07	0.07
MgO	1.89	1.85	1.87	1.84	1.84
CaO	4.72	4.80	4.73	4.53	4.71
Na2O	4.69	4.73	4.73	4.65	4.76
K2O	1.47	1.48	1.50	1.51	1.41
P2O5	0.09	0.14	0.15	0.08	0.12
LOI	0.00	0.00	0.00	0.06	
Total	100.39	100.02	100.28	100.19	
Volatiles (wt%)					
CO2 (%)	<d/l	<d/l	<d/l	<d/l	
H20	0.04	0.06	0.06	0.07	
Trace Element Content (ppm)					
BaO	387.0	376.0	384.1	373.6	
Ce	33	53	48	28	
Co	24	20	22	24	
Cr2O3	<d/l	20.9	24.4	<d/l	
Cu	46	61	49	24	
Ni	<d/l	<d/l	6	5	
Sc	<d/l	<d/l	<d/l	<d/l	
V	80.0	76.9	76.0	73.3	
Zn	22	21	22	26	
Ga	19.3	19.4	19.2	19.3	
Nb	4.7	5.5	6.4	5.1	
Pb	9.2	8.4	9.3	7.6	
Rb	32.8	34.1	34.6	34.5	
Sr	438.0	443.3	437.8	431.7	
Th	2.5	2.4	2.8	3.1	
U	1.7	<d/l	1.3	1.2	
Y	8.4	10.9	10.9	8.0	
Zr	126.4	126.0	131.6	126.3	

*Data from Thornber et al USGS Open-File Report 2008-1130

Table D.2. Geochemsitry XRD. Average mineralogy of fault rocks and undeformed dacite of the Mount St Helens 2004-2008 Dacite Eruption

	Rock Units							
	Spine 4			**Spine 7**				
Minerals	Slickensides	Cataclasite	Dacite	Slickensides	Grey Cataclasite	Black Cataclasite[a]	Black Cataclasite[b]	Dacite
Plagioclase Feldspar	abundant	abundant	abundant	abundant	abundant	abundant	abundant	abundant
Quartz	abundant	abundant	abundant	abundant	abundant	abundant	abundant	abundant
Trydimite	minor	3	common	3	3*	3	-	3
Crystobalite	-	-	-	-	-	-	-	-
Hornblende	trace	minor	minor	minor	trace	trace	trace	minor
Hypersthene	-	minor	minor	-	minor	-	trace	minor
Non-crystalline buldge	minor	no	no	minor	no	minor	minor	no

Relative mineral abundance determined by X-ray diffraction analysis: **abundant** > 25% > **common** > 10% > **minor** > 3% > **trace** > 0%

[a] black cataclasite with phenocrysts of 4 analyses

[b] black cataclasite absent of phenocrysts of 5 analyses